Universitat Autònoma de Barcelona

Metal-Organic Frameworks made of amino acids and adenine: chirality and hydrochromism

Iván Patricio Burneo Saavedra

Universitat Autònoma de Barcelona

Metal-Organic Frameworks made of amino acids and adenine: chirality and hydrochromism.

Iván Patricio Burneo Saavedra

Doctoral Thesis

Ph. D. in Chemistry

Supervisors

Dr. Daniel Maspoch and Dr. Inhar Imaz

Tutor

Dr. Jordi Hernando

Catalan Institute of Nanoscience and Nanotechnology (ICN2)

Departament de Química - Facultat de Ciències

2017

Thesis presented to aspire to the Doctorate in Chemistry degree by Iván Patricio Burneo Saavedra.

Dr. Daniel Maspoch
ICREA Research Professor & Group Leader
Supramolecular Nanochemistry and Materials Group
Institut Català de Nanociència i Nanotecnologia

Dr. Inhar Imaz
RyC Researcher & Division Coordinator
Supramolecular Nanochemistry and Materials Group
Institut Català de Nanociència i Nanotecnologia

Dr. Jordi Hernando

Professor Agregat
Departament de Química
Universitat Autònoma de Barcelona

The present PhD thesis has been carried out at the Supramolecular Nanochemistry and Materials Group of the Catalan Institute of nanoscience and nanotechnology (ICN2) following the doctoral program in Chemistry of the Autonomous University of Barcelona. According to the decision of PhD Commission, this PhD Thesis is presented as a compendium of publications.

The publications are listed below in order of their appearance in the Thesis:

1) Iván Burneo, Kyriakos C Stylianou, Inhar Imaz, Daniel Maspoch. The influence of the enantiomeric ratio of an organic ligand on the structure and chirality of metal–organic frameworks. *Chemical Communications*, **2014**, 50, 13829-13832.DOI: 10.1039/C4CC06190J

2) Iván Burneo, Kyriakos C Stylianou, Sabina Rodríguez-Hermida, Jordi Juanhuix, Xavier Fontrodona, Inhar Imaz, Daniel Maspoch. Two New Adenine-based Co(II) Coordination Polymers: Synthesis, Crystal Structure, Coordination Modes and Reversible Hydrochromic Behavior. Crystal Growth and Design, **2015**, 15, 3182–3189. DOI: 10.1021/acs.cgd.5b00218

Table of Contents

Abstract

The present Thesis has been addressed to the synthesis of bio-related metal-organic frameworks and coordination polymers as novel and functional materials. On the basis of the above, two main lines were developed to reach the objectives proposed: i) study the influence of enantiomeric ratio of two chiral ligands over the structure and chirality in Metal-Organic Frameworks, and ii) the design and synthesis of novel coordination polymers based in nucleobase-adenine, aromatic tetracarboylate ligands and transition metals.

In Chapter 1, we showed a brief review about Coordination Polymers (CPs)/Metal-Organic Frameworks (MOFs), their chemistry, synthetic methods and their current applications, as gas adsorption or catalysis, with emphasis in ones which use biomolecules as building blocks for the construction of coordination polymers. Then, general objectives of this Thesis are described in Chapter 2.

Chapter 3 describes the importance of chirality as an important property in CPs/MOFs, and summarized the results obtained and reported in the article "The influence of the enantiomeric ratio of an organic ligand on the structure and chirality of metal–organic frameworks", *Chemical Communications*, 2014, 50, 13829-13832. In this work, we showed the importance of enantiomeric ratio as relevant variable in the synthesis of porous metal-organic frameworks, and as it might be introduced as variable with surprising results, which enabled us to obtain a porous material varying the enantiomeric ratio.

In Chapter 4, we aimed to develop new adenine-based coordination polymers using aromatic tetracarboxylic acids, as auxiliary linker and Co(II). We showed in the article titled “Two New Adenine-based Co(II) Coordination Polymers: Synthesis, Crystal Structure, Coordination Modes and Reversible Hydrochromic Behavior”, *Crystal Growth and Design*, 2015, 15, 3182–3189, where we took advantage of its five potential coordination sites for metal binding, showing the relevance of adenine as rigid linker in the synthesis of functional coordination polymers.

Resumen

La presente Tesis ha sido enfocada en la síntesis de Polímeros de Coordinación (CPs) y Metal-organic frameworks (MOFs) a partir de ligandos basados en biomoléculas para la obtención de materiales nuevos y funcionales. Sobre esta premisa, la Tesis aborda dos líneas de investigación principales que han sido desarrolladas para alcanzar los objetivos propuestos: i) estudiar la influencia de la razón enantioméricos de dos ligandos quirales sobre la estructura y quiralidad en Metal-Organic Frameworks, y ii) el diseño y la síntesis de nuevos polímeros de coordinación basados en adenina, ligandos aromáticos tetracarboxílicos y metales de transición.

En el Capítulo 1, mostramos un breve resumen a cerca de la química, los métodos de síntesis y las aplicaciones actuales de CPs/MOFs, como, por ejemplo, absorción de gases o catálisis, con énfasis en aquellos en los cuales se usan biomoléculas como bloques de construcción. Posteriormente, en el Capítulo 2, describimos los objetivos generales de nuestra tesis.

El Capítulo 3 describe la importancia de la quiralidad como una importante propiedad en CPs/MOFs, y resume los resultados obtenido y publicados en el artículo "The influence of the enantiomeric ratio of an organic ligand on the structure and chirality of metal–organic frameworks", *Chemical Communications*, 2014, 50, 13829-13832. En este trabajo, hemos mostrado la importancia de la *razón enantiomérica* como variable relevante en la síntesis de MOFs porosos, y que puede ser tomada en cuenta como variable con resultados sorprendentes, la cual

nos ha permitido obtener materiales porosos variando la *razón enantiomérica*.

En el Capítulo 4, hemos tratado de desarrollar nuevos polímeros de coordinación basados en adenina usando ácidos aromáticos tetracarboxílicos, como ligandos auxiliares y Co(II). Lo resultados han sido publicados en el artículo titulado "Two New Adenine-based Co(II) Coordination Polymers: Synthesis, Crystal Structure, Coordination Modes and Reversible Hydrochromic Behavior", *Crystal Growth and Design*, 2015, 15, 3182–3189, donde hemos aprovechado de los cinco sitios potenciales de coordinación y mostrado la importancia de adenina como ligando rígido en la síntesis de polímeros funcionales.

Acknowledgements

I would like to give my sincere thanks to my supervisors, Prof. Daniel Maspoch and Dr. Inhar Imaz, for giving me the opportunity to work in their research group and study the fascinating chemistry of Metal-Organic Frameworks, and also for all I have learned about their work capacity, motivation and love for chemistry.

I would like to thank Dr. Kyriakos C. Stylianou and Dr. Sabina Rodríguez for their valuable guidance and very helpful discussion, who with their suggestions provide me a better understanding of the chemistry and synthesis of Metal-Organic Frameworks

I am also grateful to my colleagues and NanoUp group members Dr. Arnau Carné, Dr. Marta Rubio, Dr. Carlos Carbonell, Dr. Sonia García, Dr. Mary Cano, Dr. Vincent Guillerm, Dr. Nereida Mejías, Dr. Javier Pérez, Dr. Raquel Rios, Mr. Jorge Albalad, Ms. Blanca Chocarro, Mr. Amirali Yazdi, Mr. Heng Xu, Ms. Claudia Vignatti, Mr. Luis Carlos Garzón, Mr. Abraham Ayala, Mr. Jordi Espín and Mr. Javier Ariñez for the patient, generosity and friendship. Especially to Xavi Ariñez and Arnau Carné for their selfless friendship and the long hours of interesting conversation about everything and, especially about chemistry.

Thanks to the Institut Catalá de Nanociencia i Nanotecnologia and Universitat Autonoma de Barcelona for having given me the opportunity to develop my PhD Thesis in the best possible conditions.

Also, I would like to express my gratitude to the Secretaría de Educación Superior, Ciencia, Tecnología e Innovación (SENESCYT) of Ecuador for the award of Ph.D. Fellowship and the financial support.

Finally, I would like to say thanks to my family for their unconditional love, care, understanding, and support throughout these years.

Chapter 1

Introduction to Metal-Organic Frameworks made of biomolecules

1. Metal-Organic Frameworks (MOFs)

1.1 From Coordination Polymers to MOFs

"Serendipity" means "happy accident" or "fortunate mistake", and that is how the first man made coordination polymer (CP) was created in the early eighteenth century. Heinrich Diesbach, a German colormaker, discovered by accident a method for making the blue pigment known as Prussian blue.[1] Despite being a valuable pigment used all over the world, its crystalline structure remained unknown for around 200 years.[2] Today, it is known that Prussian blue is a CP with a 3-D cubic structure built up from the combination of heterometallic centres and cyanide organic ligands resulting in a mixed-valence polycyanide compound with a characteristic strong blue colour.

This example is the perfect illustration of the secret dream and permanent frustration of crystal engineers: how to predict the resulting final crystal structure from the supramolecular assembly of metal ions and/or organic molecules. This challenge is in line with the provocative assertion of Maddox,[3] for whom "one of the continuing scandals in the physical sciences is that it remains impossible to predict the structure of even the simplest crystalline solids from knowledge of their composition".

In the 80's, however, there were two crucial events that gave a real impulse to the design and prediction of new crystalline materials: Prof. Lehn introduced the new concept of Supramolecular Chemistry;[4] while Prof. Etter[5] and Prof. Desiraju[6] reported several works understanding the organisation of organic molecules through hydrogen bonds. Since

then, challenges in this field are not only the creation of new CPs but also the understanding and prediction of their crystal structures. Prof. Wells strongly contributed to this challenge by reducing the description of crystal structures to networks formed by points with certain geometries (*e.g.* octahedral, tetrahedral, etc.) connected to other points through lines.[7] In 1989, Robson *et al.* applied Wells' approach to the design of CPs.[8] They proposed that CPs could be obtained by simply connecting centres (metal ions) having either a tetrahedral or an octahedral array of valences with rod-like connecting units (organic ligands).[9]

At that moment, nobody could imagine that this new concept would open a new world in the field of chemistry, materials science and nanotechnology. But only five years later, Prof. Yaghi confirmed the high potentiality of these pioneering studies. He reported the hydrothermal synthesis, of an extended network with formula Cu(4,4'-bpy)1.5·NO_3(H_2O) (where 4,4'-bpy is 4,4' bypiridine) which contains large rectangular channels filled by nitrate ions. He showed that these nitrates could be exchanged by other anions, demonstrating the accessibility of the channels and the first zeolite-like properties in a coordination polymer.[10] In this study, Prof. Yaghi named this new compound as a Metal-Organic Framework (MOF)

When Prof. Yaghi introduced the term of MOF, it was unpredictable the potential of this new generation of "hybrid" materials and the quantity of structures with different compositions, topologies and properties which will be reported during the next 20 years. However, the large number of publications concerning these new materials and the

introduction of many terminologies to define them generated some confusion and misunderstanding. Indeed, since the middle of 90's, the new published compounds have been indistinctly termed as MOFs, coordination polymers, coordination networks, hybrid organic–inorganic materials and organic zeolite analogues.[11-15] To introduce some clarity and to define more clearly the different terminologies, some attempts have been made in the literature to elucidate their definition.[16, 17] Finally, the International Union of Pure and Applied Chemistry (IUPAC) has published some provisional recommendation defining a MOF as: *"a Coordination Compound continuously extending in 1, 2 or 3 dimensions through coordination bonds (Coordination Polymer or alternatively Coordination Network) with an open framework containing potential voids". And a coordination compound as: "any compound that contains a coordination entity. A coordination entity is an ion or neutral molecule that is composed of a central atom, usually that of a metal, to which is attached a surrounding array of atoms or groups of atoms, each of which is called ligands"*. [18]

The interest on MOFs is based on two key attributes: (i) their extremely large surface-areas given by its ultra-micro-porosity, the highest of any known materials; and (ii) the flexibility in which their structures and compositions can be varied, offering a diversity of pore shapes. Both attributes confer MOFs with potential for myriad applications. Most of these applications are obviously related to its ultra-high porosity (up to 7000 m2/g) (**Figure 1**), and mainly includes their use in storage, separation and catalysis. A tasting of the performance of MOFs in these applications is given below. Also, the progresses made in the MOF field

in terms of their synthesis, topologies and applications have today enveloped in many reviews.[14, 19-22]

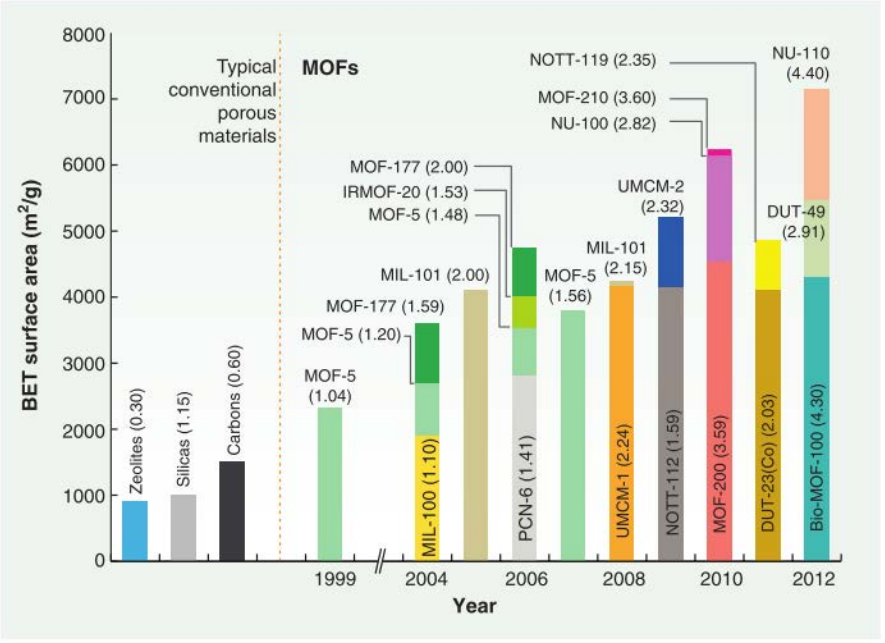

Figure 1 Progress in the synthesis of ultrahigh-porosity MOFs. Brunauer–Emmett–Teller (BET) surface areas of MOFs and typical conventional materials were estimated from gas adsorption measurements. The values in parentheses represent the pore volume (cm3/g) of these materials. Adapted from reference 12.

1.2 Biomolecules based MOFs: new natural ligands for new properties.

Organic synthesis has been undoubtedly a quasi-infinite source to generate new ligands for their use in the assembly of new metal-organic frameworks. Thanks to the large panel of possibilities that offer organic synthesis, the storage capacities of MOF has not ceased to increase, the tailoring of pores to a precise separation of gas has improved and the catalytic activities of MOFs reach more and more organic reactions. Beyond the classical properties of porous materials, the continuous incorporation of new organic ligands has allowed developing novel MOFs that introduce new properties. Beyond the classical rigid multitopic carboxylate and N-donor based molecules that constitute most of ligands studied so far, recently an increasing interest exists in introducing new ligands to form CPs because they can directly incorporate their own functionalities in the coordination structures.

Among them biomolecules offer a very large panel of ligands that have emerged recently as building blocks for constructing MOFs and incorporating new properties. Biomolecules offer several advantages to be used as biomolecules as building blocks in the construction of coordination polymers or metal-organic frameworks:

- Simple biomolecules, including amino acids, nucleobases, sugars, and others, are readily and naturally available in quantities and at prices amenable to preparing bulk quantities of materials.
- Biomolecules can lead to biologically-compatible MOFs.

- Biomolecules are structurally diverse. They can be either structurally rigid or flexible, aspects that impact the functional nature of the resulting MBioF.
- Biomolecules can have many different metal-binding sites. Consequently, they can exhibit multiple possible coordination modes, a feature that increases the potential structural diversity of MBioFs.
- Many biomolecules have intrinsic self-assembly properties which can be used to direct the structure and function of MBioFs.
- Finally, many biomolecules are chiral. Therefore, they can be used to construct chiral MBioFs, which may have interesting recognition, separation, and catalytic properties.

In this Section, we will try to give a representative overview of the use of biomolecules in the MOF synthesis.

1.2.1 Amino acids

Amino acids (AA) are molecules with the general formula H_3N^+—$(CR^1R^2)_n$—CO_2^- with n=1 for the series of α-amino acids, n=2 for β-amino acids (where H_3N^+ and CO_2^- are the amino and carboxylic acid groups, respectively, and R is the organic side chain). Amino acids are essential part of life because protein and peptides, that serve important biological functions, are made up from the linking of AA units *via* amide bonds. From coordination point of view, AA have two common metal binding sites, amino nitrogen and carboxylate oxygen atoms, but other kinds of metal binding sites can also be present in the side chain residues such as imidazole nitrogen atoms in *L*-histidine or thiolate and thioether sulfur

atoms in *L*-cysteine and *L*-methionine, respectively, and also β-carboxylic groups in aspartic acid and glutamic acid (**Figure 2**).[23]

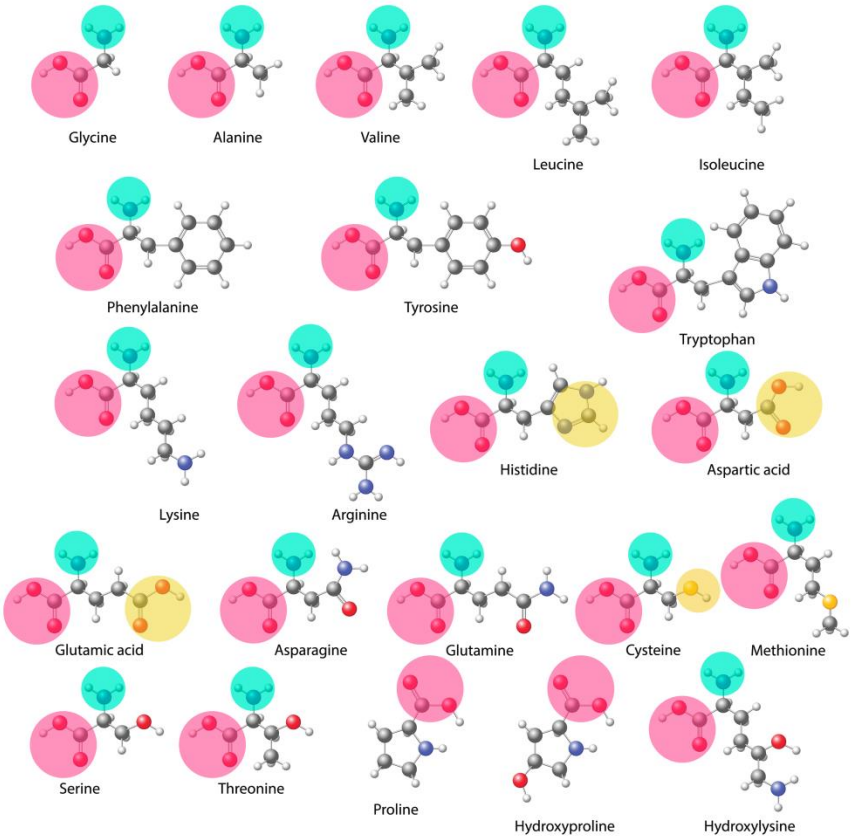

Figure 2 α-amino acids, where different coordinative groups are highlighted

The basic unit of AAs consists on a α-carbon atom onto which an amino group and a α-carboxylic acid group are attached. Metals tend to the typical five-membered glycinate chelate ring leading to the formation of discrete complexes. However, when the α-carboxylate group coordinate metal ions via bi- or tridentate bridging modes extended metal ion–AA frameworks can be created.

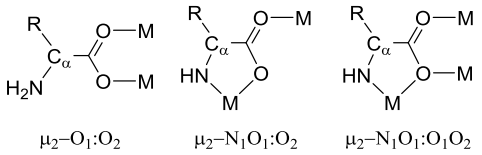

Figure 3 Coordination modes of α-amino acids, where NH_2 and CO_2H are the amino and carboxylic acid groups, respectively, and R is the organic side chain.

1.2.1.1 Pure amino acids

1-D coordination networks based on pure AAs are more common than 2-D or 3-D extended structures. 2-D metal ion–AA frameworks have been obtained, for example, when glycine (**Gly**) coordinates to metal ions (*e.g.* Ni(II),[24] Mn(II),[25] and Co(II)[26]) in a 2/1 fashion. In these 2-D structures, each octahedral metal ion is linked to another four metal ions by four **Gly** ligands adopting a μ_2-O_1:O_2 coordination mode (Figure 3). Another typical connectivity pattern that leads to the formation of 2-D frameworks is when two AA ligands coordinate to an octahedral metal ion in the typical O, N-chelating mode. However, each AA also bridges neighbouring metal ions using the second oxygen atom of its carboxylate (μ_2-N_1O_1:O_2 coordination mode, see **Figure 3**). Examples of these 2-D structures have been obtained by combining L-phenylalanine (Phe) with Mn(II)[27] and Cu(II),[28] L-tryptophan (Trp) with Mn(II)[29] and Ni(II),[30] and L-glutamine (Gln) with Cu(II).[31] More recently, Zhang *et al.* reported two enantiomorphic zeolitic MOFs, Ni(L-ala)$_2$ and Ni(D-ala)$_2$, based on an enantiopure alanine ligand and Ni(II), which show zeotype sodalite topology. Each alanine bridges two Ni(II) ions through the O,N-chelating mode and the second oxen atom of its carboxylate leading to 3D structure.[32]

Some AAs bear R side chains with metal binding groups that favor the increase of dimensionality of the resulting coordination polymer. This R

side chains consist on the β-carboxylate groups of aspartic (**Asp**) and glutamic (**Glu**) acids, the imidazole group of histidine (**His**), the thiol or thioether groups of cysteine (**Cys**) and methionine (**Met**), respectively, or the phenol ring of tyrosine (**Tyr**). These binding groups, in addition to serving as metal binding sites in proteins, allow to bridge metal ions together and further increase the dimensionality of metal ion–AA networks.

Aspartic and glutamic acid that present two carboxylate groups that can bridge metal ions are the most common AA used to produce three dimensional MOFs. MOFs with different metals such as Pb(II),[33] Cd(II),[34, 35] Ni(II),[36] Zn(II),[37, 38] Cu(II)[39, 40] and Co(II) have been reported.[41] As an illustrative example, Anokhina and Jacobson reported the synthesis of homochiral 1-D nickel aspartate oxide helical chains formulated as $[Ni_2O(\textbf{L-Asp})(H_2O)_2]\cdot 4H_2O$.[42] In these chains, each Asp ligand coordinates five Ni(II) ions through its carboxylate and amino groups adopting the μ_2-N_1O_1:O_2 and μ_3-O_3:O_3:O_4 modes. By increasing the pH of the reaction, these helical chains were connected by additional $[NiAsp_2]^{2-}$ units to generate a 3-D porous chiral framework, $[Ni_{2.5}(OH)(\textbf{L-Asp})_2]\cdot 6.55H_2O$, that exhibits 1-D channels with dimensions of 8 × 5 Å.[36] Using the same acid aspartic, Rosseinsky *et al.* described a homochiral AA-derived MOF, $[Zn(\textbf{Asp})]\cdot H_2O$.[37] The connection of 4-, 5-, and 6-coordinated Zn(II) ions through Asp ligands via μ_2-N_1O_1:O_2 and μ_2-O_3:O_4 modes leads to the formation of this 3-D framework with cavities having a volume of 33 $Å^3$.

Pellacani et al. described the 3D [Cu(**L-Asp**)(Im)]·2H2O (where Im is imidazole).[41] This framework is constructed from Cu(II) ions bridged by **Asp** ligands. Each Asp moiety is linked to three Cu(II) ions via the μ_2-

N_1O_1:O_2 and μ_1-O_3 modes. Glutamic acid has one additional methylene group in its side chain than does aspartic acid. Isostructural 3-D MOFs formulated as [M(**L-** or **D-Glu**)(H_2O)]·H_2O (where M is Cd(II),[35] Zn(II),[40] Cu(II),[39] or Co(II)[43]) were synthesized using Glu as briding lingand. In these structures, the Glu ligands serve as multidentate ligands to coordinate to three different metal ions via the μ_2-N_1O_1:O_2, μ_1-O_3:O_4 and μ_2-O_3:O_4 modes; each octahedral metal ion is coordinated with three **Glu** ligands.

Lanthanide ions have also been used as the metal ion component of AA-based MBioFs. The high coordination capacity of lathanide ions favor the production of extended MOFs. 2-D coordination layers constructed from trivalent Dy(III), Ho(III) and Pr(III) ions and Glu ligands as well as from Sm(III) ions and Asp ligands have been described. In addition, Gao *et al.* spatially linked the well-known cubane-like [$Dy_4(\mu_3$-OH)$_4$] lanthanide cluster using Asp ligands to form a 3-D framework formulated as [$Dy_4(\mu_3$-OH)$_4$(**Asp**)$_3$(H_2O)$_8$]·2(ClO_4)·10H_2O.[44] This structure has 1-D parallelogram-shaped channels with dimensions of 4 × 9 Å. Recently, analogous Er(III) and Eu(III)-based MBioFs have been prepared.[45, 46]

Beyond the carboxylic side chain of glutamic and aspartic acid, there are other AAs that feature metal binding groups in their side chains. For instance, Lu et *al.* have used the ability of thioether groups of Met to bind to Ag(I) metal ions to prepare a homochiral heterobimetallic MBioF, [Ag_3Cu_3(**L-Met**)·6(NO_3)$_3$(H_2O)$_3$]·7H_2O.[47] In this structure, L-Met ligands bind to two different types of metal ions: (i) to Cu(II) ions through the hard amino and carboxylate sites via μ_2-N_1O_1:O_2 and simple O,N-chelating modes, and (ii) to Ag(I) ions through the soft

monodentate thioether groups. The distinct coordination preference of metals to specific binding sites on the AA ligand leads to the assembly of a 3-D MBioF constructed from 1-D helical building blocks, featuring homochiral channels that host 1-D chains of water molecules. His has also been employed by Chen and Bu to form a 2-D layered framework.[48] Figure shows a representation of the layers, which are composed of inorganic Zn(II)/HPO_3^{2-} clusters that are further connected to each other by zwitterionic **His** ligands. The use of His as a linker is unusual because it prefers to form 5 or 6 membered rings between metal ions and its amino, carboxylate, or imidazole groups. In this example, Bu *et al.* overcame this tendency by carefully adjusting the pH to obtain the zwitterionic form of His. In this form, the protonated amine group does not coordinate with metal ions, which therefore enables both the imidazole and carboxylate groups to coordinate different metal ions. This discovery will certainly lead to the more prevalent use of His as a bridging AA ligand to obtain 3-D MBioFs in the near future.

1.2.1.2 Modified AA

Natural AAs can also be modified or incorporated to other organic molecules to extend the dimensionality and potential topologies of homochiral metal ion–AA frameworks. For example, while Phe tends to form 1-D and 2-D metal ion–AA structures, modifying its phenyl ring with a tetrazole allows construction of 3-D frameworks. Xiong et al. described the synthesis of two isostructural homochiral networks with non-interpenetrated $SrAl_2$ topologies constructed by linking Zn(II) or Cd(II) ions with this Phe-tetrazole ligand.[49] In this porous structure, each metal ion is coordinated to four of these ligands and each ligand bridges four metal centers through the carboxylate and amino groups

adopting the typical μ_2-N_1O_1:O_2 coordination mode and through the tetrazole moiety. Using a similar approach, Wang et al. further proved that one can control the size and the shape of the grids of 2-D Zn(II) and Cd(II) chiral frameworks by introducing different functionalities to the phenyl ring of Phe.[50] Chiral coordination networks also have been obtained using cysteic acid obtained from Cys.[51] This ligand is able to coordinate Cu(II) and Cd(II) ions through the carboxylate and amino groups adopting the typical μ_2-N_1O_1:O_2 coordination mode and through the SO_3 moiety in a monodentate mode, thus leading to the formation of 3-D frameworks. Wu, *et al.*,[52] synthesized the trimesoyltri(L-alanine) (**L-TMTAH$_3$**) ligand where three alanine groups were incorporated to a phenyl group. They reported the formation of helical three-dimensional MOF, $[Cd_8(\textbf{\textit{L}}\textbf{-TMTA})_6(\textbf{bipy})_3(H_2O)_4]\cdot(H_3O)_2$. Remarkably, each homochiral MOF integrates double helical chains based on ***L*-TMTA** or **D-TMTA** ligands and single helical structures bonded by the achiral 4,4'-bipyridine and cadmium clusters.

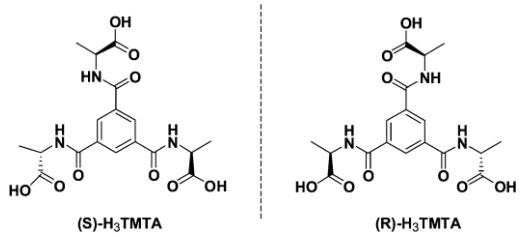

Figure 4 Trimesoyltri(L-alanine) L-TMTAH$_3$ and Trimesoyltri(D-alanine) R-TMTAH$_3$

Each ***L*-TMTA** connects three tetranuclear Cd(II) units through its three carboxylate groups. Two arms of two tripodal ***L*-TMTA** ligands link the same two ion clusters developing a knotted double right-handed helical structures (**Figure 4**). The third ***L*-TMTA** ligand is coordinated to another metal.

1.2.1.3 Auxiliary ligands

Another strategy to get three dimensional AA-derived MOFs is to use an additional organic ligands or inorganic anions/clusters that act as linkers within the metal ion–AA frameworks. To date, some examples of these MOFs have been described.[53-62] An illustrative example was reported by Xu *et al.*, who synthesized a 3-D homochiral MBioF by connecting Cu(II)–L- or D-Pro chains through polyoxometalate $[BW_{12}O_{40}]^{5-}$ clusters.[53] The resulting structure has helical channels with dimensions of 11 × 7 Å. More recently, two non-chiral 3-D MBioFs obtained by bridging Cu(II)–Gly and Cu(II)/Gd(III)–L-Ala chains using azide and 1,3-benzene dicarboxylate ligands, respectively, have also been described. [54, 55]

In addition to the linkage of AA-derived chains, some 3-D pillared MBioFs resulting from the connection of metal ion–Asp layers through bipy-type ligands have been reported. Rosseinsky *et al.* synthesized an enantiopure crystalline nanoporous MOF, $[Ni_2(\mathbf{L\text{-}Asp})_2(\mathbf{4,4'\text{-}bipy})]$·guest (Figure 5), by mixing Ni(**Asp**)·$3H_2O$ salt and 4,4′-bipyridine (**4,4′-bipy**) in a mixture of water and methanol at 150 °C.[56] In this framework, neutral chiral Ni(**L-Asp**) layers are connected by 4,4′-bipy linkers to afford a pillared structure with 1-D sinusoidal channels (3.8 × 4.7 Å) defined by the length of the 4,4′-bipy ligands and the separation between the Ni(II) centers in the Ni(**L-Asp**) layers.

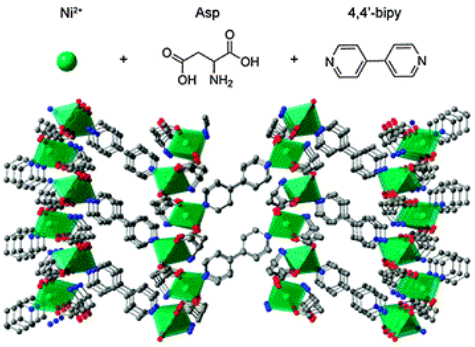

Figure 5 Representation of the metal–Asp framework [Ni_2(L-Asp)$_2$(4,4'-bipy)] resulting from linking Ni–Asp layers by 4,4-bipy ligands. Figure adapted from reference 63.

The Ni(**L-Asp**) layers are formed by octahedrally-coordinated Ni(II) ions linked by Asp ligands, which each bind to one Ni(II) center via μ_2-N_1O_1:O_2 and μ_2-O_3:O_4 modes. Isostructural homochiral MBioFs containing Co(II) ions have also been reported.[57] Interestingly, these MBioFs are stable after removal of the guest solvent, and the pore characteristics (e.g. shape, cross-section, chemical functionality, and volume) can be controlled by substituting the pillaring 4,4′-bipy ligand with extended bipy-type ligands, such as 4,4′-azopyridine (**azpy**), 3,5-bis(4-pyridyl)pyridine (**35bpp**), among others.[58] For example, the pillaring of Ni(**L-Asp**) layers through azpy ligands leads to an analogous structure having nearly linear channels with variable dimensions of 4.1 × 3.8 Å (windows) and 7.8 × 3.7 Å (pores), whereas the use of 35bpp ligands yields a pillared structure with channels whose dimensions range between 6.7 × 4.9 Å and 10.3 × 5.4 Å.

1.2.2 Peptides

A peptide is a compound consisting of two or more amino acids linked in a chain, linked by a peptide bond; the carboxyl group of each acid being

joined to the amino group of the next by a bond of the type -OC-NH. Each peptide has a distinctive sequence depending on the conformation and stereochemical configuration of their constituent AAs. Consequently, they have specific recognition properties and intrinsic chirality that may be useful for a wide range of biological functions but also other applications including asymmetric catalysis and enantioselective separation. Peptides always have an amino terminus and a carboxylic acid terminus, both of which can coordinate metal ions via different coordination modes. The terminal amino group usually coordinates to metal ions in a monodentate or chelating fashion, in which the oxygen atom of the neighbouring amide group also coordinates to the same metal ion forming a five-membered chelate ring. At the opposite peptide terminus, the carboxylate group can coordinate to metal ions in any one of the well-known coordination modes of carboxylic acids (**Figure 6**). Peptides design offers the possibility to incorporate more metal binding groups to their structure by simply adding suitable AAs to their sequence. For example, the incorporation of more carboxylate groups can be achieved simply by synthesizing peptides made from constituent Asp or Glu.

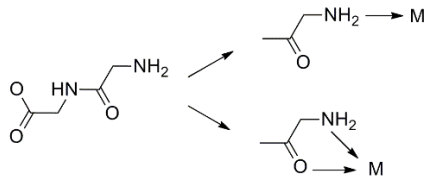

Figure 6 Schematic illustration showing the possible coordination modes of peptides.

If we analyse the literature, we can observe immediately that the number of reported coordination polymers using peptides decrease when the number of AAs monomers of the peptides increase. Takayama

et al. used **GlyGly**, the simplest and shortest peptide first synthesized three metal–peptide frameworks by adjusting the pH values of aqueous solutions containing Zn(II) or Cd(II) metal salts and **GlyGly** peptide.[64] At pH 6, these authors obtained 2-D MBioFs formulated as [M(**GlyGly**)$_2$]·2H$_2$O (where M is Zn(II) or Cd(II)), which are constructed by connecting each octahedral metal ion to four other metal ions through four bridging **GlyGly** ligands. Each **GlyGly** ligand bridges two metal ions through the terminal carboxylate group in a monodentate mode and the terminal amino group through the aforementioned five-membered chelate ring (vide supra). By increasing the pH to 9, a novel 2-D MBioF with formula [Cd(**GlyGly**)$_2$]·H$_2$O was formed. In these layers, the terminal carboxylate groups of **GlyGly** ligands bind to two Cd(II) ions, and their amino groups coordinate to another Cd(II) ion in a monodentate mode. Therefore, each Cd(II) ion is linked to six other Cd(II) ions by four **GlyGly** ligands.

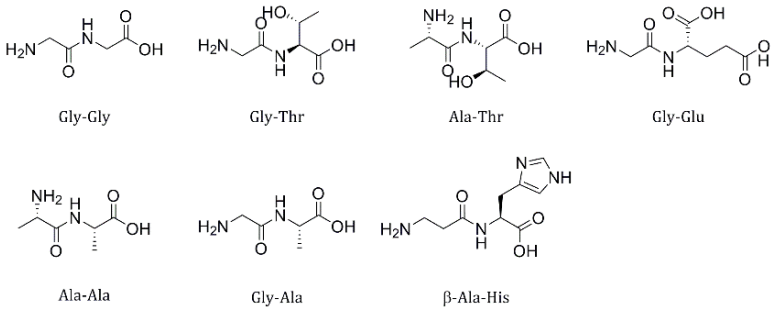

Figure 7 Example of dipeptides used to prepare dipeptide based metal-dipeptide frameworks.

Other metal–peptide networks made from dipeptides using different sequence have been also reported. [Zn(**GlyThr**)$_2$]·2H$_2$O,[65] [Cd(**AlaThr**)$_2$]·4H$_2$O,[66] [Cd(**AlaAla**)$_2$][66] and [Zn(**GlyAla**)$_2$]·solvent[67] consist of metal–peptide sheets connected through strong hydrogen

bonds. Interestingly, these MOFs exhibit a metal–peptide connectivity similar to that observed for [M(**GlyGly**)$_2$]·2H$_2$O,[64] in which each metal ion is connected to four other metal ions through four dipeptide ligands. However, their structures are not identical because of the different coordination spheres (number and configuration) of the metal ions and/or the different metal–peptide coordination modes. While [Zn(**GlyThr**)$_2$]·2H$_2$O and [Cd(**AlaThr**)$_2$]·4H$_2$O have porous structures with 1-D channels resulting from the assembly of square-like 2-D layers through H-bonds, [Cd(**AlaAla**)$_2$] forms a non-porous structure built-up from H-bonded distorted square lattices. Among the dipeptides based MOFs, the most notable is probably [Zn(**GlyAla**)$_2$]·solvent, which was recently reported by Rosseinsky *et al.*[67] Each GlyAla ligand coordinates to the tetrahedral Zn(II) ions by the terminal carboxylate group of the Ala residue and the terminal amino groups of the Gly residue, both in a monodentate mode. The layers are then aligned in an A–A fashion by hydrogen bonds to form a porous structure with square-shaped 1-D pores (solvent-accessible volume: 532.7 Å^3 per unit cell at 100 K (28%). Remarkably, this porous MOF has an adaptable porosity, in which its crystal structure undergoes reversible structural changes after desorption/reabsorption of solvent molecules. The same authors reported porous 3D framework synthesized from Zn^{2+} and the natural dipeptide carnosine (**β-ala-his**) (Figure 8a). Unlike previous extended peptide networks, in this structure the imidazole side chain of the histidine residue is deprotonated to afford Zn–imidazolate chains, with bonding similar to the zeolitic imidazolate framework (ZIF) family of porous materials. Zn(**β-ala-his**) exhibits permanent microporosity with a surface area of 448 m^2 g^{-1}, and its pores are 1D channels with 5 Å

openings and a characteristic chiral shape. This compound is chemically stable in organic solvents and water.

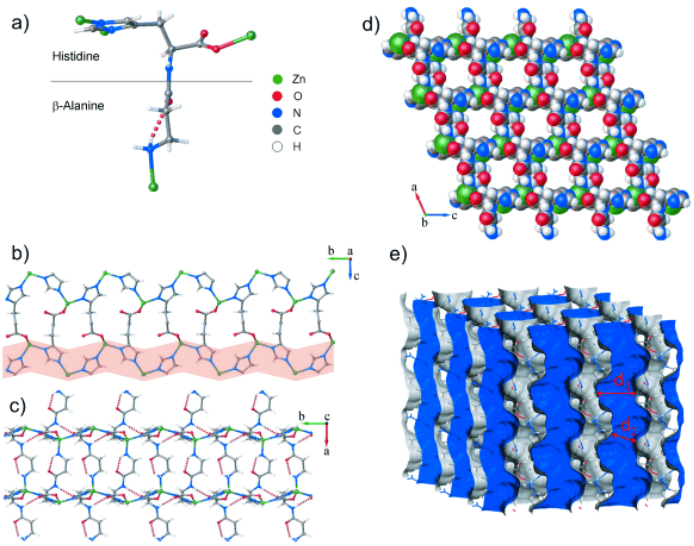

Figure 8 Different views of Zn(β-ala-his) metal-biomolecule framework

The substitution of one of the two constituent AAs of the dipeptides lead to the formation of different metal–peptide structures. Using the **GlyGlu** peptide Gasque *et al.* synthesized two MOFs connecting the peptide with Pb(II) or Cd(II).[68] The first material has a 2-D metal–peptide framework, in which both carboxylate groups of each Glu residue coordinate to four Pb(II) ions in a tridentate mode. The second is a 3-D porous MBioF, [Cd(**GlyGlu**)$_2$]·3H_2O, that has 1-D channels. In this structure, each octahedral Cd(II) ion is linked in three dimensions to four other Cd(II) ions by four **GlyGlu** ligands. The amino groups do not participate in the coordination of Cd(II) ions, and only the carboxylate groups of the Glu residue bind to Cd(II) ions in a bidentate mode. Interestingly, the simple

addition of a metal-binding site to the peptides allows the formation of 3-D metal–peptide frameworks.

The same **GlyGlu** was combined to Co(II) ions by Maspoch *et al.*, to produce 1-D homochiral metal-organic chiral ladders that can be used as 1-D building blocks.[69] The infinite ladder units are constructed from the connection of octahedral Co(II) centres through L-GG linkers. Each L-GG coordinates to three Co(II) centers, whereas each Co(II) center is bound to four O atoms (three from the carboxylate groups, and one from the carbonyl group) and one N-atom (from the terminal amino group) of three consecutive L-GG linkers, and to one H_2O molecule, which points towards the neighbouring 1D chains along the c-axis. In this configuration, the Co(II) ions are positioned at the vertices of the Co-L-**GlyGlu** ladders. Adding N-donor spacer ligands in the reactions these Co-**GlyGlu** ladders were connected and spaced through the Co(II) ions positioned at the vertices allowing the engineering of homochiral porous MOFs with enhanced pore sizes, pore volumes, and surface areas.

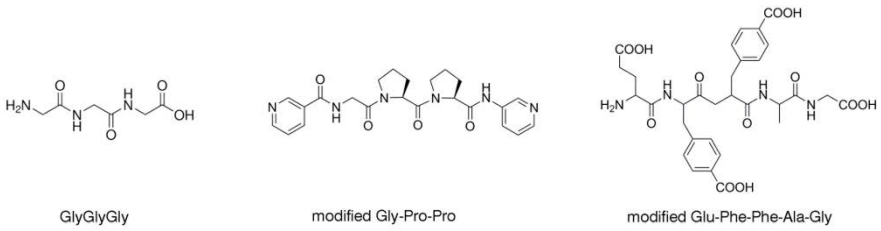

Figure 9 Example of polypeptides used to prepare tripeptide and polypeptide based metal-polypeptide frameworks.

If we analyse the literature we observe that MOFs made of peptides with more than two monomers are very rare. The first MOFs made of a

tripetided was reported by Marsh *et al.* who used the tripeptide GlyGlyGly (**Figure 9**) to synthesize a 2-D MBioF with formula $[Cd(\mathbf{GlyGlyGly})_2]\cdot 2H_2O$.[66] From a structural point of view, this structure is similar to that of $[Cd(\mathbf{GlyGly})_2]\cdot H_2O$ (pH = 9) reported by Takayama *et al.*[64] We can find as far as we know two more metal-peptide frameworks reported by Yaghi *et al.* and Fujita *et al.* In both cases the peptides were slightly tuned to favour the formation of extended coordination polymers. Yaghi *et al.* used the pentapeptide **NH_2-Glu-pCO_2Phe-pCO_2Phe-Ala-Gly-OH** in which two phenyalanine AA are replaced by two 4–carboxyphenylalanine monomers to create a ladder like structure (**Figure 10a**).[70] The metal-peptide framework is constructed of two infinite cadmium chains linked by a pentapeptide in a double-ladder fashion which progress along the [010] axis of the unit cell. Furthermore, during the assembly process the Glu amino acid at the amine end of **NH_2-Glu-pCO_2Phe-pCO_2Phe-Ala-Gly-OH** reacted in an intramolecular fashion to form a 2-pyrrolidone moiety, as is evident from the crystal structure, to form **pyrrolidone-pCO_2Phe-pCO_2Phe-Ala-Gly-OH**. More recently, Fujita *et al.* modified the short peptide **Gly-Pro-Pro** to generate a coordinative ligand by the introduction of 3-pyridyl groups (py) with amide bonds at both termini. In the resulting coordination polymer Ag(I) are coordinated to the peptide ligand through the pyiridyl moieties (**Figure 10b**).[71] The resulting material possesses two types of unique helical nano-channel. Guest uptake properties were investigated by soaking the crystals in polar solutions of guest molecules; anions, organic chiral molecules, and bio-oligomers are effectively encapsulated by this peptide-folded porous crystal, with moderate to high chiral recognition for chiral molecules.

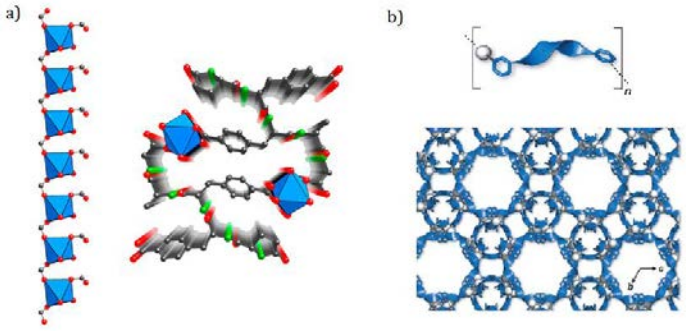

Figure 10 a) View of the crystalline 1D metal-polypeptide ladder like framework (from reference [70]), and b) View of a crystalline networked structure produce by reaction of Gly-Pro-Pro ligand with AgBF4 (from reference [71]).

1.2.3 Nucleobases

Nucleobases are other kind of bio-building block used in the formation of coordination polymers. Nucleobases are key constituents of nucleic acids that are involved in base-pairing; that is, adenine (Ade) binds to thymine or uracil with the help of two H-bonds, whereas guanine specifically recognizes cytosine through three H-bonds. In addition, nucleobases also have accessible nitrogen and oxygen electron lone pairs which allow these molecules to act as multidentate organic ligands. Their rich metal binding and H-bonding capabilities, together with the rigidity of their molecular structures, make them ideal bio-linkers for constructing topologically diverse families of MBioFs. In particular, adenine nucleobase, has showed to be a fruitful linker in the synthesis complexes. As an illustrative example of adenine coordination polymers, the Figure 11 shows the projection of the anionic porous framework, $[Zn_8(\mathbf{ade})_4(\mathbf{bpdc})_6O{\cdot}2Me_2NH_2]{\cdot}8DMF{\cdot}11H_2O$ reported by An *et al.*. Called bio-MOF-1, it consists of infinite Zn(II)–Ade columns

composed of apex-sharing Zn(II)–Ade octahedral cages. Nucleobase coordination polymers will be discussed in detail in **Chapter 4**.

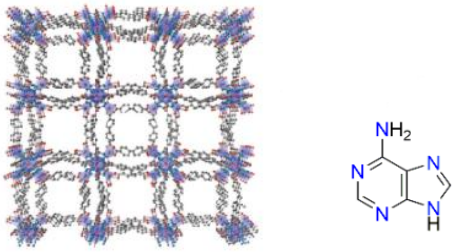

Figure 11 Projection of the metal-biomolecules frameworks of $[Zn_8(Ade)_4(bpdc)_6O{\cdot}2Me_2NH_2]{\cdot}8DMF{\cdot}11H_2O$ (Adapted from reference 63)

1.2.4 Other molecules

Besides Amino acids, peptides, proteins and nucleobases that one typically recognizes as biomolecules, there are also many other molecules present in humans, animals or plants. For example, some molecules containing carboxylic acids such as formic and oxalic acids and fumaric, glutaric, malic and succinic acids play key roles as intermediates in the Krebs cycle, which is of central importance in all living cells. All of these linkers have been extensively used to obtain a wide diversity of metal–organic frameworks. For this reason, a number of excellent reviews have been recently published detailing this area. As an illustrative example Férey et al. reported a 3-D Fe(III) fumarate open-framework with formula $[Fe_3O(MeOH)_3(fum)_3(CO_2CH_3)]{\cdot}4.5MeOH$.[72] This framework has trimeric clusters connected to each other through fumarate ligands. Each cluster is formed by three octahedral Fe(III) ions bridged by six fumarate dianions. The resulting structure has a 1-D pore channel system that is filled with solvent and cages that are filled with

acetate groups. Interestingly, this structure exhibits unique swelling behaviour upon adsorption of water and various alcohols.[73]

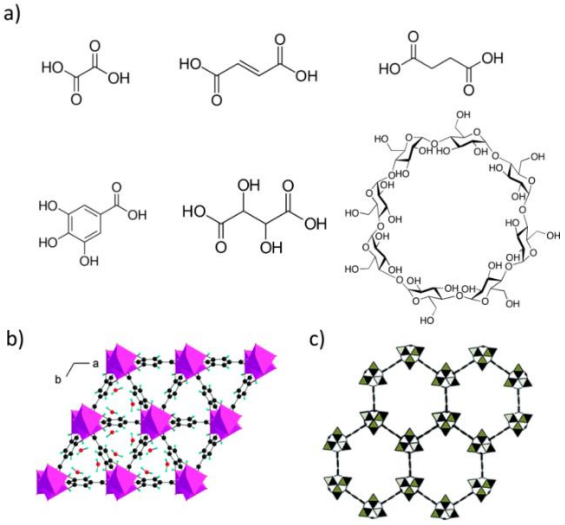

Figure 12 Representation of biomolecules used as linkers in MOF synthesis. a) From left to right: oxalic acid, fumaric acid, succinic acid, 3,4,5-trihydroxybenzoic acid, tartaric acid, and γ–cyclodextrin. b) View of structure $Mg(H_2gal)\cdot 2H_2O$ (From reference 74) and c) View of structure (From reference).

Same authors, reported a microporous magnesium gallate MOF (Figure 12b), the $Mg(H_2gal)\cdot 2H_2O$, was prepared from gallic acid, a type of phenolic acid, found in gallnuts, sumac, witch hazel, tea leaves, oak bark, and other plant . The structure consists of chains of corner sharing MgO_6 distorted octahedra (four oxygen atoms coming from the phenol groups and two from the carboxyl functions) connected through the gallic acid which define small channels containing water molecules.[74]

Finally, saccharides (carbohydrates) that are divided into monosaccharides and disaccharides (sugars), oligosaccharides, and polysaccharides have also been used to synthesize biomolecule based frameworks. Saccharides perform numerous roles in living systems,

ranging from energy storage (*e.g.* starch and glycogen) to providing structure (*e.g.* cellulose in plants and chitin in arthropods). Stoddart *et al.* have recently reported a very exciting study that exploits their use as multidentate organic ligands to form functional MBioFs.[75] These authors reported two metal–saccharide frameworks synthesized from γ-cyclodextrin (γ-CD), a symmetrical cyclic oligosaccharide that is mass-produced enzymatically from starch and comprises eight asymmetric α-1,4-linked D-glucopyranosyl residues. Both frameworks, which have the empirical formula [(γ-CD)$(MOH)_2$] (where M is K or Rb), are constructed from six γ-CD units connected into (γ-CD) 6 cubes through the metal ions. These cubes are further linked by the alkali metal K^+ or Rb^+, leading to a porous framework in which apertures of 0.78 nm provide access to larger spherical voids of 1.7 nm at the center of each γ-CD (**Figure 13**). Remarkably, both structures are permanently porous after heating to nearly 200 °C and exhibit BET surface areas of 1220 g cm^{-3} (K^+) and 1030 g cm^{-3} (Rb^+).

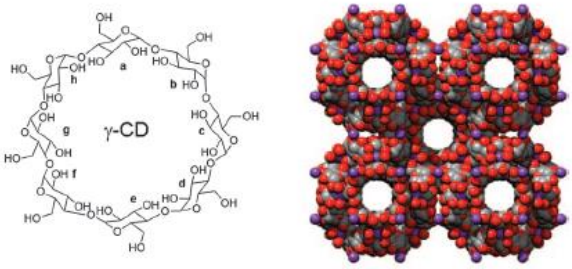

Figure 13 Representation of γ-cyclodextrin (γ-CD) (left), and the porous structure of (γ-CD)$(KOH)_2$ (From reference 75)

1.3 New properties of biomolecule based MOFs

As a subclass of MOFs, MBioFs can exhibit porous structures with high internal surface areas, high porosities, and tailorable pore sizes. In these sections, rather than focusing on these properties which are expected to be similar to those exhibited by MOFs, we will review some examples in which the use of biomolecules improves upon current MOF capabilities or introduces new potential applications.

1.3.1 Storage

It is well known that the sorption and storage capabilities of metal–organic materials are directly related to their structural characteristics. An important characteristic of most of biomolecules is that they are flexible molecules. Flexibility is sometimes a hindrance to the preparation of robust porous frameworks, but it can also be an excellent characteristic for designing flexible porous frameworks which can serve as responsive and adaptable materials.[53, 76] A first example of this class of materials has been recently reported by Rosseinsky et al.,[67] who synthesized the adaptable porous $[Zn(GlyAla)_2]\cdot$(solvent) (**Figure 14**). Once desolvated, neighbouring peptides within the structure hydrogen bond together, which in turn occludes the pores, as confirmed by the inability of the material to adsorb N_2 and H_2 at 77 K. However, these pores gradually and cooperatively open when triggered by small molecules having polar bonds, including water, MeOH and CO_2. This behaviour is a direct consequence of the flexibility of GlyAla, because the torsional degrees of freedom of these dipeptide ligands, which strongly depend on their interaction with guest molecules, allow the methyl group to impact the accessible void volume. For example, when CO_2

molecules penetrate the pores, the hydrogen bonds between neighbouring peptides break because of the repulsion between the methyl group and CO_2.

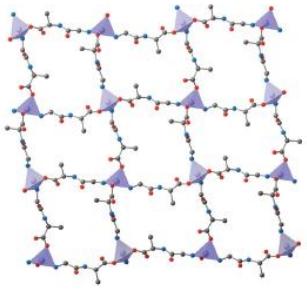

Figure 14 Representation of one layer of $[Zn(GlyAla)_2]$. (From reference 63)

Another example, the structure Zn(**β-ala-his**) reported by the same authors present similar flelixibility. Zn(**β-ala-his**) is chemically stable in organic solvents and water. Single-crystal X-ray diffraction (XRD) study showed that the ZnCar framework adapts to MeOH and H_2O guests because of the torsional flexibility of the main His-Ala chain, while retaining the rigidity conferred by the Zn–imidazolate chains. The conformation adopted by carnosine is driven by the H bonds formed both to other dipeptides and to the guests, permitting the observed structural transformations.

1.3.2 Catalysis and separation

One of the most important property of biomolecules is that they can act as chiral ligands to induce the formation of homochiral MBioFs. This property together with the above-mentioned adsorption capabilities opens the possibility to use MBioFs for heterogeneous asymmetric catalysis and enantioselective separation.[77]

In 2006, Rosseinsky et al. showed that the [Ni_2(L-Asp)$_2$(4,4′-bipy)]·guest (**Figure 5**) exhibits significant enantioselective sorption capabilities of small chiral diols,[56] with levels of enantioselectivity as high as 53.7% ee (enantioselective excess) for the sorption of 2-methyl-2,4-pentane-diol. Recently, the same authors also introduced Brønsted acidic –COOH sites into the same family of chiral porous MBioFs via post-synthetic modification for heterogeneous asymmetric catalytic methanolysis of cis-2,3-epoxybutane.[78] Treatment of the [Ni_2(L-Asp)2(4,4′-bipy)]·guest and [Cu_2(L-Asp)2(bpe)]·guest (where bpe is 1,2-bis(4-pyridyl)ethane) with HCl in Et2O affords the protonated [Ni_2(L-Asp)2(4,4′-bipy)·(HCl)1.8(MeOH)] and [Cu_2(L-Asp)$_2$(bpe)·(HCl)2·(H2O)2] frameworks. Both resulting materials are active as heterogeneous asymmetric catalysts for the methanolysis of rac-propylene oxide. Figure 15 illustrates that the porous Cu(II)-based MBioF also shows good catalytic activity for the methanolysis of other epoxides. Its chiral induction ability, however, is modest, and the best results were observed for the methanolysis of the cis-2,3-epoxybutane that afforded 3-methoxybutan-2-ol with a modest 17% ee.

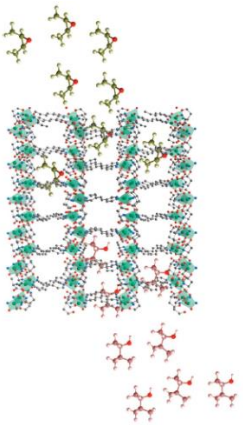

Figure 15 Schematic illustration of the methanolysis of epoxides (cis-2,3-epoxybutane) using [Cu2(L-Asp)$_2$(bpe)·(HCl)$_2$·($_{H2}$O)$_2$] as an heterogeneous asymmetric catalyst. (From reference 63)

Kim and Fedin *et al.* also have studied the enantioselective separation and catalytic properties of [Zn_2(bdc)(L-lac)(DMF)·DMF] (where bdc is 1,4-benzendicarboxylic acid and L-lac is L-lactic acid).[79] When this MBioF is stirred in the presence of racemic mixtures of sulfoxides, the resulting material shows high enantioselective adsorption capability to sulfoxides with smaller substituents. The ee values for these adsorbed sulfoxides were between 20 and 27% with excess of the S enantiomer in all cases. In addition, the same MBioF shows excellent size- and chemoselective catalytic oxidation of thiothers to sulfoxides by urea hydroperoxide or hydrogen peroxide. These interesting results inspired Fedin and Bryliakov *et al.* to fabricate the first chiral chromatographic column for the separation of racemic mixtures of chiral alkyl aryl sulfoxides using this enantiopure MBioF as the stationary phase.[80] Also, by combining its chromatographic and catalytic properties, the authors developed a one-pot process for the synthesis of enantiomerically pure sulfoxides.

1.3.3 Biomedical applications

The molecular storage-release capabilities and potential biocompatibility of MBioFs together with the possibility to miniaturize them to the submicron length scale are excellent characteristics that allow these materials to be exploited as novel delivery systems for active species (*e.g.* drugs, vaccines, genes, etc.) in the fields of medicine, pharmaceutics and cosmetics. Thus far, however, such biomedical applications have not been fully explored, and only some examples of MBioFs that can adsorb and release drugs have been reported. A possible explanation is that many examples of MBioFs stable in aqueous and buffer conditions are not yet known. For instance, Rosi et al. demonstrated controlled drug release of $[Zn_8(Ade)_4(bpdc)_6O{\cdot}2Me_2NH_2]{\cdot}8DMF{\cdot}11H_2O$.[81] This MBioF is modestly stable in water and biological buffers for several weeks; however, its toxicity is still unknown. Procainamide, which is a cationic drug molecule, was loaded into the pores of material via cationic exchange with the dimethylammonium cations that initially reside inside the pores (Fig. 16). In addition, procainamide release was monitored in PBS buffer, and it was shown that cation exchange of drug molecules with cations within the buffer likely played a role in the drug release process. It was shown that 0.22 g of procainamide per gram of MBioF was loaded and that drug release was completed after ~3 days.

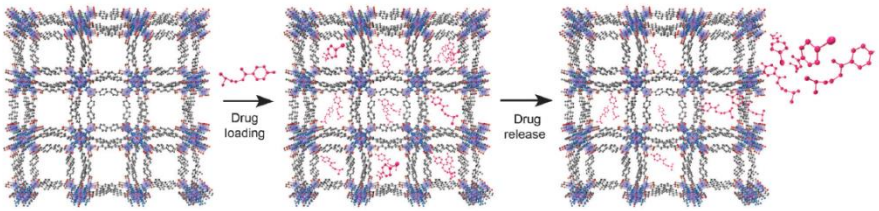

Figure 16 Schematic illustration showing the use of MBioF, $[Zn_8(Ade)_4(bpdc)_6O{\cdot}2Me_2NH_2]$, as drug delivery carriers. (From reference 63)

Similarly, Horcajada *et al.* have recently reported various excellent studies that proves the promising use of submicron crystals of MBioFs as platforms for drug delivery and imaging.[82] They showed that two MBioFs, such as $[Fe_3O(MeOH)_3(fumarate)_3(CO_2CH_3)]{\cdot}4.5MeOH$ and $[Fe_3O(MeOH)(C_6H_4O_8)_3Cl]{\cdot}6MeOH$ (where $C_6H_4O_8$ is galactarate), could adsorb appreciable amounts of several drugs (*e.g.* busulfan, azidothymidine triphosphate and cidofovir). The loading was achieved by soaking both MBioFs in saturated drug solutions. Interestingly, in both cases, the successful design of the drug delivery system was confirmed by proving the controlled and progressive release of the encapsulated drug as well as their in vitro anticancer efficacies. Finally, and very importantly, these authors also proved that the degradation of these MBioFs produces endogenous substances, thus minimizing their toxicity. For example, the fumarate-derived MBioF degrades after seven days of incubation at 37 °C, releasing large quantities of their ligands (72% of fumaric acid) and Fe(III) ions. These major degradation products are endogenous, and consequently, the toxicity values are low [LD50(Fe(III)) = 30 g kg−1 and LD50 (fumaric acid) = 10.7 g kg−1]. The low toxic effects of these MBioFs were further demonstrated by in vivo

subacute toxicity assays done by injecting up to 150 mg of sub-micron crystals during four consecutive days.

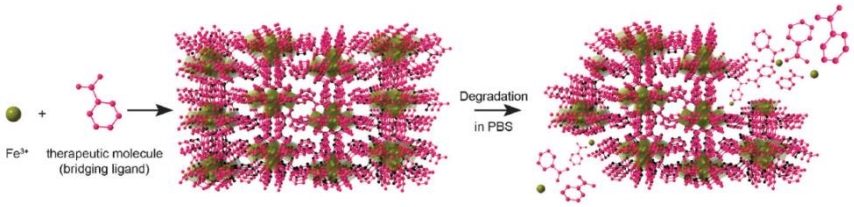

Figure 17 The use of therapeutic species as bridging organic ligands to build up the MBioF; the therapeutic species are released as the MBioF degrades. (From reference 63)

Although MOFs were initially considered for controlled drug release through mainly physisorption processes, the incorporation of an active biomolecule within the framework and its release by degradation of the framework itself was also reported by the same authors with the Mg(H_2gal) MOF. Thus, the authors demonstrated that the solid degrades in physiological fluids, slowly releasing gallic acid and leading to strong antioxidant activity, as highlighted in the case of HL-60 cells.

1.3.4 Sensors

MBioFs have two major advantages that render them useful as novel sensors. First, they can be permanently porous structures and can exhibit high surface areas. Second, interactions between guest molecules and the pores of metal–organic structures can induce changes in their physical properties. Third, some biomolecules (*e.g.* peptides, antibodies) have the ability to recognize specific analytes. Thus far, however, few sensors based on MBioFs have been reported, and only the porous anionic [$Zn_8(Ade)_4(bpdc)_6{\cdot}O{\cdot}2Me_2NH_2$] framework loaded with lanthanide cations has shown promise for serving as a photostable O2 sensor (**Figure 18**).[83]

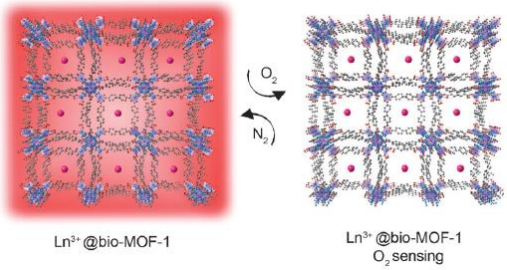

Figure 18 Schematic illustration showing the potential use of $[Zn_8(Ade)_4(bpdc)_6 \cdot O \cdot 2Me_2NH_2]$ as a O_2 sensor. (From reference 63)

This MBioF is able to incorporate lanthanide ions (e.g.Tb(III), Sm(III), Eu(III) and Yb(III)) simply by soaking it in DMF solutions of nitrate salts of these ions. Importantly, the resulting materials are luminescent, even in water, a property that can be used to detect O2 and that points toward their potential applicability as intracellular O2 sensors. Indeed, when a sample of Yb(III)-loaded MBioF was exposed to O2 gas, an approximate 40% decrease in Yb(III) luminescence was observed within the first 5 minutes. Interestingly, the total signal intensity was recovered after exposing this material to N2. Importantly, this experiment was reversible after several cycles of exposure to O2 and N2. We also note that the near-infrared luminescence of Yb(III) is ideal for biological samples, which are re virtually transparent to NIR radiation.

1.4 References

1. A. Kraft, *Bull. Hist. Chem.*, 2008, **33**, 61-67.
2. H. J. Buser, D. Schwarzenbach, W. Petter and A. Ludi, *Inorganic Chemistry*, 1977, **16**, 2704-2710.
3. J. Maddox, *Nature*, 1988, **335**, 201-201.
4. J. M. Lehn, *Pure and Applied Chemistry*, 1978, **50**, 871-892.
5. M. C. Etter, *Accounts of Chemical Research*, 1990, **23**, 120-126.
6. G. R. Desiraju, *Crystal engineering: the design of organic solids*, Elsevier, 1989.
7. A. F. Wells, *Three dimensional nets and polyhedra*, Wiley, 1977.
8. B. F. Hoskins and R. Robson, *Journal of the American Chemical Society*, 1990, **112**, 1546-1554.
9. B. F. Hoskins and R. Robson, *Journal of the American Chemical Society*, 1989, **111**, 5962-5964.
10. O. M. Yaghi and H. Li, *Journal of the American Chemical Society*, 1995, **117**, 10401-10402.
11. J. L. C. Rowsell and O. M. Yaghi, *Microporous and Mesoporous Materials*, 2004, **73**, 3-14.
12. M. Eddaoudi, D. B. Moler, H. Li, B. Chen, T. M. Reineke, M. O'Keeffe and O. M. Yaghi, *Accounts of Chemical Research*, 2001, **34**, 319-330.
13. R. Kitaura, K. Seki, G. Akiyama and S. Kitagawa, *Angewandte Chemie International Edition*, 2003, **42**, 428-431.
14. S. Kitagawa, R. Kitaura and S.-i. Noro, *Angewandte Chemie International Edition*, 2004, **43**, 2334-2375.
15. P. J. Hagrman, D. Hagrman and J. Zubieta, *Angewandte Chemie International Edition*, 1999, **38**, 2638-2684.
16. G. Férey, *Chemistry of Materials*, 2001, **13**, 3084-3098.
17. C. Janiak, *Dalton Transactions*, 2003, DOI: 10.1039/b305705b, 2781-2804.
18. R. Batten Stuart, R. Champness Neil, X.-M. Chen, J. Garcia-Martinez, S. Kitagawa, L. Öhrström, M. O'Keeffe, M. Paik Suh and J. Reedijk, *Journal*, 2013, **85**, 1715.
19. D. Bradshaw, J. B. Claridge, E. J. Cussen, T. J. Prior and M. J. Rosseinsky, *Accounts of Chemical Research*, 2005, **38**, 273-282.
20. D. Bradshaw, A. Garai and J. Huo, *Chemical Society Reviews*, 2012, **41**, 2344-2381.
21. O. M. Yaghi, M. O'Keeffe, N. W. Ockwig, H. K. Chae, M. Eddaoudi and J. Kim, *Nature*, 2003, **423**, 705-714.

22. S. Furukawa, J. Reboul, S. Diring, K. Sumida and S. Kitagawa, *Chemical Society Reviews*, 2014, **43**, 5700-5734.
23. B. D. Glisic, U. Rychlewska and M. I. Djuran, *Dalton Transactions*, 2012, **41**, 6887-6901.
24. M. Fleck and L. Bohaty, *Acta Crystallographica Section C*, 2005, **61**, m412-m416.
25. R. Mrozek, Z. Rza˛czyńska, M. Sikorska-Iwan and T. Głowiak, *Journal of Chemical Crystallography*, 1999, **29**, 803-808.
26. K. Stenzel and M. Fleck, *Acta Crystallographica Section E*, 2004, **60**, m1470-m1472.
27. J. B. H. Weng, M. C.; Cao, R.; Shi, Q.; Chan, A. S. C., *Chin. J. Struct. Chem.*, 2003, **22**, 195-199.
28. D. Van der Helm, M. B. Lawson and E. L. Enwall, *Acta Crystallographica Section B*, 1971, **27**, 2411-2418.
29. Y. Xie, H.-H. Wu, G.-P. Yong and Z.-Y. Wang, *Acta Crystallographica Section E*, 2006, **62**, m2089-m2090.
30. J. Wang, X. Xu, W. Ma, L. Lu and X. Yang, *Acta Crystallographica Section E*, 2007, **63**, m2867-m2868.
31. José M. Schveigkardt, Alberto C. Rizzi, Oscar E. Piro, Eduardo E. Castellano, Ricardo Costa d. Santana, R. Calvo and Carlos D. Brondino, *European Journal of Inorganic Chemistry*, 2002, **2002**, 2913-2919.
32. E. Yang, L. Wang, F. Wang, Q. Lin, Y. Kang and J. Zhang, *Inorganic Chemistry*, 2014, **53**, 10027-10029.
33. L. Gasque, S. Bernès, R. Ferrari, C. R. de Barbarín, M. de Jesús Gutiérrez and G. Mendoza-Díaz, *Polyhedron*, 2000, **19**, 649-653.
34. L. Gasque, S. Bernès, R. Ferrari and G. Mendoza-Díaz, *Polyhedron*, 2002, **21**, 935-941.
35. R. J. Flook, H. C. Freeman and M. L. Scudder, *Acta Crystallographica Section B*, 1977, **33**, 801-809.
36. E. V. Anokhina, Y. B. Go, Y. Lee, T. Vogt and A. J. Jacobson, *Journal of the American Chemical Society*, 2006, **128**, 9957-9962.
37. J. A. Gould, J. T. A. Jones, J. Bacsa, Y. Z. Khimyak and M. J. Rosseinsky, *Chemical Communications*, 2010, **46**, 2793-2795.
38. C. Gramaccioli, *Acta Crystallographica*, 1966, **21**, 600-605.
39. M. Mizutani, N. Maejima, K. Jitsukawa, H. Masuda and H. Einaga, *Inorganica Chimica Acta*, 1998, **283**, 105-110.
40. C. M. Gramaccioli and R. E. Marsh, *Acta Crystallographica*, 1966, **21**, 594-600.
41. L. Antolini, G. Marcotrigiano, L. Menabue, G. C. Pellacani and M. Saladini, *Inorganic Chemistry*, 1982, **21**, 2263-2267.

42. E. V. Anokhina and A. J. Jacobson, *Journal of the American Chemical Society*, 2004, **126**, 3044-3045.
43. Y. Zhang, M. K. Saha and I. Bernal, *CrystEngComm*, 2003, **5**, 34-37.
44. B.-Q. Ma, D.-S. Zhang, S. Gao, T.-Z. Jin, C.-H. Yan and G.-X. Xu, *Angewandte Chemie International Edition*, 2000, **39**, 3644-3646.
45. R. Wang, H. Liu, M. D. Carducci, T. Jin, C. Zheng and Z. Zheng, *Inorganic Chemistry*, 2001, **40**, 2743-2750.
46. H.-y. Zhang, H.-j. Yu, H.-x. Xu, J.-s. Ren and X.-g. Qu, *Polyhedron*, 2007, **26**, 5250-5256.
47. T.-T. Luo, L.-Y. Hsu, C.-C. Su, C.-H. Ueng, T.-C. Tsai and K.-L. Lu, *Inorganic Chemistry*, 2007, **46**, 1532-1534.
48. L. Chen and X. Bu, *Chemistry of Materials*, 2006, **18**, 1857-1860.
49. Z.-R. Qu, H. Zhao, X.-S. Wang, Y.-H. Li, Y.-M. Song, Y.-j. Liu, Q. Ye, R.-G. Xiong, B. F. Abrahams, Z.-L. Xue and X.-Z. You, *Inorganic Chemistry*, 2003, **42**, 7710-7712.
50. Y. Xie, Z. Yu, X. Huang, Z. Wang, L. Niu, M. Teng and J. Li, *Chemistry – A European Journal*, 2007, **13**, 9399-9405.
51. H.-Y. Li, F.-P. Huang, Y.-M. Jiang and X.-J. Meng, *Inorganica Chimica Acta*, 2009, **362**, 1867-1871.
52. X. Wu, H.-B. Zhang, Z.-X. Xu and J. Zhang, *Chemical Communications*, 2015, **51**, 16331-16333.
53. H.-Y. An, E.-B. Wang, D.-R. Xiao, Y.-G. Li, Z.-M. Su and L. Xu, *Angewandte Chemie International Edition*, 2006, **45**, 904-908.
54. Z.-L. Chen, C.-F. Jiang, W.-H. Yan, F.-P. Liang and S. R. Batten, *Inorganic Chemistry*, 2009, **48**, 4674-4684.
55. F. Luo, Y.-t. Yang, Y.-x. Che and J.-m. Zheng, *CrystEngComm*, 2008, **10**, 1613-1616.
56. R. Vaidhyanathan, D. Bradshaw, J.-N. Rebilly, J. P. Barrio, J. A. Gould, N. G. Berry and M. J. Rosseinsky, *Angewandte Chemie International Edition*, 2006, **45**, 6495-6499.
57. P. Zhu, W. Gu, F.-Y. Cheng, X. Liu, J. Chen, S.-P. Yan and D.-Z. Liao, *CrystEngComm*, 2008, **10**, 963-967.
58. J. Perez Barrio, J.-N. Rebilly, B. Carter, D. Bradshaw, J. Bacsa, A. Y. Ganin, H. Park, A. Trewin, R. Vaidhyanathan, A. I. Cooper, J. E. Warren and M. J. Rosseinsky, *Chemistry – A European Journal*, 2008, **14**, 4521-4532.
59. M. J. Ingleson, J. Bacsa and M. J. Rosseinsky, *Chemical Communications*, 2007, DOI: 10.1039/B706557D, 3036-3038.
60. B. Wisser, Y. Lu and C. Janiak, *Zeitschrift für anorganische und allgemeine Chemie*, 2007, **633**, 1189-1192.

61. G. Aromí, J. J. Novoa, J. Ribas-Ariño, S. Igarashi and Y. Yukawa, *Inorganica Chimica Acta*, 2008, **361**, 3919-3925.
62. A. Ghosh and R. A. Sanguramath, *Journal of Chemical Sciences*, 2008, **120**, 217-222.
63. I. Imaz, M. Rubio-Martinez, J. An, I. Sole-Font, N. L. Rosi and D. Maspoch, *Chemical Communications*, 2011, **47**, 7287-7302.
64. T. Toshio, O. Shirabe, K. Yoshio, W. Masanobu, H. Daisuke and O. Yuji, *Bulletin of the Chemical Society of Japan*, 1996, **69**, 1579-1586.
65. U. Eriko, Y. Yutaka, K. Noriko, T. Makoto, S. Hiromu, K. Naemi and K. Yoshitane, *Bulletin of the Chemical Society of Japan*, 2004, **77**, 981-986.
66. H.-Y. Lee, J. W. Kampf, K. S. Park and E. N. G. Marsh, *Crystal Growth & Design*, 2008, **8**, 296-303.
67. J. Rabone, Y.-F. Yue, S. Y. Chong, K. C. Stylianou, J. Bacsa, D. Bradshaw, G. R. Darling, N. G. Berry, Y. Z. Khimyak, A. Y. Ganin, P. Wiper, J. B. Claridge and M. J. Rosseinsky, *Science*, 2010, **329**, 1053-1057.
68. R. Ferrari, S. Bernés, C. R. de Barbarín, G. Mendoza-Díaz and L. Gasque, *Inorganica Chimica Acta*, 2002, **339**, 193-201.
69. K. C. Stylianou, L. Gómez, I. Imaz, C. Verdugo-Escamilla, X. Ribas and D. Maspoch, *Chemistry – A European Journal*, 2015, **21**, 9964-9969.
70. D. Peri, J. Ciston, F. Gándara, Y. Zhao and O. M. Yaghi, *Inorganic Chemistry*, 2013, **52**, 13818-13820.
71. T. Sawada, A. Matsumoto and M. Fujita, *Angewandte Chemie International Edition*, 2014, **53**, 7228-7232.
72. C. Serre, F. Millange, S. Surblé and G. Férey, *Angewandte Chemie International Edition*, 2004, **43**, 6285-6289.
73. C. Serre, C. Mellot-Draznieks, S. Surblé, N. Audebrand, Y. Filinchuk and G. Férey, *Science*, 2007, **315**, 1828-1831.
74. L. Cooper, T. Hidalgo, M. Gorman, T. Lozano-Fernandez, R. Simon-Vazquez, C. Olivier, N. Guillou, C. Serre, C. Martineau, F. Taulelle, D. Damasceno-Borges, G. Maurin, A. Gonzalez-Fernandez, P. Horcajada and T. Devic, *Chemical Communications*, 2015, **51**, 5848-5851.
75. R. A. Smaldone, R. S. Forgan, H. Furukawa, J. J. Gassensmith, A. M. Z. Slawin, O. M. Yaghi and J. F. Stoddart, *Angewandte Chemie International Edition*, 2010, **49**, 8630-8634.
76. G. Ferey and C. Serre, *Chemical Society Reviews*, 2009, **38**, 1380-1399.

77. Y. Liu, W. Xuan and Y. Cui, *Advanced Materials*, 2010, **22**, 4112-4135.
78. M. J. Ingleson, J. P. Barrio, J. Bacsa, C. Dickinson, H. Park and M. J. Rosseinsky, *Chemical Communications*, 2008, DOI: 10.1039/B718443C, 1287-1289.
79. D. N. Dybtsev, A. L. Nuzhdin, H. Chun, K. P. Bryliakov, E. P. Talsi, V. P. Fedin and K. Kim, *Angewandte Chemie International Edition*, 2006, **45**, 916-920.
80. A. L. Nuzhdin, D. N. Dybtsev, K. P. Bryliakov, E. P. Talsi and V. P. Fedin, *Journal of the American Chemical Society*, 2007, **129**, 12958-12959.
81. J. An, S. J. Geib and N. L. Rosi, *Journal of the American Chemical Society*, 2009, **131**, 8376-8377.
82. P. Horcajada, T. Chalati, C. Serre, B. Gillet, C. Sebrie, T. Baati, J. F. Eubank, D. Heurtaux, P. Clayette, C. Kreuz, J.-S. Chang, Y. K. Hwang, V. Marsaud, P.-N. Bories, L. Cynober, S. Gil, G. Ferey, P. Couvreur and R. Gref, *Nat Mater*, 2010, **9**, 172-178.
83. J. An, C. M. Shade, D. A. Chengelis-Czegan, S. Petoud and N. L. Rosi, *Journal of the American Chemical Society*, 2011, **133**, 1220-1223.

Chapter 2

Objectives

2. Objectives

The main objective in this PhD thesis is to exploit the coordination abilities of biomolecules, in particular amino acids and nucleobases, to construct new and versatile coordination polymers and metal-organic frameworks. The thesis has been organised around the following objectives:

1. Study the influence of enantiomeric ratio of two chiral ligands over the structure and chirality in Metal-Organic Frameworks:

    - Design, synthesis and complete characterization of the aspartic acid-based benzene-1,3,5-tricarboxamide linkers, (1***S***,3***S***,5***S***)-benzene tricarbonyl tri-(aspartic acid) and (1***R***,3***R***,5***R***)-benzene tricarbonyl tri-(aspartic acid), for the construction of novel and functional metal-organic frameworks. Here we aim to use the supramolecular and coordination abilities of benzene-1,3,5-tricarboxamide derivatives to build up MOFs from Cu(II) and aspartic acid-based benzene-1,3,5-tricarboxamide linkers.
    - Study the influence of the enantiomeric ratio of ***R***- and ***S***- linkers over the structure, chirality and properties of the resulting MOFs.
    - Fully characterization of the chiral and porosity properties of resulting frameworks.

2. Design and synthesis of novel nucleobase-adenine, aromatic tetracarboxylate ligands and transition metals.

    - Design, synthesis and characterization of coordination polymers constructed from Co(II) ions, aromatic tetracarboxylate ligand and adenine. Here we aim to take advantage of the wide range of binding modes of adenine for metal coordination and different forms of protonation as a bridging and terminal ligand.
    - Fully characterise the properties of the resulting coordination polymers. Here we aim to study the reversible hydrochromic behaviour of the adenine based coordination polymers synthesised.

Chapter 3

The influence of the enantiomeric ratio of an organic ligand on the structure and chirality of metal–organic frameworks

3. The influence of the enantiomeric ratio of an organic ligand on the structure and chirality of metal–organic frameworks.

3.1. Chirality

Chirality is used to describe an object that cannot be superimposed on its mirror image. The word "chiral" was derived from the Greek word for hand because our hands are good example of chirality since they are non-superimposable mirror images of each other. In nature, most of the molecules of life are chiral and, in living systems they are almost always enantiomerically pure. Natural *L*-amino acids (main components of proteins) and *D*-sugars (main components of DNA) are the perfect illustration of this particularity. Almost all 20 amino acids in naturally occurring proteins are chiral, and all of them are classified as being left handed, except glycine. On the contrary, the helical structure of naturally occurring DNA turns to the right.

Since Pasteur discovered the molecular chirality in the crystallization of the racemic sodium ammonium tartrate tetrahydrate from an aqueous solution, the interest in the production of optically active intermediates and products as pure enantiomers is a topic of ever-increasing importance for the chemical industry. For example, in the pharmaceutical sector, chirality is crucial since the differently handed forms (called 'enantiomers') of chiral molecules can have very different physiological effects. A harmless example is glucose: both enantiomers taste sweet, but the body can only metabolize the (natural) right-handed form. The left-handed form, which is manufactured artificially, is used as a calorie-free sweetener.

The chiral molecules can be mainly classified in three types of chirality. The ***point chirality*** is related to the presence of an asymmetric carbon in the molecule. An asymmetric carbon is one around which four different substituents can be arranged in left- or right-handed orientation (Figure 1, top). Also, a molecule can be chiral even if it lacks an asymmetric carbon. This is the case for molecules that possess an axis about which a set of substituents is held in a spatial arrangement that is not superimposable on its mirror image (Figure 1, middle).[1] This particular class of chirality is called ***axial chirality***. Finally, helicity or ***helical chirality*** is another special form of axial chirality. Helicity can be a type of molecular chirality if the substituents are atoms covalently attached to the axis. In this case, the molecule has axial chirality. However, if the substituents are molecules held together along the axis by noncovalent bonds, the assembly has helical chirality (Figure 1, bottom).[1] Interestingly, helicity is a special form of one-dimensional chirality, and can be found in single-, double-, and triple-helical structures. Helicity is widely observed in polymeric structures as a consequence of their homochirality.[2-5]

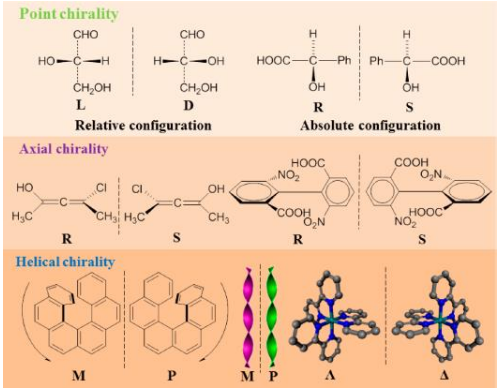

Figure 1 Chiral molecules and types of chirality: point, axial and helical chirality. Reproduced from reference 1.

3.2. Chirality in porous solids

In general, chiral solids from a mixture of enantiomers can crystallize as conglomerate, racemic or pseudo-racemic solids. A *conglomerate* is formed when the enantiomers crystallize separately, meaning that a mixture of enantiomerically pure crystals is obtained. This phenomenon is called *spontaneous resolution*. In contrast, racemic compounds are formed when the two enantiomers coexist in the same cell unit and then, the crystal contains both *R* and *S*-enantiomers.[6] Then, mixtures of enantiomers can crystallize in three ways: (i) as a *racemic compound* in which both enantiomers are present in the same condensate; (ii) as a *conglomerate* in which molecules form condensates comprised of only one enantiomer, but where the sample as a whole is racemic because it contains equal amounts of enantiomorphic condensates; and (iii) as a *pseudoracemate*, in which the condensates contain the two enantiomers in a non-ordered arrangement" (Figure 2).[7]

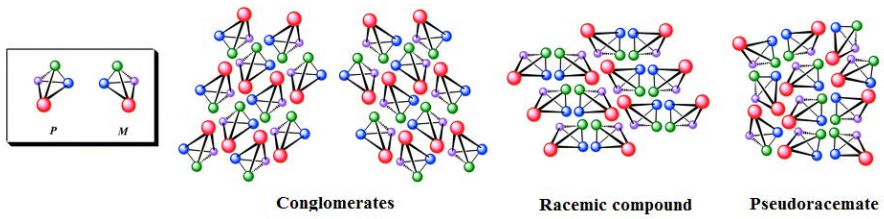

Figure 2 Representation of conglomerates, racemic compounds and pseudoracemate condensates. Adapted from reference 7.

Among the different methods to obtain enantiomerically pure compounds, the asymmetric catalysis is probably the most interesting and challenging method. In this type of catalysis, chiral catalysts can transfer its chiral information to thousands or even millions of new chiral molecules.[8-11] A very promising type of asymmetric catalysts is

today the family of chiral porous solids. Indeed, the incorporation of enantiomerically pure building blocks into porous materials offers many advantages (*e.g.* confined molecules in their chiral pores) for using them not only in asymmetric catalysis but also in other enantioselective processes such as separation.

Inorganic frameworks that include zeolites can show chiral structures in both right- and left handed crystalline forms crystallizing as racemic conglomerates. However, a few of these materials (*e.g.* zeolite β, titanosilicate ETS-10, SU-32 and ITQ-37) exist as homochiral porous solids. In particular, ITQ-37 combines potential chiral activity with extra-large pores.[12] However, although zeolites contain channels and cages of molecular dimensions and therefore they are ideally suited for molecular separation, the preparation of enantiopure zeolites is still very challenging. For this, due to the promising porosity and synthetic flexibility of MOFs, there is recently an increasing interest in controlling the synthesis of chiral MOFs. To date, there are basically three approaches that one can follow to synthesize chiral MOFs: considerations to take account of in the growth of chiral coordination compounds: i) use chiral molecules as ligands to build up MOFs; ii) the addition of a chiral specie that, even though it is not incorporated into the MOF, can induce chirality on it; and iii) the post synthetic modifications (PSM) of MOFs to introduce chiral moieties, thus transforming an achiral MOF into a homochiral MOF. Among these different strategies, the use of chiral molecules as building blocks is the most extended one. **Figure 3** shows some of the chiral molecules used in the synthesis of chiral porous MOFs so far. Note there that some of them are amino acids, as already mentioned in the introduction.

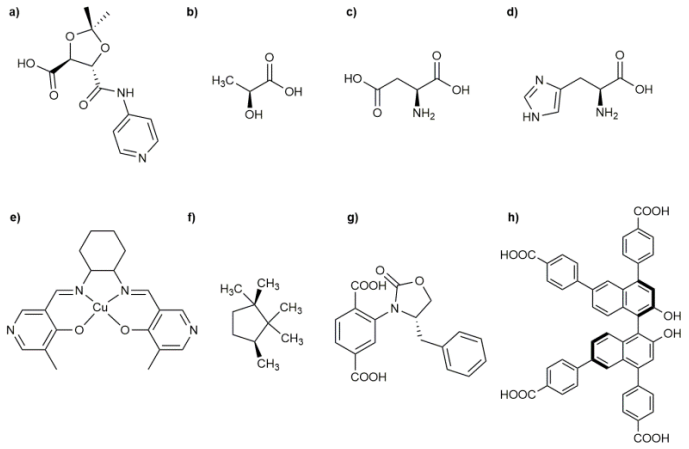

Figure 3 Representation of some chiral linkers used in the synthesis of homochiral MOFs.

3.3. Our research: The influence of the enantiomeric ratio of an organic ligand on the structure and chirality of metal–organic frameworks

Considering the importance of using chiral building blocks for the construction of porous MOFs, in the first part of this Thesis, we have performed a systematic study to determine how the enantiomeric ratio of a chiral ligand influences the final structure and properties of a synthesized MOF. This study, which is entitled "The influence of the enantiomeric ratio of an organic ligand on the structure and chirality of metal–organic frameworks", was published in *Chemical Communications*, 2014, 13829-13832. In it, we took advantage of the inherent chirality of amino acids to design and synthesize two enantiomorphs, which were then used as ligands to synthesize chiral MOFs. In these syntheses, the enantiomeric ratio was systematically

modified in order to determine how this affects the final structure, porosity and chirality properties of these MOFs.

3.3.1 Synthesis of 1,3,5-benzene tricarbonyl tri-(*S*-(*L*-) or *R*-(*D*-) aspartic acid; *S*- or *R*-BTAsp)

Initially, the two enantiomorphs (1*S*,3*S*,5*S*)-benzene tricarbonyl tri-(aspartic acid) (*S*-BTAsp) and (1*R*,3*R*,5*R*)-benzene tricarbonyl tri-(aspartic acid) (*R*-BTAsp) were designed and synthesized. These ligands were designed to combine the rigidity of the phenyl ring (blue) with the coordination ability, chirality and flexibility of the aspartate carboxylic groups (*S*, orange; *R*, green; **Figure 4**).

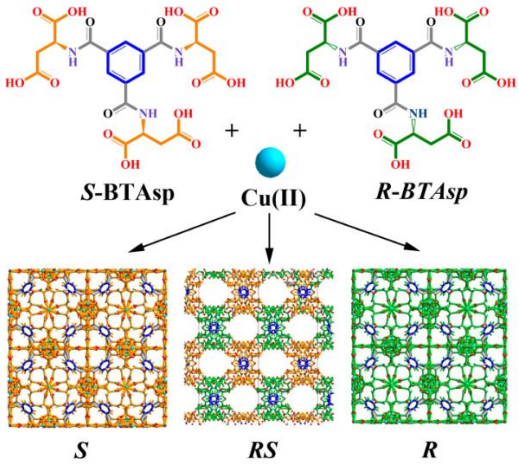

Figure 4 Schematic illustration of the enantiopure ligands R- and S-BTAsp. Under identical conditions, the reaction of Cu(II) with R-BTAsp alone, or mixtures of S- and R-BTAsp, or S-BTAsp alone affords the three distinct MOFs R, RS and S (bottom), respectively, which differ by chirality and/or porosity.

Figure 5 shows the synthetic route followed for preparing *S*- and *R*-BTAsp ligands. Both (1*S*,3*S*,5*S*)-1,3,5-benzenetricarbonyl tri-(*S*-(*L*-)aspartic dimethyl ester) and (1*R*,3*R*,5*R*)-1,3,5-benzenetricarbonyl tri-(*R*-(*D*-)aspartic dimethyl ester) were synthesised as previously

reported.[13] Briefly, dry triethylamine (4.24 mL, 30.13 mmol) was added to a cool solution (0 ºC) of *S*-(*L*-) or *R*-(*D*-) aspartic acid dimethyl ester hydrochloride (2.71 g, 13.29 mmol) in dry CH_2Cl_2 (40 mL). The resulting mixture was stirred for 20 min at 0 ºC. Then, a solution of 1,3,5-benzenetricarbonyl trichloride (1.0 g, 3.69 mmol) in dry CH_2Cl_2 (30 mL) was added dropwise, and the reaction was stirred overnight. The reaction mixture was treated with CH_2Cl_2 (50 mL) and washed with aq. 2N H_2SO_4, followed by aq. $NaHCO_3$ and water. The organic layer was dried with anhydrous Na_2SO_4 and concentrated *in vacuo* to give 2.04 g of (1*S*,3*S*,5*S*)-1,3,5-benzenetricarbonyl tri-(*S*-(*L*-)aspartic dimethyl ester) (yield: 86%) or 2.01 g of (1*R*,3*R*,5*R*)-1,3,5-benzenetricarbonyl tri-(*R*-(*D*-)aspartic dimethyl ester) (yield: 85%). Both molecules were characterized by FT-IR [ATR, cm^{-1}: $\tilde{\nu}$ =3369.4, 3238.3, 2931.6, 2628.8, 2526.6, 1703, 1635.5, 1544.9, 1413.7, 1300, 1186, 921.9, 628.8, 574.7] and ^{1}H-NMR [DMSO-d_6, 250 MHz, ppm: 2.83-3.12 (m, 6H), 3.68 (s, 9H), 3.71 (s, 9H), 4.88-4.97 (m, 3H), 8.51(s, 3H), 9.32 (d, J=7.58 Hz, 3H)] (**Figure 6**).

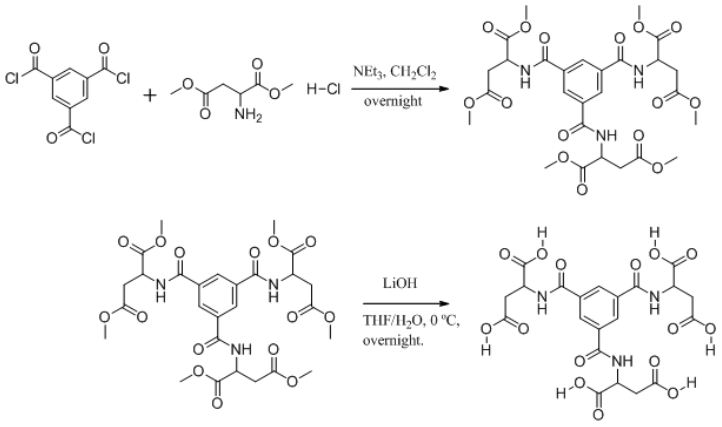

Figure 5 Synthetic route of (1*S*,3*S*,5*S*)-1,3,5-benzenetricarbonyl tri-(*S*-(*L*-)aspartic dimethyl ester) (and (1*R*,3*R*,5*R*)-1,3,5-benzenetricarbonyl tri-(*R*-(*D*-)aspartic dimethyl ester).

In a final step, both esters were saponificated by adding $LiOH{\cdot}H_2O$ (22.42 mmol) to a solution of (1*S*,3*S*,5*S*)-1,3,5-benzenetricarbonyl tri-(*S*-(*L*-)aspartic dimethyl ester) or (1*R*,3*R*,5*R*)-1,3,5-benzenetricarbonyl tri-(*R*-(*D*-)aspartic dimethyl ester) (3.20 mmol) in THF (20 mL) and H_2O (5 mL) at ~0 ^oC. The reaction mixture was stirred overnight at room temperature, and then acidified to pH ~3 with HCl (1.0 M). The resulting mixture was washed with brine, dried over Na_2SO_4 and concentrated *in vacuo* to give 1.55 g (yield: 87%) of ***S*-BTAsp** or 1.56 g of ***R*-BTAsp** (yield: 87%). Both ligands were characterized by FT-IR (ATR, cm^{-1}: 50 MHz, ppm): 2.68-2.90 (m, 6H), 4.69-4.77 (m, 3H), 8.54(s, 3H), 9.14-9.16 (d, J=7.48 Hz, 3H). FT-IR [ATR, cm^{-1}: $\tilde{\nu}$ = 3352, 1633.6, 1541, 1402.2, 1280.7, 1188] and ^{1}H-NMR [DMSO-d_6, 250 MHz, ppm: 2.68-2.90 (m, 6H), 4.69-4.77 (m, 3H), 8.54(s, 3H), 9.14-9.16 (d, J=7.48 Hz, 3H)] (**Figure 6**).

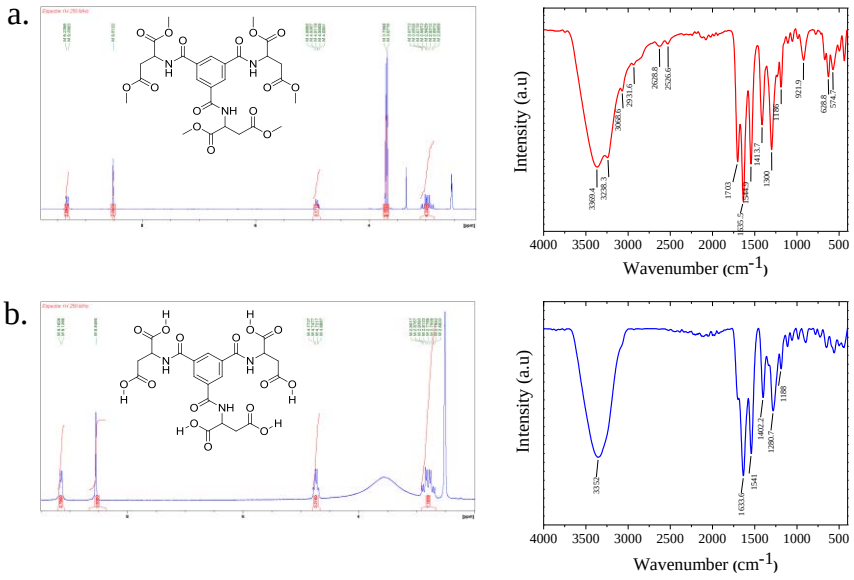

Figure 6 ^{1}H NMR spectra (solvent: DMSO-d6) and corresponding FT-IR spectra of **a)** *S*-BTAsp-OMe and **b)** *S*-BTAsp.

To evaluate of the enantiopurity of the synthesised BTAsp ligands, we prepare aqueous solutions of *R*- and *S*-BTAsp and of an equimolar mixture of the both ligands. Electronic Circular Dichroism (ECD) Spectroscopy analysis were performed for the aqueous solutions. We observed that pure ligands presented opposite chirality and the racemic solution presented no activity (**Figure 7**).

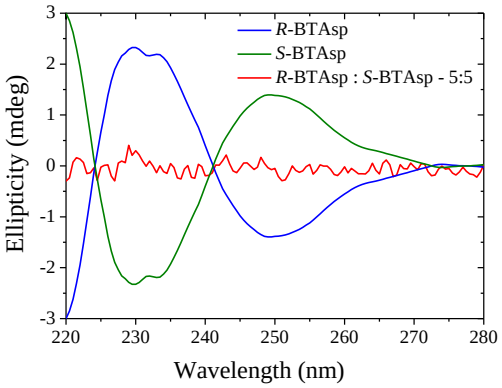

Figure 7 ECD spectra of aqueous solutions of free enantiopure *R*- and *S*-BTAsp and of an equimolar mixture of the both ligands.

3.3.2 Synthesis and crystal structures of MOFs made of S- and/or R-BTAsp

Once *S*- and *R*-BTAsp were synthesized, both ligands were reacted with Cu(II) ions with either enantiomerically pure ligand (*S*- or *R*-BTAsp) or with the racemic mixture *RS*-BTAsp under identical reaction conditions. These reactions yielded three 3D polyamino acid-based MOFs (**Figure 8**): two isostructural and homochiral, non-porous (but with large void volumes) MOFs with opposite optical activity (hereafter, ***S*** and ***R***) (**Figure 8a**); and a third, achiral, MOF (hereafter, ***RS***), which contains 1D pores accessible for gas uptake (**Figure 8b**).

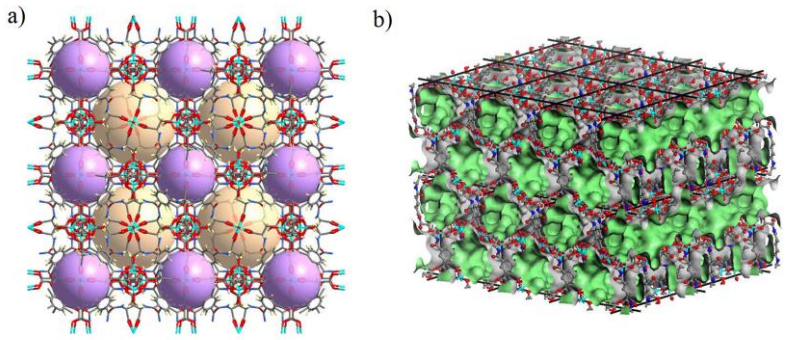

Figure 8 a) Packing of ***S*** along the *c*-axis, showing the organisation of the large cages (yellow balls) and cavities (purple balls) forming the channel system. **b)** Crystal structure of ***RS***, Connolly surface representation of ***RS*** viewed in 3D.

3.3.2.1 Synthesis, crystal structure and optical properties of [Cu_3(*S*- or *R*-BTAsp)(H_2O)$_3$].12.75H_2O (*S* or *R*)

To synthesize ***S*** or ***R***, $Cu(NO_3)_2{\cdot}2.5H_2O$ (100 mg, 0.43 mmol) was added to an aqueous solution (4 mL) of enantiopure *S*-BTAsp or *R*-BTAsp (10 mg, 0.02 mmol). The mixture was brought to pH 6 using NaOH (1M) and became slightly cloudy. After 24 h at room temperature, greenish-blue octahedral crystals of ***S*** or ***R*** were obtained (**Figure 9**), and then filtered and air-dried to give 12.6 mg of ***S*** (yield: 67%, based on *S*-BTAsp) or 12.4 mg of ***R*** (yield: 70%, based on *R*-BTAsp). Elemental analysis was used to confirm their purity; for ***S*** - $[Cu_3(C_{21}H_{15}N_3O_{15})(H_2O)_3].(H_2O)_{12.75}$, calculated (%): C: 24.7, H: 4.6, N: 4.1; found: C: 26.3, H: 4.2, N: 4.1; and for ***R*** - $[Cu_3(C_{21}H_{15}N_3O_{15})(H_2O)_3].(H_2O)_{12.75}$, calculated (%): C: 24.7, H: 4.6, N: 4.1; found: C: 26.0, H: 4.0, N: 4.5.)

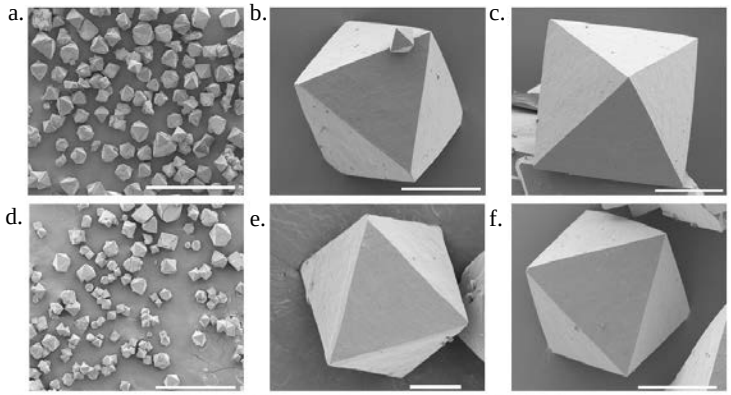

Figure 9 SEM images of **a-c)** ***R***, **d-f)** ***S***. The images reveal the octahedral morphology of the ***R*** and ***S*** crystals, and the intergrown, needle-shaped crystals of *RS*, and confirm that all the MOFs are homogeneous. Scale bars: **a)** 400 μm; **b)** 30 μm; **c)** 20 μm; **d)** 400 μm; **e)** 10 μm; **f)** 30 μm.

Single-crystal XRD revealed the formation of identical 3D networks of formula $[Cu_3(S\text{-BTAsp})(H_2O)_3]\cdot 12.75H_2O$, ***S***, and $[Cu_3(S\text{-BTAsp})(H_2O)_3]\cdot 12.75H_2O$, ***R***. Both MOFs crystallise in the chiral *F23* space group (**Table 1**). The basic unit of the MOF is a Cu_2 paddlewheel unit, in which each Cu(II) is coordinated to four carboxylate O atoms, from four adjacent aspartate functions, and to one H_2O molecule. Each carboxylate group of the aspartate residue bridges two Cu(II) centres within the Cu_2 paddlewheel unit; consequently, a single *S*-BTAsp (or *R*-BTAsp) ligand binds to twelve Cu(II) centres (**Figure 10**).

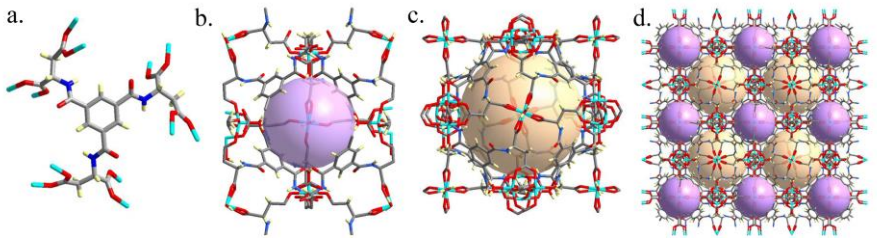

Figure 10 a-d) Crystal structure of ***S***. **a)** Binding mode of the ligand *S*-BTAsp. **b)** Single cavity forming the 3D channel system, in which the purple ball illustrates the internal diameter (7.0 Å). **c)** Single large cage delimited by 8 *S*-BTAsp ligands and 18 Cu(II) paddlewheels. The yellow ball represents the internal void volume (1340 Å^3) within the cage. **d)** Packing of ***S*** along the *c*-axis, showing the organisation of the large cages (yellow balls) and cavities (purple balls) forming the channel system. *b*-axis. Atom colour code: Cu: sky blue; C: grey; O: red; N: blue; and H: yellow.

Within both structures, the aspartate residues of a single BTAsp ligand have the same conformation, as confirmed by measurement of the side chain dihedral angle: -66.65° for *S*-BTAsp 65.11 ° *R*-BTAsp for (**Figures 11** and **12**). The specific folding of the aspartate groups of the ligand, and the coordination around the Cu(II)-paddlewheel unit, of together create a 3D structure that incorporates two types of void volumes: i) a 3D channel system, formed of cavities (internal diameter: 7.0 Å, considering van der Waals radii (vdW); **Figure 13**) connected by small pores (dimensions: 7.0 Å x 3.5 Å, considering vdW radii) and ii) larger, isolated cages, in which the shortest separation between their centroid and their vdW surface is 6.8 Å, indicating that a sphere with a volume of 1340 Å^3 can fit inside them (**Figures 13** and **14**).

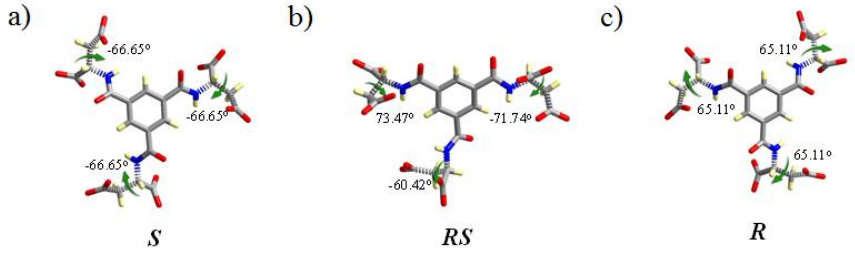

Figure 11 Representation of BTAsp within **a)** ***S***, **b)** ***RS*** and **c)** ***R***. The dihedral side-chain angles of a single BTAsp ligand within ***S*** and ***R***, are equivalent (-66.65º and 65.11º, respectively), which confirms their opposite configuration and that the ligand is symmetric (*i.e.* the aspartate groups fold in the same manner). In contrast, the dihedral side-chain angles of the BTAsp ligand within ***RS*** are not equivalent: each aspartate residue folds in a different way, which highlights the flexibility of the ligand.

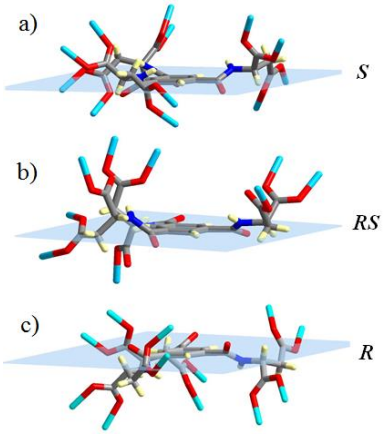

Figure 12 Illustration of the BTAsp ligand within **a)** ***S***, **b)** ***RS*** and **c)** ***R***. The blue represents the plane (through the benzene ring) and confirms that the ligand is equivalent within ***S*** and ***R*** and symmetric, but within ***RS*** it is not so.

Remarkably, these large cages are not accessible, as the largest window aperture is found to be between HOH···OCNH and CH···HCH, at a distance of 3.4 Å and 0.5 Å, respectively, including vdW radii of the atoms (**Figure 15**). The 3D channel system and the large cages combine for a total void space of 52% per unit cell (**Figure 13b,c**).[14] In addition,

PXRD patterns confirmed that both ***S*** and ***R*** are isostructural (**Figure 16**).

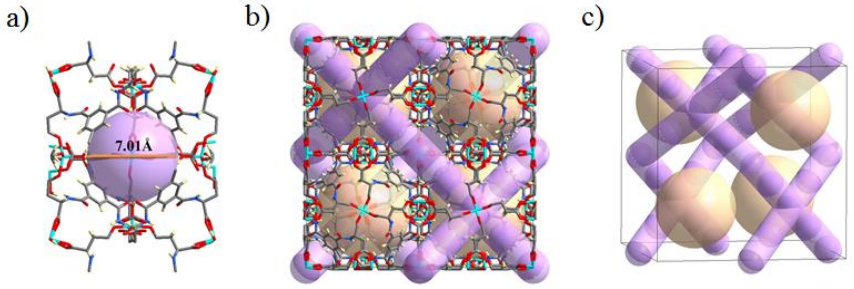

Figure 13 a) Representation of the cavities formed in ***S*** (diameter: 7.01 Å). **b-c)** 3D view of one unit cell, showing the organisation of the large isolated cages (yellow) and the cavities (purple); the latter are interconnected in 3D by pore openings (dimensions: 7.0 Å x 3.5 Å).

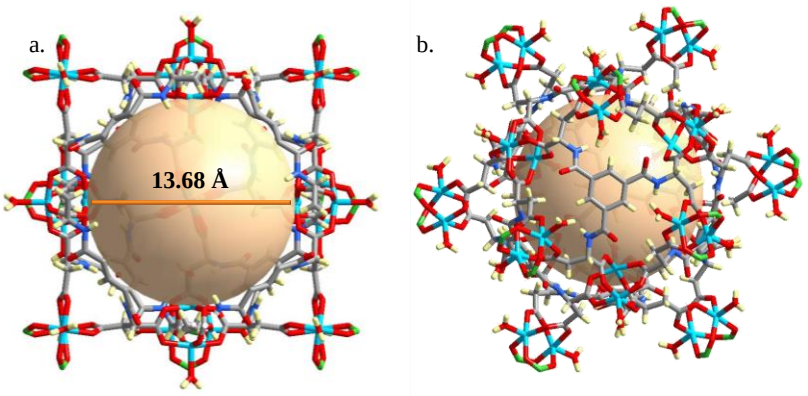

Figure 14 a) Representation of one large isolated cage in ***S***. **b)** Representation showing that each cage comprises eight BTAsp ligands and eighteen Cu-paddlewheels, twelve of which are shared with twelve neighbouring cages. The C atoms of the shared paddlewheels are coloured in green.

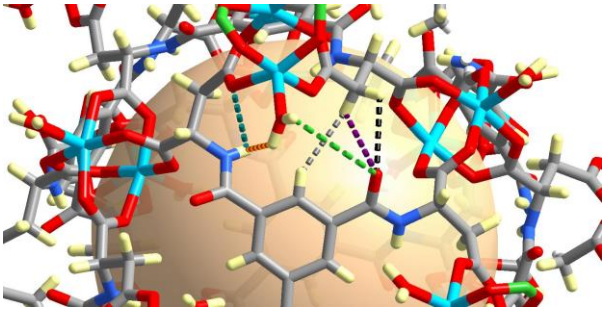

Atom-to-atom distance	Colour	Bond distances (Å) (including van der Waals radii)
NH···OC	blue	1.4
NH···HOH	orange	2.0
HOH···OC	green	3.4
CH···HCH	grey	0.5
HCH···OC	purple	0.3
HCH···OC	black	0.2

Figure 15 Representation of the bond distances within the isolated cages in ***S***, confirming the absence of any significant opening.

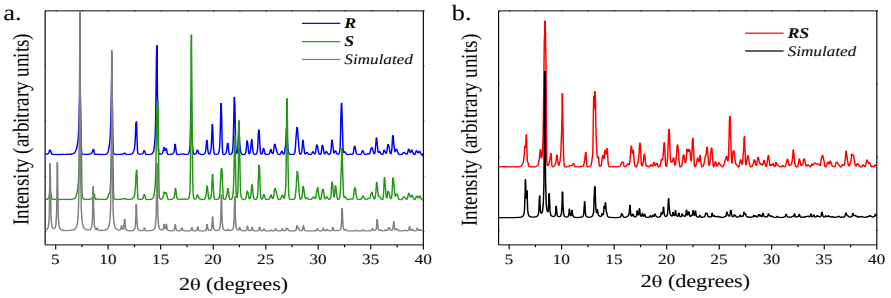

Figure 16 Comparison of the experimental PXRD patterns of **a)** ***R*** and ***S***, and of **b)** ***RS***, with their corresponding simulated PXRD pattern derived from the single-crystal XRD data. The excellent match indicates that all three MOFs were isolated as pure phases.

Table 1 Crystallographic data for ***S***, ***RS*** and ***R***.

Crystal data	***S***	***RS***	***R***
Empirical formula	$C_{21}H_{15}Cu_3N_3O_{30.75}$	$C_{42}H_{30}Cu_6N_6O_{53}$	$C_{21}H_{15}Cu_3N_3O_{30.75}$
Formula weight	991.99	1848.02	991.99
Temperature / K	293(2)	150	150
Crystal system	cubic	orthorhombic	cubic
Space group	F23	Pcnn	F23
a / Å	34.172(5)	17.530(3)	34.182(3)
b / Å	34.172(5)	20.037(3)	34.182(3)
c / Å	34.172(5)	21.050(3)	34.182(3)
α / °	90	90	90
β / °	90	90	90
γ / °	90	90	90
Volume / $Å^3$	39904(18)	7394(2)	39939(11)
Z	32	8	32
ρ_{calc} / mg mm^{-3}	1.321	1.660	1.320
μ / mm^{-1}	1.351	1.808	1.351
F(000)	4520.0	3374.0	4520.0
Crystal size / mm^3	0.61 × 0.32 × 0.32	0.56 × 0.34 × 0.22	0.38 × 0.2 × 0.2
Crystal colour and shape	Green-blue octahedra	Green-blue needles	Green-blue octahedra
θ range for data collection	4.128 to 52.734°	4.95 to 52.74°	4.128 to 52.734°
Index ranges	-42 ≤ h ≤ 42, -42 ≤ k ≤ 42, -42 ≤ l ≤ 42	-17 ≤ h ≤ 21, -24 ≤ k ≤ 23, -26 ≤ l ≤ 24	-42 ≤ h ≤ 18, -42 ≤ k ≤ 36, -39 ≤ l ≤ 37
Reflections collected	140953	19582	30141
Independent reflections	6832	7428	6736
R(int) =	0.0711	0.0241	0.0485
Data/restraints/parameters	6832/0/360	7428/0/473	6736/0/360
Goodness-of-fit on F^2	1.323	1.048	1.196
Final R indices [I > 2σ (I)]	R_1 = 0.0828, wR_2 = 0.2770	R_1 = 0.0659, wR_2 = 0.2013	R_1 = 0.0836, wR_2 = 0.2670
Final R indices [all data]	R_1 = 0.0920, wR_2 = 0.2926	R_1 = 0.0716, wR_2 = 0.2084	R_1 = 0.0897, wR_2 = 0.2775
Largest diff. pk/hole (e $Å^{-3}$)	2.27/-0.72	1.68/-0.80	1.98/-0.73
Flack parameter	0.022(7)		0.073(8)

3.3.2.2 Synthesis and crystal structure of [Cu_3(*RS*-BTAsp)$(H_2O)_4$]·7.5H_2O, *RS*.

To explore the influence of the enantiopurity of *R*- and *S*-BTAsp ligands on MOF synthesis, we prepared a racemic mixture using equimolar amounts (er = 5:5) of the two ligands, and then reacted it with Cu(II) using the same experimental conditions as for the isolation of ***S*** and ***R***. In this synthesis, $Cu(NO_3)_2$·2.5H_2O (100 mg, 0.43 mmol) was added into an aqueous solution (4 mL) of an equimolar mixture of *S*-BTAsp (5 mg, 0.01 mmol) and *R*-BTAsp (5 mg, 0.01 mmol) at pH 3.8. The mixture was brought to pH 6 using NaOH (1M), which immediately became slightly cloudy. After 15 to 17 days at room temperature, 5.8 mg of *RS* (yield: 35%, based on *S*-BTAsp) was obtained as greenish-blue, intergrown needle-type crystals (**Figure 17**). Elemental analysis for *RS* - [$Cu_3(C_{21}H_{15}N_3O_{15})(H_2O)_4$].$(H_2O)_{7.5}$, calculated (%): C: 26.6, H: 4.0, N: 4.4; found: C: 27.4, H: 4.6, N: 3.8.

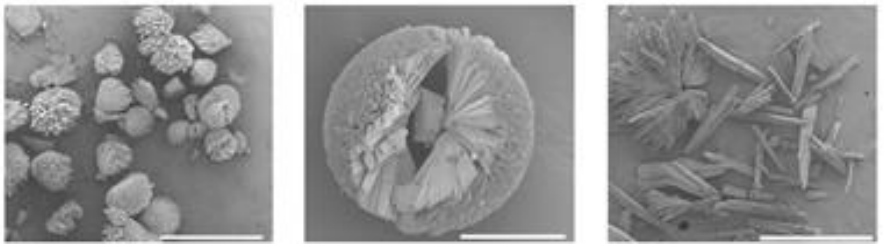

Figure 17 SEM images of ***RS***. The images reveal the octahedral morphology of the ***R*** and ***S*** crystals, and the intergrown, needle-shaped crystals of ***RS***, and confirm that all the MOFs are homogeneous. Scale bars: 1 mm (left); 50 μm (middle) ; and 500 μm (right)

Single-crystal XRD revealed the formation of a new 3D MOF of formula [Cu_3(*RS*-BTAsp)$(H_2O)_4$]·7.5H_2O, ***RS***, which crystallises in the centrosymmetric *Pcnm* orthorhombic space group (**Table 1**). Within ***RS***, there are three distinct Cu(II) ions: Cu#1, which has square pyramidal

geometry; and Cu#2 and Cu#3, both of which have square planar geometry. Each aspartate group of the BTAsp within ***RS*** is bound to three Cu(II) ions, giving a total connectivity per ligand of nine Cu(II) ions (**Figure 18a**). A striking difference observed between ***S*** or ***R*** and ***RS*** is that the side-chain dihedral angles of the three aspartate groups within a single BTAsp ligand in ***RS*** vary (73.47°, -60.42° and -71.74°) (**Figure 11b**). In ***RS***, the coordination of the BTAsp ligand around the three distinct Cu(II) leads to the formation of columnar left- and right-handed helices (**Figure 18b**), in which the benzene rings of the BTAsp are stacked along the *b*-axis, introducing weak π-π stacking interactions (distance: 4.0 Å). This organisation generates 1D channels (dimensions: 9.1 Å x 4.3 Å, considering vdW radii) running along the *b*-axis (**Figures 18d** and **19**). These channels are filled with four H_2O molecules coordinated to Cu#3 and 7.5 guest H_2O molecules. The total accessible void volume of ***RS*** is 32% per unit cell,[14] and the calculated pore volume in ***RS*** is 0.181 cm^3/g.

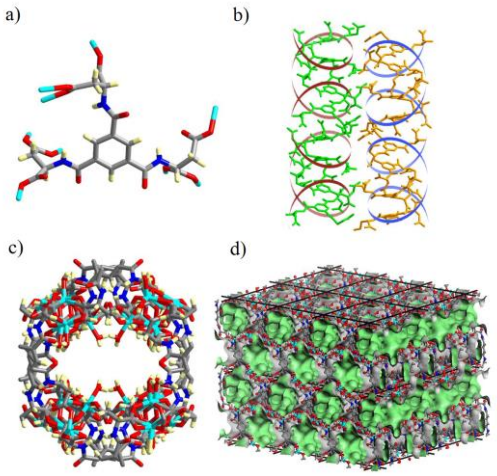

Figure 18 a) Coordination of BTAsp ligand to nine Cu(II) centres. **b)** Left- or right-handed helices made by connecting the Cu(II) ions to either *S*-BTAsp or *R*-BTAsp, respectively, along the *b*-axis. **c)** Stick representation of one pore channel (dimensions:

of 9.1 Å x 4.3 Å), and **d)** Connolly surface representation of ***RS*** viewed in 3D. Atom colour code: Cu: sky blue; C: grey; O: red; N: blue; and H: yellow.

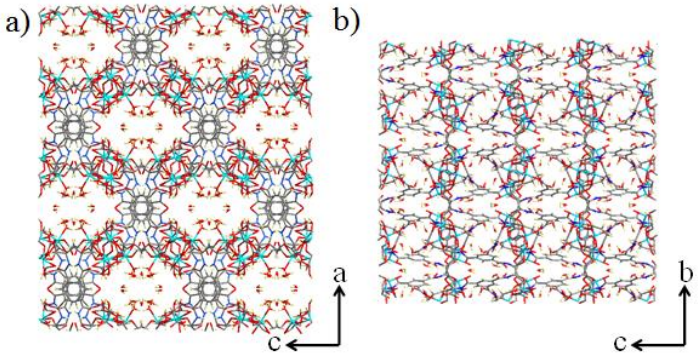

Figure 19 Packing of ***RS*** along the b-axis and the a-axis, showing that the 1D pores are filled with H_2O molecules and revealing the columnar arrangement of the BTAsp ligand (along the *b*-axis), respectively.

3.3.2.3 Study of the influence of the enantiopurity of the BTAsp ligands

Initially, the opposite chirality between ***S*** and ***R*** was confirmed by solid-state Vibrational Circular Dichroism (VCD). The use of this technique was possible because the chirality of both MOFs is defined by the coordination network between the Cu(II) ions and the carboxylate groups, which have specific absorptions in the infrared region. In these VCD spectra, a mirror-image relationship was clearly observed between the enantiomeric pairs of ***S*** and ***R*** (**Figure 20a**). The most relevant inverted VCD signals were at 1623 cm^{-1} and 1417 cm^{-1}, which primarily correspond to asymmetric and symmetric stretching bands, respectively, of the carboxylate groups; and at 1537 cm^{-1}, which is attributed to the bending of N-H bond. Both frameworks were also studied using ECD by disassembling them under acidic conditions (pH 2.0; **Figures 20b**). For ***S*** and ***R***, identical ECD signals of their

corresponding enantiomeric *S*- or *R*-BTAsp ligands, respectively, were observed (**Figure 21**). As expected, note here that no VCD and ECD signals were detected for the ***RS***, thereby confirming that is composed of a racemic mixture of *S*- and *R*-BTAsp ligands (**Figure 20a-b**).

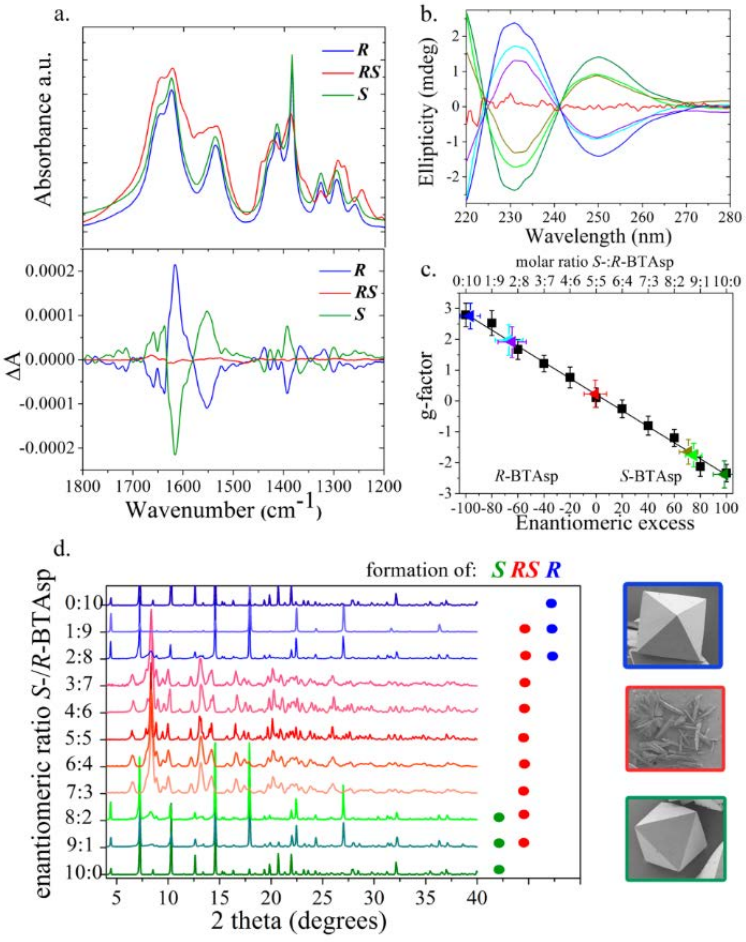

Figure 20 a) IR (top) and VCD (bottom) spectra of ***S***, ***R*** and ***RS***. **b)** ECD spectra collected after the disassembly of the MOF crystals synthesised using er of 10:0, 9:1 and 8:2 (and *vice versa*) of *S*-BTAsp/*R*-BTAsp and er 5:5. **c)** Plot of g-values against enantiomeric excess of *S*-BTAsp/*R*-BTAsp. The triangles represent the g-values calculated from the MOFs synthesised using er of 0:10 (blue), 1:9 (sky blue), 2:8 (purple), 5:5 (red), 8:2 (dark yellow), 9:1 (light green) and 10:0 (green). d) PXRD patterns and FESEM images of the MOFs resulting when various ratios of *S*-BTASp/*R*-BTAsp were used in the reaction with Cu(II).

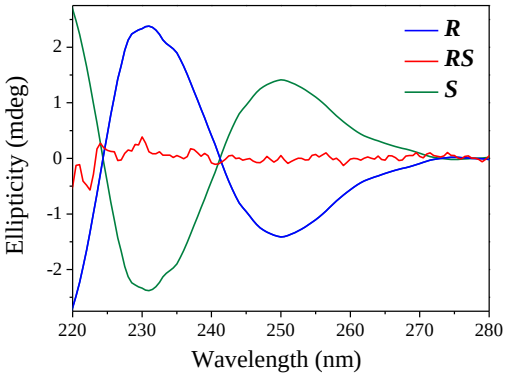

Figure 21 ECD spectra of the BTAsp ligand present within ***R***, ***S*** and ***RS*** after disassembly of each MOF at pH 2. The profiles are consistent with the corresponding ECD profiles of free R-BTAsp, free S-BTAsp and the equimolar mixture of the two ligands.

To evaluate the importance of the enantiopurity of the BTAsp ligand in the resulting MOF, we systematically prepared different mixtures of *S*- and *R*-BTAsp (from 9:1 to 1:9, including the enantiopure 10:0 and 0:10), and then reacted each mixture with Cu(II) under the conditions used for the isolation of ***S***, ***R*** and ***RS***.

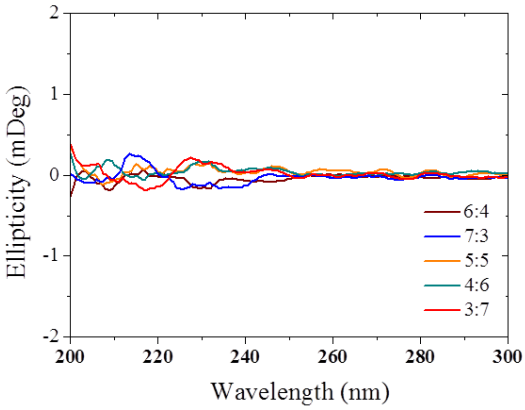

Figure 22 ECD spectra of the BTAsp ligand present in the ***RS*** crystals obtained when using ***R***-BTAsp /***S***-BTAsp ratios of 7:3 or 6:4 (and vice versa), after their disassembly at pH 2. These profiles are consistent with the ECD profile of the equimolar mixture of ***R***- and ***S***-BTAsp and therefore, with the formation of ***RS*** (see **Figure 7**).

We observed that the use of a slight excess of either *S*- or *R*-BTAsp (7:3 and 6:4, or *vice versa*) always led to the formation of the achiral ***RS*** phase, just as when synthesised with the equimolar mixture (5:5). For all reactions, the formation and purity of ***RS*** was confirmed by Field Emission SEM (FESEM), PXRD and ECD after disassembly of the product at pH 2 (at which point we could not detect any signal by ECD; **Figure 22**). Contrariwise, when a large excess of either *S*- or *R*-BTAsp (9:1 and 8:2, or *vice versa*) was used, we observed mainly the formation of octahedral crystals indicative of the homochiral ***S*** or ***R***, respectively, as confirmed by both PXRD (**Figure 20d**) and ECD (**Figure 20b**). However, the presence of low-intensity Bragg reflections (2θ: 8.3° and 13.2°), together with the different ECD intensity maxima,[15] revealed that a small amount of ***RS*** also had formed together with ***S*** or ***R***.

To quantify the amounts of ***S***, ***R*** and ***RS*** formed in the aforementioned reactions, we disassembled the product crystals at pH 2, and then determined the corresponding enantiomeric excess (ee) of the free *S*- or *R*-BTAsp. We used an analytical method based on calculation of the anisotropy factor: the g-factor, a concentration-independent parameter derived from the absorbance and ellipticity of the chiral ligand.[16, 17] In a first step, this method was validated by confirming the linearity of the g-factor calculated in pure samples of *S*- or *R*-BTAsp in the working concentration range (0.04 mg/mL to 0.06 mg/mL; **Figure 23**). The analytical calibration curve (R^2 = 0.994) was measured by calculating the g-factor of different mixtures of *S*- and *R*-BTAsp (from 9:1 to 1:9, including the enantiopure 10:0 and 0:10), and then plotting them against the enantiomeric excess (ee). As shown in **Figure 20c**, the straight line nearly intercepts the “x” axis at 0% ee—the

value expected for the racemic mixture. To test this method, a series of control experiments was performed, in which the ee of pure samples of ***S***, ***R*** and ***RS*** was measured. The g-values of the enantiopure ***S*** and ***R***, and of the racemic ***RS***, were -2.4 ± 0.4, 2.8 ± 0.4 and 0.2 ± 0.4, respectively, corresponding to the expected 99.3 ± 8.7 ee (*S*-BTAsp), 97.5 ± 7.9 ee (*R*-BTAsp) and 0.7 ± 8.8 ee (*R*-BTAsp), respectively. Finally, the g-values of the MOF crystals resulting from the reactions run with a large excess of either isomer (9:1 and 8:2, and *vice versa*) were measured. These values were found to be: -1.7 ± 0.4 [9:1; 71.4 ± 7.2 ee (*S*-BTAsp)], -1.8 ± 0.4 [8:2; 75.5 ± 6.4 ee (*S*-BTAsp)], 1.9 ± 0.5 [2:8; 65.2 ± 11.0 ee (*R*-BTAsp)] and 2.0 ± 0.5 [1:9; 67.6 ± 10.8 ee (*R*-BTAsp)]. Importantly, these ee values, together with the previously described PXRD data, demonstrate that both ligands indeed participate in the construction of the MOFs in these reactions. Here, if one assumes that a combination of ***S*** and ***RS*** is simultaneously formed when 9:1 and 8:2 ratios are used (or ***R*** and ***RS*** for the 1:9 and 2:8 ratios), then the percentage of ***S*** relative to ***RS*** (or ***R*** relative to ***RS*** for the 1:9 and 2:8 ratios) is simply given by the corresponding ee value (~ 65-75%).

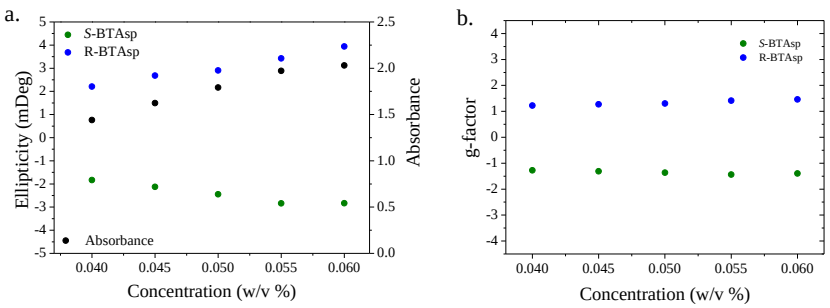

Figure 23 a) Absorbance and ellipticity of enantiopure R-BTAsp or S-BTAsp ligand as a function of concentration. **b)** The derived g-factor values plotted against the concentration of the pure ligand (R-BTAsp or S-BTAsp). Note that the g-factor values remain constant over the working concentration.

3.3.2.4 Porosity properties

Thermogravimetric analysis (TGA) of isostructural ***S*** and ***R*** indicated a continuous weight loss of 25.1% and 26.3%, respectively, from 30 °C to 200 °C, which we attributed to the loss of all H_2O molecules (calcd. 27.7%; **Figure 24**). Above 200 °C, both frameworks decompose in multiple steps. The TGA profile of *RS* shows a weight loss of 11.2% from 30 °C to 200 °C, which we ascribed to the removal of the 7.5 guest H_2O molecules (calcd. 14.6%; **Figure 24**). Also, ***RS*** begins to decompose stepwise at 200 °C. To further evaluate the thermal stability of ***S*** and ***RS***, TGA data were complemented with *in-situ* Variable Temperature PXRD (VT-PXRD) experiments performed in a closed capillary tube. VT-PXRD revealed that ***S*** (and therefore, ***R***) slowly collapses and becomes an amorphous solid above 100 °C (**Figure 25**). This finding is consistent with the TGA data and with the PXRD pattern of the activated *S* after lyophilisation at -50 °C and 0.07 mbar (**Figure 26**), showing that the collapse of *S* (and therefore, of *R*) occurs gradually, upon the loss of H_2O molecules. Contrariwise, the VT-PXRD patterns of ***RS*** show that it loses much of its crystallinity at a far higher temperature (200 °C) than does ***S***.

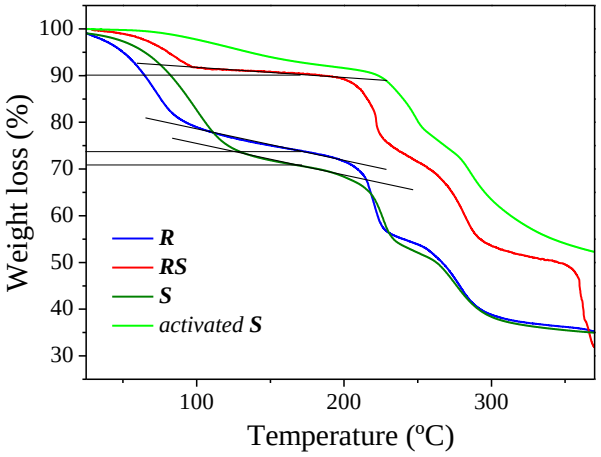

Figure 24 TGA curves for ***R, S, RS*** and activated ***S*** (heating rate: 5 °C/min; temperature range: 25 to 400 °C), showing that the profiles of ***R*** and ***S*** are very similar (continuous loss up to 200 °C, corresponding to the loss of the guest H_2O molecules). Above this temperature, the framework collapses stepwise. In contrast, ***RS*** shows a weight loss of 9.8% from 30 °C to 100 °C, which corresponds to the loss of guest H_2O molecules; is stable up to 200 °C; and then decomposes stepwise above 200 °C. The TGA curve of the activated ***S*** shows no loss from 30 °C to 100 °C, which confirms that ***S*** is free of any guest molecules; this is followed by a weight loss of 7.1% that occurs before decomposition.

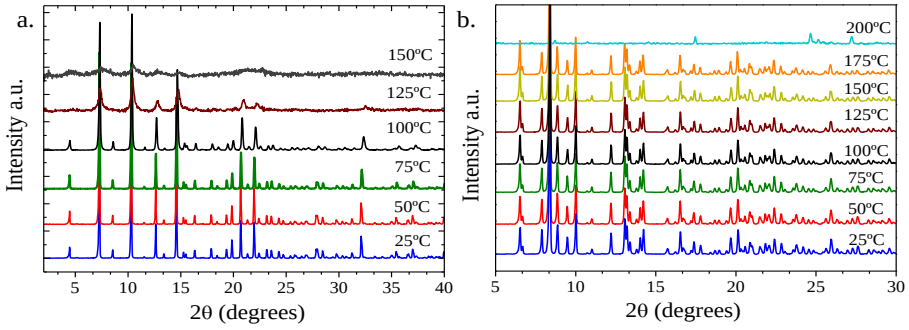

Figure 25 a) *In-situ* variable temperature PXRD patterns of ***S*** sealed in a capillary tube, from 25 °C to 150 °C. As observed, ***S*** maintains its structural integrity up to 100 °C. Above this temperature, ***S*** gradually collapses, which is consistent with the TGA data. **b)** *In-situ* variable temperature PXRD patterns of ***RS*** sealed in a capillary tube, showing that it is thermally stable up to 175 °C (*i.e.* at a much higher temperature than is ***S***). The loss of crystallinity observed from 175 °C to 200 °C reveals that ***RS*** collapses rapidly, presumably

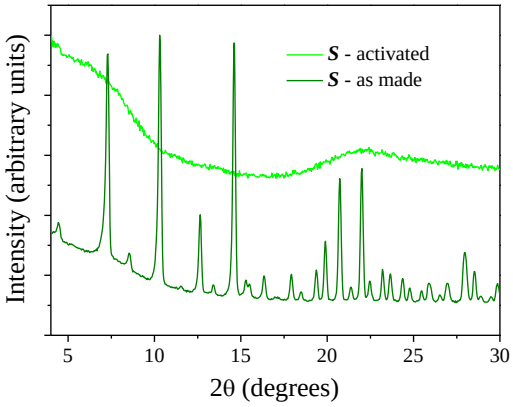

Figure 26 PXRD spectra revealing that upon activation-lyophilisation, **S** becomes irreversibly amorphous.

As expected, type II isotherms (77 K and 1 bar) of ***S*** and of ***R*** revealed that they are non-porous to N_2. This is due to their low stability upon removal of the guest H_2O molecules, as confirmed by TGA and PXRD (Figure 53). In contrast, ***RS*** (once activated by solvent exchange with chloroform for 72 hours (Figure S19) and subsequent outgassing at 40 ºC overnight)[18] is porous to N_2 (92.7 cm^3/g at 0.96 bar; BET surface area: 263 m^2/g at $0.05>p/p^0>0.3$) at 77 K, for which it showed a reversible typical type-I isotherm (**Figure 27a**). The pore volume for ***RS***, derived from the N_2 adsorption branch using the Dubinin-Radushkevich equation,[19] was found to be 0.142 cm^3/g, which is somewhat smaller than the value (0.181 cm^3/g) estimated from the static crystal structure. The type-I N_2 isotherm of ***RS*** prompted us to investigate its CO_2 sorption and to assess the strength of the interactions between ***RS*** and CO_2. ***RS*** is porous to CO_2 (79.8 cm^3/g at 195 K and 0.85 bar) at 195 K, showing a type-I isotherm (**Figure 27b**). At 273 K and 0.85 bar, ***RS*** adsorbed 38.3 cm^3/g of CO_2, whereas at 295 K and 0.85 pressure, it adsorbed 25.5 cm^3/g of CO_2. Isosteric heats of adsorption (Q_{st}) of ***RS*** for CO_2 were

calculated from the virial-type expression,[20] using the adsorption branches of the isotherms measured at 273 K and 295 K (**Figure 28**). At zero coverage, Q_{st} was calculated to be 27.5 kJ/mol, but it gradually decreased to 18.5 kJ/mol at high loadings.

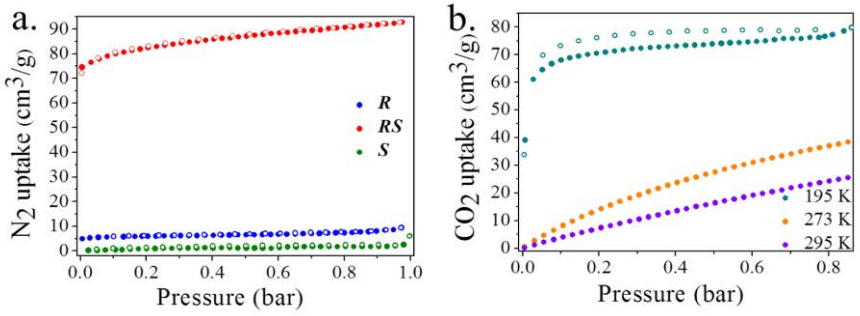

Figure 27 a) N_2 isotherms on ***S***, ***R*** and ***RS*** collected at 77 K up to 1 bar and **b)** CO_2 isotherms collected on ***RS*** at 195, 273 and 295 K up to 0.85 bar

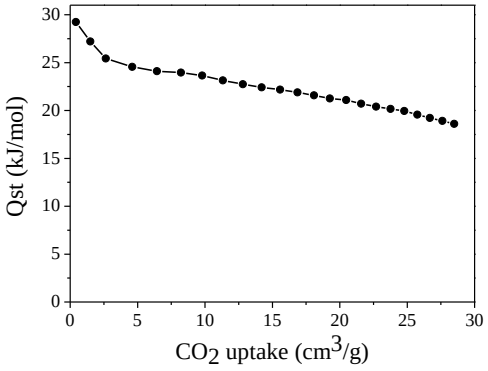

Figure 28 Isosteric heat of adsorption (Q_{st}) calculated using the Clausius-Clapeyron equation and the adsorption branches of the CO2 isotherms (collected at 273 K and 295 K).

3.4 Conclusions

In conclusion, we have demonstrated that the ratio of two opposite enantiomeric ligands can influence the final structure of the resulting MOFs. We showed that by simply modifying the ratio of *S*-BTAsp/*R*-BTAsp in a MOF reaction, the structure of the resulting MOF can be tuned between the three structures ***R***, ***RS*** and ***S***, which exhibit different porosity and chirality properties. The systematic identification of new parameters that determine MOF structures is important, as it will enable greater understanding of structure/-function relationships and therefore, enable better engineering of MOFs for targeted applications.

3.5 References

1. M. Liu, L. Zhang and T. Wang, *Chemical Reviews*, 2015, **115**, 7304-7397.
2. J. Zhang and X. Bu, *Chemical Communications*, 2009, DOI: 10.1039/b816742g, 206-208.
3. J. Zhang, S. Chen, A. Zingiryan and X. Bu, *Journal of the American Chemical Society*, 2008, **130**, 17246-17247.
4. X. Wu, H.-B. Zhang, Z.-X. Xu and J. Zhang, *Chemical Communications*, 2015, **51**, 16331-16333.
5. Y. Liu, H. Zhang, C. Tian, P. Lin and S. Du, *CrystEngComm*, 2013, **15**, 5201-5204.
6. J. Jacques, A. Collet and S. H. Wilen, *Enantiomers, racemates, and resolutions*, Krieger Pub. Co., 1994.
7. L. Perez-Garcia and D. B. Amabilino, *Chemical Society Reviews*, 2002, **31**, 342-356.
8. J. Crassous, *Chemical Communications*, 2012, **48**, 9687-9695.
9. M. Xue, B. Li, S. Qiu and B. Chen, *Materials Today*, DOI: http://dx.doi.org/10.1016/j.mattod.2016.03.003.
10. M. Yoon, R. Srirambalaji and K. Kim, *Chemical Reviews*, 2011, **112**, 1196-1231.

11. Y. Liu, W. Xuan and Y. Cui, *Advanced Materials*, 2010, **22**, 4112-4135.
12. R. E. Morris and X. Bu, *Nat Chem*, 2010, **2**, 353-361.
13. V. Haridas, Y. K. Sharma and S. Naik, *European Journal of Organic Chemistry*, 2009, **2009**, 1570-1577.
14. A. L. Spek, *J. Appl. Crystallogr.*, 2003, **36**, 7-13.
15. A. E. Holmes, S. Zahn and J. W. Canary, *Chirality*, 2002, **14**, 471-477.
16. P. Horváth, A. Gergely and B. Noszál, *Talanta*, 1997, **44**, 1479-1485.
17. M. T. Reetz, K. M. Kühling, H. Hinrichs and A. Deege, *Chirality*, 2000, **12**, 479-482.
18. J. An, O. K. Farha, J. T. Hupp, E. Pohl, J. I. Yeh and N. L. Rosi, *Nat Commun*, 2012, **3**, 604.
19. F. R. Rouquerol, J.; Sing, K. S. W. , *Adsorption by Powders and Porous Solids: Principles, Methodology and Applications*, Academic Press, 1998.
20. S. A. Al-Muhtaseb and J. A. Ritter, *Industrial & Engineering Chemistry Research*, 1998, **37**, 684-696.

Chapter 4

Adenine-based coordination polymers: synthesis, crystal structure, coordination modes and reversible hydrochromic behavior

4. Nucleobase coordination polymers

The use of nucleobases as building blocks for the construction of CPs is very promising because of their structural rigidity and versatility, different metal-binding sites, and multiple possible coordination modes.[1] These features are enhanced by their intrinsic self-assembly properties that open a door to new and functional architectures.[2] In this section, we will introduce the possibilities that offer nucleobases, and specially adenine, to construct CPs.[3]

4.1. Nucleobases

Natural nucleobases that include adenine, cytosine, guanine, thymine and uracil are very important in nature because they are involved in the self-assembly of the DNA and RNA double helices (Figure 1). These double helices, which result from the interaction between two DNA strands, are primarily mediated by four nucleobases [adenine (A), cytosine (C), guanine (G), and thymine (T)] forming A–T and C–G base pairs.[4]

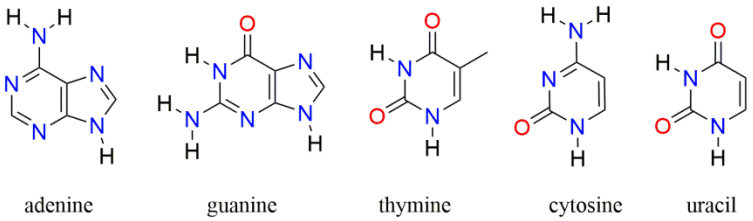

Figure 1 Five main natural nucleobases: **a)** adenine, **b)** guanine, **c)** thymine, **d)** cytosine and **e)** uracil showing oxygen and nitrogen donor sites.

Besides the crucial role of nucleobases in nature, they can also form coordination bonds with more than one metal ion and thus, act as organic linkers to construct CPs. Indeed, nucleobases can coordinate to metal ions

through the nitrogen and keto oxygen atoms of their base heterocyclic ring (**Figure 1**). In addition, they can simultaneously participate in other supramolecular interactions, including hydrogen-bonds and π-π stacking, and they have the capacity to recognize its complementary pyrimidine nucleobase and form stable A-T, G-C base pairing (**Figure 2**).

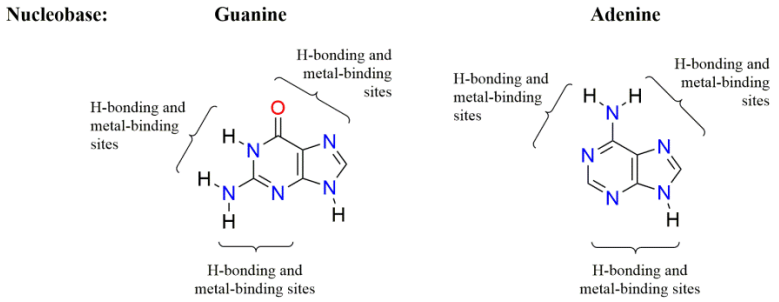

Figure 2 Purines nucleobases. Guanine and adenine schemes are showing available sites for non-covalent interactions as H-bonding and metal binding.

4.2. Adenine as potential ligand for coordination polymers

Figure 3 Chemical structure of adenine showing the labels for the Nitrogen binding sites. The exocyclic amino group and N9 may coordinate via deprotonation.

Among the different nucleobases, the purine derivative adenine has been mostly used for the generation of new CPs.[2, 3, 5] Adenine contains an exocyclic amino group and four imino nitrogens, allowing a versatile metal ion coordination *via* the imino nitrogen N1, N3, N7 and N9 atoms, or through the N6 atom of the amino group after its deprotonation

(**Figure 3**). Thus, adenine presents five potential coordination sites with a decrease in basicity that follow this order: N9>N1>N7>N3>N6. Importantly, these coordination sites can be protonated in acidic media and deprotonated in basic media affecting and enriching their coordination capacity (Figure 6).

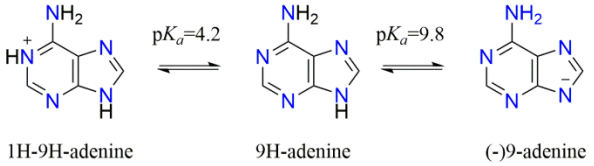

Figure 4 Chemical structure of 9H-adenine along with deprotonated (-9)H-adenine and protonated 1H-9H-adenine in aqueous solution.

Besides these numerous potential coordination sites, the imidazole moieties [N7, N9] in adenine possess the ability to imitate the coordination of imidazole used to construct the well-known zeolitic imidazolate frameworks (ZIFs). Also, the [N3, N9] coordination pattern resemble to a carboxylic acid group by replacing the two coordinating oxygen atoms with two coordinating imino nitrogens, making possible the formation of adeninate-paddlewheel structures.[6] In addition, since adenine has usually a neutral character, it can also be mixed with other auxiliary linking molecules (mainly, polycarboxylate linkers) to synthesize MOFs with larger accessible pores. Altogether make adenine very attractive for designing new CPs.

An analysis of extended structures containing adenine and transition metal ions obtained from the Cambridge Structural Database (CSD; Allen, 2002) illustrates the rich coordination modes that can adopt adenine for constructing CPs (**Figure 5**). From this study, we found that adenine can act as a simple monodentate ligand, mainly through the N3 or N9 sites.[7-9] Adenine can also act as a bidentate ligand through a wide variety of

combinations depending on the N sites that participate in the metal binding [N3, N9];[10, 11] [N7, N9];[11-14] [N1, N9];[15] [N1, N7];[11] and [N3, N7] sites. Adenine can also coordinate via more than two N sites. In fact, the most common coordination mode found in CPs is [N3, N7, N9],[7, 16-24] or by the more unusual coordination modes for adenine [N1, N6, N9][24] and [N3, N6, N9].[25] Finally, adenine can also coordinate four metal ions via the N1, N3, N7 and N9 sites.[26, 27]

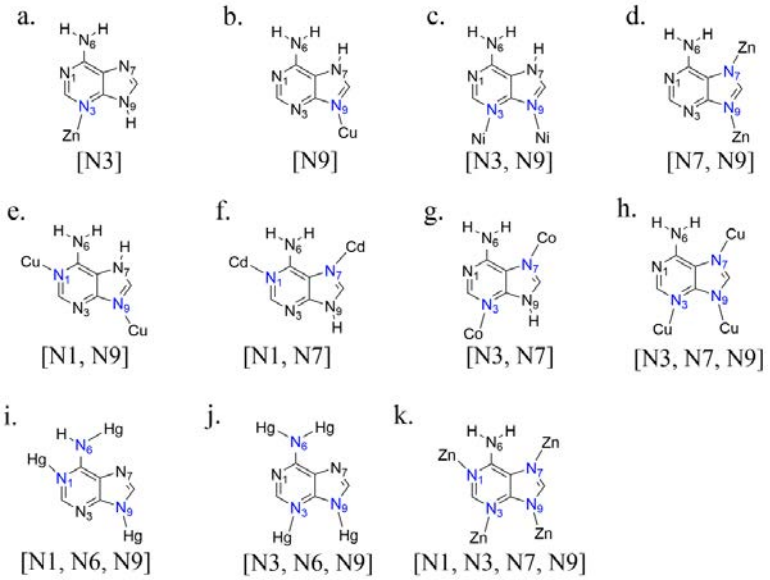

Figure 5 Representation of the coordination modes of adenine observed in extended structures.

The bridging μ_2-bidentate modes of the deprotonated (-9)H-adenine found in CPs include μ_2-N3, N9 or μ_2-N7, N9 modes. An example of μ_2-N3, N9 bridging mode was reported by Stylianou *et al.*[10] These authors reported that hydrothermal reactions of $NiCO_3$, 3,5-pyrazole dicarboxylic acid (H_3pzdc) and adenine (9H-ade) in pure water for 72 hours at 140°C yields $[Ni_3(pzdc)_2(7H\text{-}ade)_2\ (H_2O)_4]\cdot(H_2O)_{2.18}$. Within the structure, 1D chains formed by Ni/7H-ade/pzdc are linked into a 3-D non-covalent

network constructed through hydrogen bonding and π-π stacking interactions between the 7H-ade ligands (**Figure 6a-d**). The chains are based on $[Ni_2(7H\text{-}ade)_2]^{4+}$ dimeric units, where adenine coordinates through imidazolate N9 and pyrimidinate N3 atoms to the two nickel cations (Figure 11a). These dimeric units are linked by the pzdc anions to form the 1D chains, which are then linked via one strong and one weak hydrogen bond from the 7H-ade amino group to two pzdc carboxylate oxygens, and via π–π interactions between the 7H-ade pyrimidinate rings.

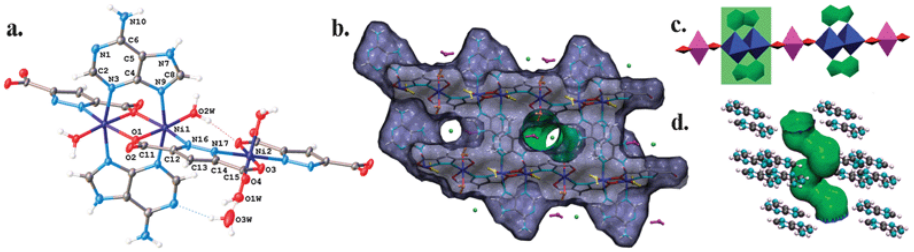

Figure 6 a) Structural motif with numbering scheme. b) Molecular surfaces and channel space calculated for the fully desolvated structure, c) Schematic of the chain unit: Ni1 (blue)/7H-ade (green) blade motif linked by pzdc (red) to Ni2 (magenta). d) Adenine units showing the proximity of N1 and N7H to the fully desolvated channel space (green) (Reproduced from reference 10).

Deprotonated (-9)H-adenine can also coordinate to soft metal ions such as Cu(II), Zn(II), Cd(II) or Hg (II) via the [μ_3-N3, N7, N9] bridging tridentate mode. Zhang, *et al*.[6] reported the synthesis of a CP with formula $Zn_3[Zn_2(\mu_2\text{-}H_2O)]_3(ade)_6(TATB)(DMF)$ (TATB = 4,4′,4′′-s-triazine 2,4,6-triyl-tribenzoate). This CP was synthesized via a solvothermal reaction between zinc acetate, adenine and H_4TATB in N,N′-dimethylformamide (DMF) and water. Two basic coordination units form this structure. The

first unit consists of a four-coordinate Zn(II) ion that links two adeninates via the N7 atom on the imidazolate moiety and two carboxylates (Figure 13a), and the second consists of a $Zn_2(\mu_2\text{-}H_2O)$ unit, where two adeninates bridge the dizinc center via N3 and N9 atoms at the two equatorial positions, while two carboxylates coordinate to the dizinc center at the two axial positions (**Figure 7a**). Each adeninate coordinates via N3, N7 and N9 with three Zn(II) ions. All the imino N7 donors coordinate to first unit, and all the N3 and N9 atoms coordinate to second unit leaving N1 and the exocyclic N6 atoms uncoordinated. Both units are connected by adeninate in a 1:1 ratio, forming one-dimensional zinc-adeninate chains. The solvent accessible volume of PCN-530 is 47.80% calculated by using the PLATON routine, indicating its porous nature. Indeed, PCN-530 possesses open channels of 7.4 × 11.9 Å along the *a* axis (**Figure 7b**)

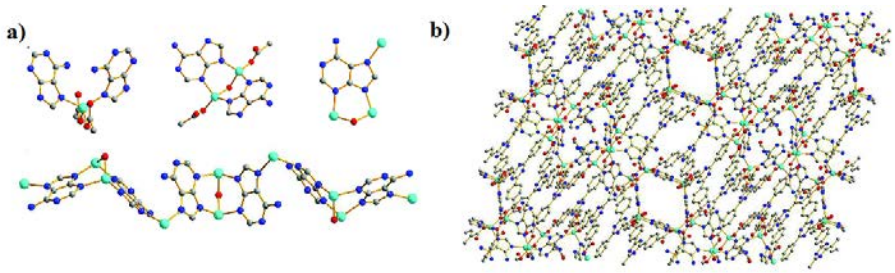

Figure 7 a) Coordination mode of adenine and one-dimensional zinc-adeninate chain and **b)** 3D packing of PCN-530 (Reproduced from reference 6).

García-Terán, *et al.,*[7] reported the synthesis of the crystal structure, thermal behavior, and magnetic properties of a covalent 3D network containing adenine as a bridging ligand, the porous coordination polymer $[Cu_2(\mu\text{-ade})_4(H_2O)_2][Cu(oxalate)(H_2O)]_2 \cdot 14H_2O$. The three-dimensional framework is composed for two distinct types of neutral building blocks: a dimeric $[Cu_2(\mu\text{-ade})_4(H_2O)_2]$ units and mononuclear

$[Cu(oxalate)(H_2O)]_2$ entities. Adeninate anions behave as tridentate bridging ligand with N3, N7, and N9 motif. The amino group of adenine remains uncoordinated and is hydrogen bonded to oxygen atoms of an oxalate ligand. The dimeric fragment, $[Cu_2(\mu\text{-ade})_4(H_2O)_2]$, is centrosymmetric and is made of two Cu(II) atoms bridged by four adeninate anions in dicopper paddlewheel cluster arrangement (**Figure 8a**). The self-assembly process directed by the metal-adeninate linkages create open channels along the crystallographic *c* axis with a diameter of about 13 Å (**Figure 8b**).

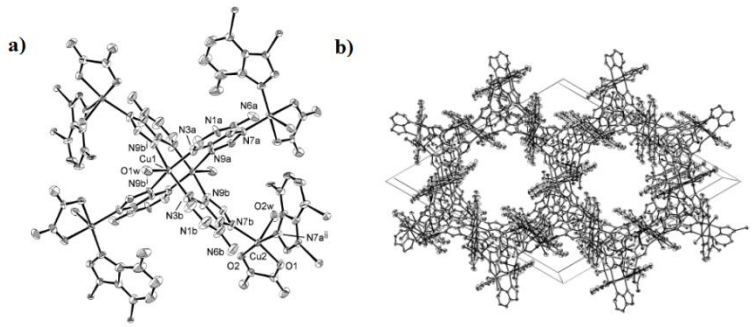

Figure 8 a) View of the $[Cu_2(\mu\text{-ade})_4(H_2O)_2]$ cluster and **b)** Perspective view of the 3D framework along the c axis, composed for the tetracopper(II)-adeninate framework $[Cu_2(\mu\text{-ade})_4(H_2O)_2][Cu(oxalate)(H_2O)]_2{\cdot}14H_2O$ (Reproduced from reference 7).

T□□□□□□□□□□□□□□□□–) anion can act as a bridge among □□□□□□□□□□□□□□□□□□□□□□ □□□□□□□□□□ μ_4-N1,N3,N7,N9 tetradentate mode. The μ_4-N1,N3,N7,N9 tetradentate mode was published by An *et al.* in a series of porous CPs called bio-MOFs. Bio-MOF-1, synthesized by reaction between biphenyldicarboxylic acid, (H_2bpdc), adenine and zinc in dimethylformamide (DMF) yielded a single crystalline material formulated as $[Zn_8(ade)_4(bpdc)_6O{\cdot}2(NH_2(CH_3)_2)^+]{\cdot}8DMF{\cdot}11H_2O$ (**Figure 9**). In Bio-MOF-1, adenine coordinates using [N1, N3, N7, N9] binding pattern. The

structure is based on zinc-adeninate columns (**Figure 9a**); the columns are formed by cages consisting on four adeninates and eight tetrahedral Zn ions, four at the corners of the equatorial plane of each cage and four at each apical position. The Zn^{2+} comprising the apexes constitute half of a ZnO cluster that links adjacent octahedral cages together. Pairs of tetrahedral Zn_4^{2+} within each ZnO cluster are bridged by two adeninates through the N3 and N9 positions. N1 and N7 of each adeninate coordinate to the tetrahedral Zn_4^{2+} in the equatorial plane. The zinc-adeninate columns are interconnected via BPDC linkers (**Figure 9b**). One carboxylate from each linker coordinates in a monodentate fashion to a Zn^{2+} in the ZnO cluster, while the other carboxylate binds in a monodentate fashion to one of the equatorial Zn_4^{2+} on an adjacent column[28]. Bio-MOF exhibited permanent porosity, and nitrogen adsorption studies yielded a type-I isotherm characteristic of a microporous material with a BET surface area is ~1700 m^2g^{-1}. The framework contains dimethylammonium cations inside the pores which give a cationic nature. These cations can be exchanged with cationic drugs for drug delivery applications.[28]

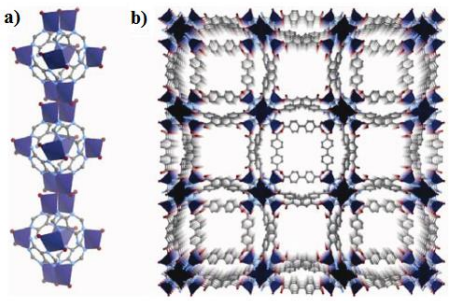

Figure 9 Crystal structure of bio-MOF-1 consists of **a)** zinc-adeninate columns, and **b)** 3-D framework by biphenyldicarboxylate linkers to generate a material with 1-D channels along the *c* crystallographic direction (Reproduced from reference 28).

Following the same methodology, An *et al.*[27] reported the synthesis of the anionic bio-MOF-100 (**Figure 16**). The structure of bio-MOF-100 contains the same discrete building units as in bio-MOF-1, described above. Hydrothermal reactions of adenine, biphenyldicarboxylic acid (H_2BPDC) and zinc acetate dihydrate in N,N′-dimethylformamide (DMF) and methanol in a capped glass vial for 24 h, leaded to a CP with formulae $[Zn_8(ade)_4(BPDC)_6O_2{\cdot}4(Me_2NH_2)^+]{\cdot}49DMF{\cdot}31H_2O$. In bio-MOF-100, 1-D zinc-adeninate columns act separately as discrete zinc-adeninate vertices. Bio-MOF-100 exhibits a very high surface area (4,300 $m^2 g^{-1}$), one of the lowest crystal densities (0.302 g cm^{-3}) and one of the largest metal-organic framework pore volume reported (4.3 $cm^3 g^{-1}$).

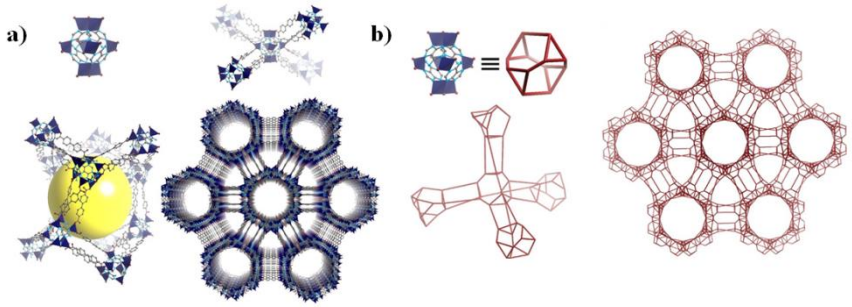

Figure 10 a) Crystal structure of bio-MOF-100. The ZABu is connected to four neighbouring zinc-adeninate building units via 12 BPDC linkers to generate a three dimensional structure with large cavities and large channels, **b)** underlying network topology of bio-MOF-100. Each subunit can be treated as a distorted truncated tetrahedron. Each truncated tetrahedron connects to four neighbouring tetrahedra to generate an augmented LCs net (Reproduced from reference 27).

4.3. Hydrochromic behavior in coordination polymers

In this section, the chromic phenomenon in CPs will be introduced. Chromism is a well-studied process that is used mainly for the development of chemical sensors. In general, chromic behaviour in a solid porous material is due to the solvent molecules entering on the cavities, which induce a certain shift on the optical absorption band of the host material. This phenomenon is called solvatochromism.[29] Solvatochromism can be *positive* (bathocromic or red shift) or *negative* (hypsochromic or blue shift).[30]

There are two main mechanisms for which CPs can show solvatochromism. The first one is due to the effect of the solvent polarity over a solvatochromic organic ligand (chromophore) forming the structure. It is known that, when absorption spectra of species containing a chromophore are measured in solvents of different polarity, the absorption bands are usually modified by these solvents.[30] These changes are the result of physical intermolecular solute–solvent interaction forces, which tend to alter the energy difference between the ground and excited states. A chromophore is generally regarded as any part of an organic molecule which is responsible for the light absorption.[30]

As an example of the solvatochromic effects of the guest molecules on chromophore ligands, Lu *et al.* synthesized a Cu(II)-based MOF $\{[(WS_4Cu_4)I_2(dptz)_3]\cdot DMF\}_n$ containing the chromophore ligand 3,6-di(pyridin-4-yl)-1,2,4,5-tetrazine (dptz).[31] Because of this ligand, this MOF showed a pronounced solvatochromic behavior when it was immersed in solvents with different polarities from water to chloroform (**Figure 11**).

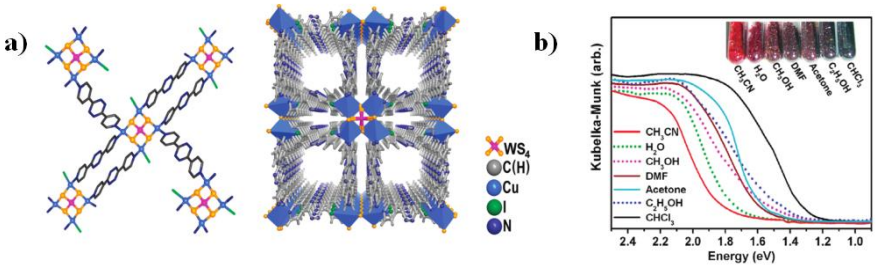

Figure 11 a) Coordination environment of the $WS_4Cu_4^{2+}$ unit (left) and crystal structure of $\{[(WS_4Cu_4)I_2(dptz)_3]\cdot DMF\}_n$ (right). **b)** UV-vis spectra and photograph of the inclusion compounds (Reproduced from reference 31).

Solvatochromism in CPs can also be due to changes in the first coordination sphere of the metal ions, including alterations in both coordination number and coordination geometry. In these materials, sorption-desorption processes of solvents usually induce structural changes and promote the generation of unsaturated metal sites.[32, 33] These modifications on the coordination environment of the metal ions provoke significant changes in the physical properties. [34] This behavior is quite common in CPs made of vanadium, cobalt, nickel, copper and metalloporphyrins, which can show intense color changes depending on their coordination environment.[35]

Among this latter type of CPs, a common case is when solvatochromism is due to the loss of coordinated water molecules changing the coordination environment of metal ions. Here, Su *et al*. reported the synthesis of a three-dimensional CP with formula $[Co_3(L)_2(BTeC)(H_2O)_2]\cdot 2H_2O$ (where HL is 3,5-di(imidazol-1-yl)benzoic acid and H_4BTeC is 1,2,4,5-benzenetetracarboxylic acid). In this CP, one of the Co(II) centers adopts a distorted octahedral geometry that includes a terminal water molecule in its coordination environment (**Figure 12**).[33] These authors observed that, after exposing this CP at 160 °C for 2

hours, the terminal water molecule was removed, so that the coordination geometry of Co(II) changed from octahedral to square pyramidal and its color from red to dark violet. Remarkably, this process was fully reversible when the dehydrated CP was exposed to air or water vapors. In this process, the dehydrated $[Co_3(L)_2(BTeC)]$ phase showed selective adsorption of water molecules over N_2, methanol and ethanol.

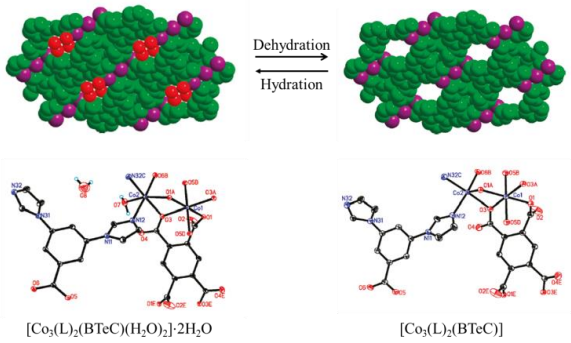

Figure 12 Reversible transformations of $[Co_3(L)_2(BTeC)]$ upon hydration/dehydration (Reproduced from reference 33).

Chen *et al.* published a related example in 2005.[36] A mix-metal CP with formula $[Co_2(ppca)_2(H_2O)(V_4O_{12})_{0.5}]\cdot 3.62H_2O$ (where ppca is 4-(pyridin-4-yl)pyridine-2-carboxylic acid) exhibited a reversible transformation involving a change in the Co(II) coordination environment when it was heated at 300 °C for 2 hours. This heating process induced the removal of all non-coordinated and coordinated water molecules and therefore, the Co2 environment changed from an octahedral to a trigonal bipyramidal coordination geometry (**Figure 13**). This modification led to a change in the crystal colour from red to brown. In this process, a reversible shrinkage and expansion was observed passing from 15% to 5.8% void space, and *vice versa*.

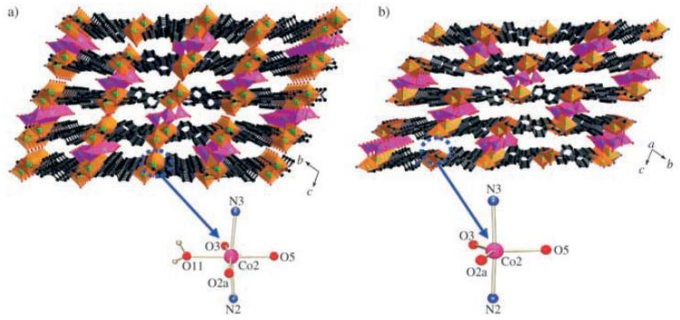

Figure 13 a) View of the [{$Co_2(ppca)_2(H_2O)(V_4O_{12})_{0.5}$}$_n$] framework containing hydrated Co2 in an octahedral coordination environment; **b)** view of the dehydrated [{$Co_2(ppca)_2(V_4O_{12})_{0.5}$}$_n$] framework containing Co2 in a trigonal-bipyramidal coordination environment (Reproduced from reference 36).

Also, Sarma *et al*. reported the influence of the dehydration into the coordination environment of Co(II) and Ni(II) ions in two CPs with formula $[M_2(5\text{-aip})_2(pyz)(H_2O)_2]\cdot 3H_2O$ (where M is Co(II) or Ni(II), 5-aip is 5-amino-isophthalic acid, and pyz is pyrazine).[32] In these cases, after dehydratation, $[Co_2(5\text{-aip})_2(pyz)(H_2O)_2]\cdot 3H_2O$ changed from purple to blue, whereas $[Ni_2(5\text{-aip})_2(pyz)(H_2O)_2]\cdot 3H_2O$ changed from green to dark yellow (**Figure 14**).

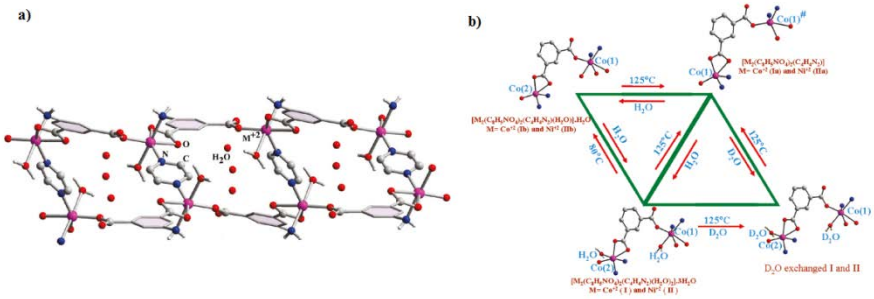

Figure 14 a) Metal atom (Co or Ni) completes its octahedral coordination with a terminal water molecule, and b)dehydration-rehydration studies of $[Co_2(5\text{-aip})_2(pyz)(H_2O)_2]\cdot 3H_2O$ and $[Ni_2(5\text{-aip})_2(pyz)(H_2O)_2]\cdot 3H_2O$ (Reproduced from reference 32).

A Mn(II)-based CP with a similar hydrochromic behaviour was reported by Näther *et al.*[37] These authors reported that, when a freshly prepared sample of this CP with formula $[Mn_2(H_2O)_2(\mu_2\text{-sqt})(\mu_2\text{-bipy})]\cdot 3H_2O$ (where H_2-sqt is squaric acid and bipy is 4,4'-bipyridine) was evacuated for several hours, its colour changed from colourless to yellow. In this CP, the water loss induced a change in the coordination environment of Mn(II) ions from octahedral to square planar (**Figure 15**). This process was reversible as the dehydrated CP recovered its original colour when it was exposed to a saturated water atmosphere.

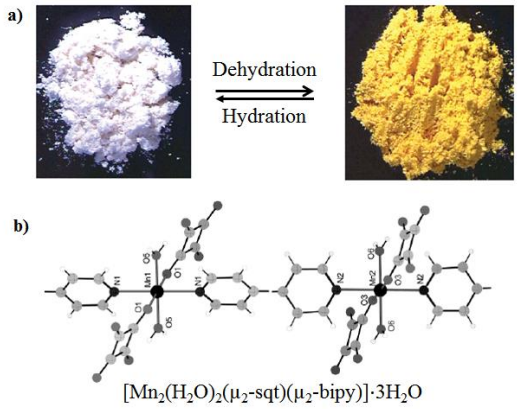

Figure 15 a) Change of colour from colourless to yellow after complete removal of water guest molecules, **b)** Mn(II) octahedral coordination environment with two terminal water molecules (Adapted from reference 37).

Finally, Takaoka *et al*. reported a reversible apical-ligand exchange in the Co(II) ions of a CP with formula $[Co(L)_2(H_2O)_2](NO_3)_2\cdot 1.5H_2O$ (where L is 2,3-bis(2-hydroxyethoxy)-1,4-bis(4-pyridyl)benzene)).[38, 39] In this CP, the Co(II) ions adopt an octahedral geometry coordinated to two water molecules at the apical positions and four pyridyl groups at the equatorial positions (**Figure 16a**). Upon heating at 150°C for 24 hours, the yellow

crystals turned to red because the apical water molecules were substituted by two nitrate ions breaking the CP and forming a non-connected nitrate complex $[Co(L)_2(NO_3)_2]_n$ (**Figure 16b**). However, upon exposure the nitrate complex to air at room temperature, the CP was formed again and the initial yellow colour was recovered (**Figure 16c**).

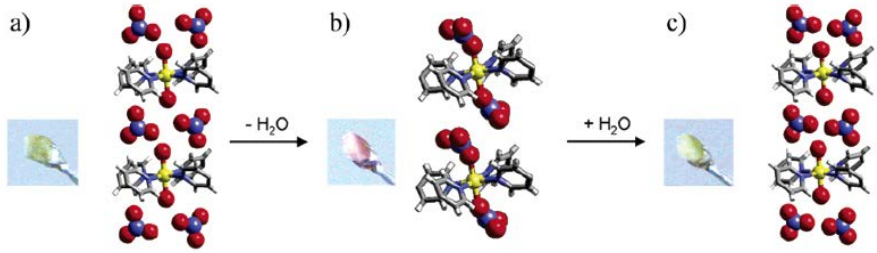

Figure 16 Photographs of crystals and structures around the cobalt ion of (a) the original crystal, (b) the crystal after heating at 423 K for 24 h, and (c) the crystal after exposure to air (Reproduced from references 38, 39).

4.4. Our research: Adenine-based coordination polymers: synthesis, crystal structure, coordination modes and reversible hydrochromic behavior

Based on the rich variety of coordinated modes that adenine can adopt, in the second part of this Thesis, we have exploited its use to synthesize two new three-dimensional CPs in which one of them shows hydrochromic behaviour. This study, which is entitled *"Adenine-based coordination polymers: synthesis, crystal structure, coordination modes and reversible hydrochromic behaviour"* was published in Crystal Growth & Design **2015**, *15*, 3182–3189. In it, we report the synthesis of the two new CPs composed of Co(II), adenine and aromatic tetracarboxylic acids. The selected tetracarboxylic acids are 1,2,4,5-tetrakis(4-

carboxyphenyl)benzene (H_4TCPB) and 1,2,4,5-benzene tetracarboxylic acid (H_4BTeC). [Co_3(μ_6-TCPB)(μ_4-H_2TCPB)(ade)$_2$]·H_2O (**1**) is based on a trinuclear Co(II) cluster, in which the three Co(II) ions are bridged by two bidentate adenine ligands through the N_3 and N_9 sites. [Co_2(ade)(μ_6-BTeC)(μ-H_2O)(H_2O)$_2$]·4(H_2O) (**2**) comprises binuclear Co(II) clusters, which are linked by bidentate adenine linkers (through the N_3 and N_7 sites) forming 1D Co(II)-adenine chains. The orientation of TCPB in **1** results in a compact network, whereas $BTeC^{4-}$ links the Co(II)-adenine chains forming a 3D porous network in **2**. The structure **2** shows reversible structural transformations upon dehydration and hydration, which are accompanied by a detectable colour change from pink to purple, respectively.

This colour change results from the dehydration process, which usually implies removal of coordinated H_2O molecules and therefore, conversion from octahedral (**2**, hydrated, pink) to tetrahedral (**2',** dehydrated, purple) Co(II) coordination geometry (or *vice versa*, for the hydration process).[19-22] It is found that **2'** is non-porous to N_2 or CO_2. Contrariwise, H_2O can diffuse within its framework and organize the well-ordered structure of **2**.

4.4.1. Synthesis of 1 and 2

Overall, both CPs were synthesized through hydrothermal reactions between $CoCO_3$, a basic metal salt source, adenine and H_4TCPB or H_4BTeC in water at 100°C for 48 h. More in detail, **1** was synthesized by placing an aqueous solution (6 mL) of adenine (5 mg, 0.04 mmol), H_4TCPB (10 mg, 0.02 mmol) and $CoCO_3$ (10 mg, 0.08 mmol) in a 12 mL scintillation vial, and the resulting mixture was heated at 100°C for 48 h. After slow cooling

to room temperature during 6 h, 1 was obtained as pink crystals, which were filtered and air-dried (yield: 48 %) (**Figure 17a**).

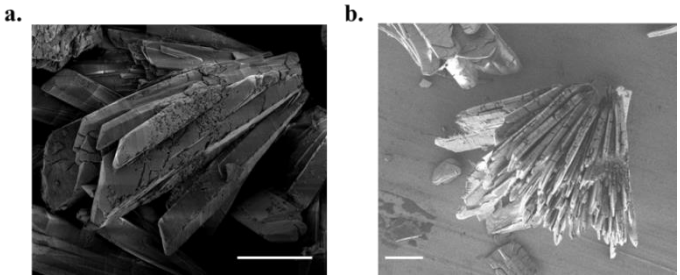

Figure 17 SEM images of **1** (a) and **2** (b), showing that the crystals were needle-shaped and confirming the homogeneity of the sample. Scale bars: 50 μm (a) and 100 μm (b).

In the case of **2**, *a* mixture of adenine (5 mg, 0.04 mmol), H_4BTeC (10 mg, 0.04 mmol) and $CoCO_3$ (10 mg, 0.08 mmol) in water (6 mL) was placed in a 12 mL scintillation vial and heated at 100°C for 48 h. After slow cooling to room temperature during 6 h, pink crystals of **2** were obtained, filtered and air-dried (yield: 25 %) (**Figure 17b**).

Importantly, in both cases, the simulated (derived from the single crystal structure of **1** and **2**, *vide infra*) and experimental powder X-ray diffraction (PXRD) patterns were consistent (**Figure 18**); confirming that **1** and **2** were obtained as pure phases (as also evidenced by elemental analysis and SEM; **Figure 17**). Thermogravimetric analysis (TGA) of **1** revealed multiple weight losses in the range of 315-500°C, corresponding to its decomposition (**Figure 19**). In **2**, the TGA profile indicates weight losses of 18.4% (from 25 to 240°C) and 4% (from 240 to 365°C), which we attributed to the loss of the guest/terminal coordinated H_2O molecules, and μ-H_2O, respectively (Figure 18). Decomposition of 2 starts at 370°C, immediately after the loss of the coordinated H_2O molecules, and occurs in a single step, forming CoO.

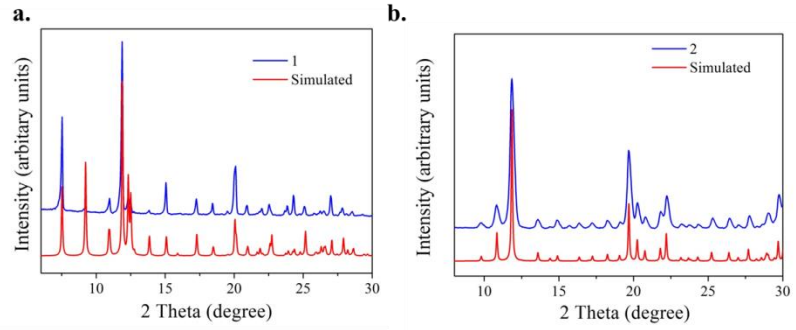

Figure 18 Comparison of the experimental (blue) PXRD pattern of **1 a)** and **2 b)** with the simulated (red) pattern, which was derived from the single crystal X-ray diffraction data.

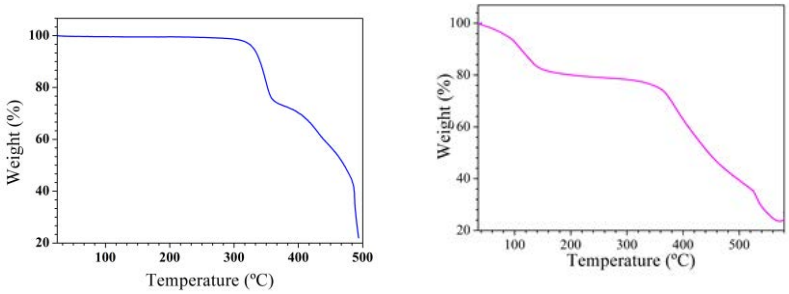

Figure 19 Thermogravimetric diagram of **1** (heating rate: 5 °C/min; temperature range: 25 to 500°C), showing stability up to 315 °C. Decomposition occurred in multiple steps starting from 315 °C

4.4.2. Structural characterization of 1 and 2

Crystallographic data for 1 was collected at 100K at XALOC beamline at ALBA synchrotron[23] (λ = 0.79474 Å). Data were indexed, integrated and scaled using the XDS[24] and iMOSFLM[25] programs. Absorption corrections were not applied. Single crystal X-Ray diffraction for 2 was collected at 298 K on a Bruker AXS SMART Apex diffractometer using graphite monochromated Mo-Kα radiation (λ = 0.71073 Å) and were corrected for Lorentz and polarisation effects. The frames were integrated with the

Bruker SAINT[26] software package. Absorption corrections were applied using the program SADABS[27] giving max./min. transmission factors of 1.000/0.635. Both structures were solved by direct methods and subsequently refined by correction of F^2 against all reflections, using SHELXS2013[28] and SHELXL2013[29] within the WinGX package.[30] All non-hydrogen atoms were refined with anisotropic thermal parameters by full-matrix least-squares calculations on F^2 using the program SHELXL2013. Hydrogen atoms were inserted at calculated positions and constrained with isotropic thermal parameters, except for the hydrogen atoms of N-H and $-NH_2$ groups and the water molecules in 2. The hydrogen atoms of the adenine moiety and the water molecules were located from difference Fourier maps, fixed and isotropically refined. By contrary, in the crystal structure of 1, the disorder associated with the oxygen atoms of the four crystallization water molecules hindered the localization of their hydrogen atoms. In 1, seven distorted atoms were found (one Co, five oxygen carboxylic atoms and one carbon) and the position of the atoms in adenine moiety was fixed and refined using DELU, EADP and SIMU instructions. Several reflections, for which I(obs) and I(calc) were differing more than 10 times SigmaW, were removed from the refinement. On the other hand, the alerts observed during the checkcif can be explained by the quality of the crystal. The best crystal was chosen and attempts to obtain better data were unsuccessful. Although the diffraction experiments proceeded at 100 K under synchrotron radiation, the disorder of the structure could not be reduced and the values of the weighted R factor and wR2 remained high. Moreover, the short Inter D···A contact between the O5A ···O6B and O5A···O6A atoms can be explained by the disorder associated with these O5 and O6. Crystal data of 1 and 2 and structure refinement data are listed in **Table 1**.

In **1**, there are two crystallographically independent Co(II) ions, which are both octahedrally coordinated forming a trinuclear cluster in the order of Co#1–Co#2–Co#1 (Figure 26a). The Co#1-Co#2 distance within this cluster is 3.62 Å. Co#1 is (NO_5)-octahedrally coordinated to the imidazolate N_9 atom of adenine and five carboxylate O atoms from three adjacent TCPB ligands. Co#2 is (N_2O_4)-octahedrally coordinated to the pyrimidinate N_3 atoms of two adjacent adenine ligands and to four neighboring TCPB linkers. Here, adenine is acting as a bridging ligand, linking the two Co#1 and Co#2 ions within the trinuclear cluster through the N_3 and N_9 sites (**Figure 20a**). The three-dimensional structure of 1 is constructed by the connection of these clusters through TCPB linkers. Within the asymmetric unit of **1**, there are two distinct TCPB linkers: i) a $TCBP^{4-}$ linker fully deprotonated that binds to six Co(II) ions with κ2O,O′ and μ-κ2O,O′:κO′ coordination modes (**Figure 20b**; **Figure 21**); and ii) a H_2TCPB^{2-} linker partially protonated, in which two *para*-benzoate groups coordinate to four Co(II) ions with a μ-κO: κO′coordination mode (**Figure 20c**; **Figure 21** and the other two protonated *para*-benzoate groups are hydrogen bonded with H_2O molecules, affording a compact 3D structure (**Figure 20d**).

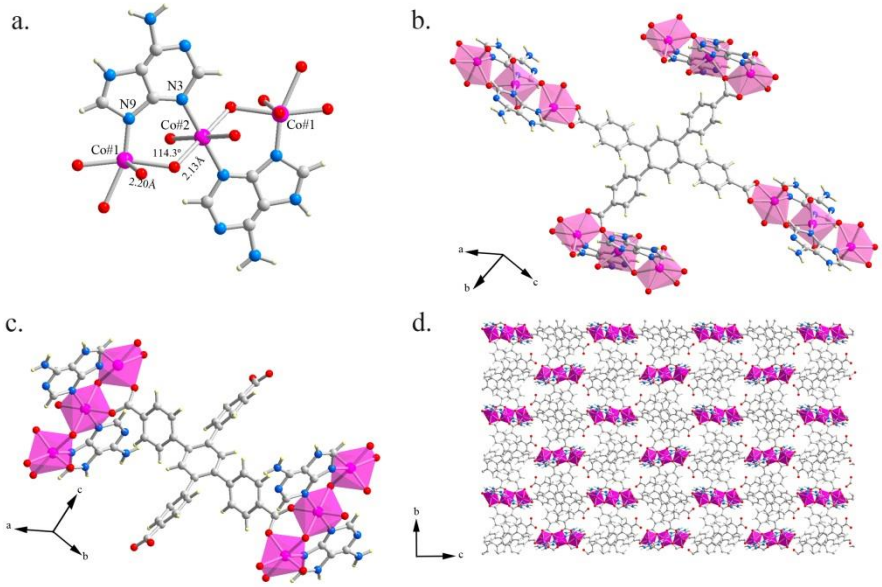

Figure 20 a) Illustration of the Co#1–Co#2–Co#1 basic unit in **1**, showing that Co#1 and Co#2 ions are linked by two bidentate adenine ligands. The pink octahedra represents the coordination environment of Co(II) ions. **b)** Illustration showing the $TCPB^{4-}$ linker that binds to six Co(II) centers and connects four Co#1–Co#2–Co#1 clusters. **c)** Illustration showing the H_2TCPB^{2-} linker that binds to four Co(II) centers and connects two Co#1–Co#2–Co#1 clusters. **d)** Perspective view of the overall 3D compact framework of 1. Colour code: O: red; N: blue; H: pale yellow; C: grey; and Co: pink.

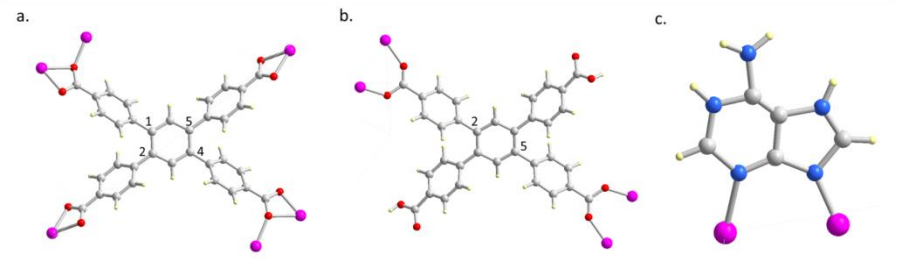

Figure 21 a) Coordination modes of $TCPB^{4-}$. **b)** Coordination modes of $H2TCPB^{2-}$. **c)** [N3, N9] Coordination mode of adenine. The adenine shows terminal coordination behaviour through N3 and N9 atoms. (Pink: Co; grey: C; red: O; blue: N; and yellow: H)

In order to better understand the crystal structure of **1**, a topological analysis was performed using TOPOS[31] program. As a result, **1** shows a 3D

binodal 4,6-c net where each Co#1–Co#2–Co#1 cluster is connected to ten other clusters through 6 TCPB ligands with distances in the range of 15.77-26.63 Å. Overall, this MOF shows a new topology with the point symbol {4^4.6^10.8}{4^4.6^2} (**Figure 22a**).

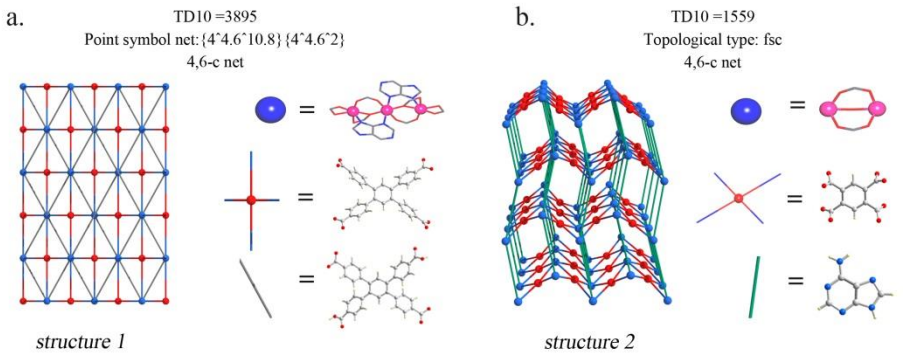

Figure 22 Topological illustration of **1** a) and **2** b), and the simplifications used in the analysis with TOPOS program. Note that a new topology was found for **1**.

The basic unit of **2** is a binuclear Co#1-Co#2 cluster, in which both Co(II) ions exhibit (NO_5)-octahedral geometries, although with different coordination environments (**Figure 23a**). Co#1 is coordinated to the pyrimidinate N_3 atom of adenine, four carboxylate O atoms from four adjacent $BTeC^{4-}$ ligands, and one μ-H_2O molecule bridging both Co(II) ions. In contrast, Co#2 is coordinated to the imidazolate N_7 atom of adenine, two carboxylate O atoms from $BTeC^{4-}$, two terminal H_2O molecules and the μ-H_2O bridge (Figure **23a**). The Co#1-Co#2 distance within this cluster unit is 3.63 Å. Comparison of the bond lengths for Co#1-μ-H_2O and Co#2-μ-H_2O (2.15 Å and 2.14 Å, respectively), and the angle between Co#1-H_2O-Co#2 (115.8º), with corresponding literature values for structures containing the same metal M-O-M unit (CSD codes:

ZALXAL, UMAGUK),[32, 33] confirmed the presence of the H_2O bridge. Adenine linkers bridge the Co#1-Co#2 clusters involving the N_3 and N_7 sites, thus forming 1D chains running along the *c*-axis (**Figure 23b**). The use of the tetracarboxylate $BTeC^{4-}$ linkers was found to be prolific for the expansion of **2** in three dimensions, as each $BTeC^{4-}$ links four neighboring chains (one from each carboxylate site) (**Figure 23c**).

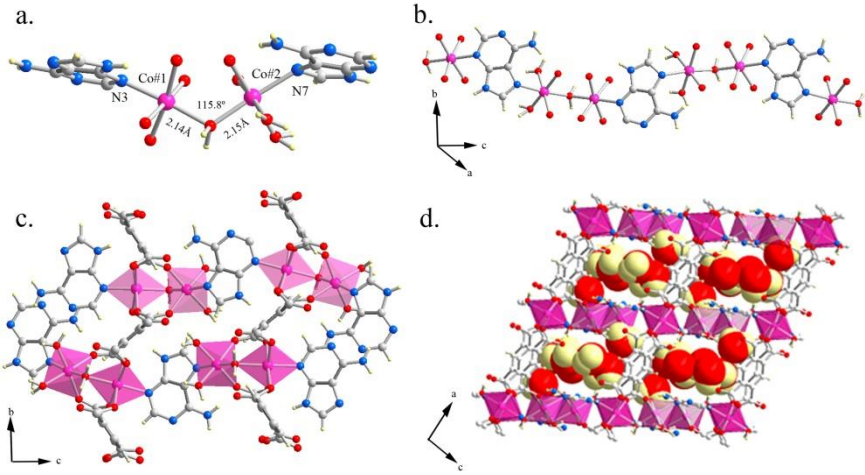

Figure 23 a) Illustration of the Co#1-Co#2 unit within **2**. **b)** Representation of the 1D chains built up from connecting the Co#1-Co#2 units through adenine ligands. **c)** Representation of the 1D chains linked by $BTeC^{4-}$ ligands (the C atoms of $BTeC^{4-}$ are colored in dark grey) to form the 3D framework of **2**. The pink octahedron represents the coordination environment of Co(II) ions. **d)** Illustration of **2**, showing the 1D channels filled with guest H_2O molecules (space filling). Color code: O: red; N: blue; H: pale yellow; C: grey; and Co: pink.

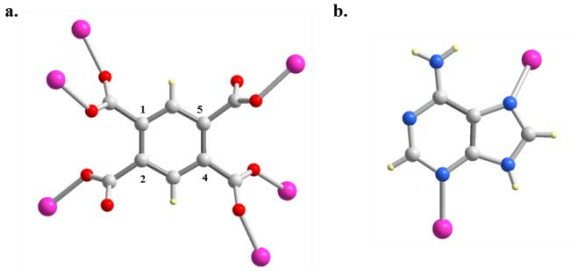

Figure 24 a) Coordination modes of $BTeC^{4-}$. **b)** [N3, N7] Coordination mode of adenine. (pink: Co; grey: C; red: O; blue: N; and yellow: H)

In particular, each $BTeC^{4-}$ binds to six Co(II) centers in two coordination modes: a monodentate κO mode, in binding Co#1 from the carboxylate positions 1 and 4; and a bidentate μ-κO: κO' mode, in bridging Co#1 and Co#2 from the carboxylate positions 2 and 5. Framework **2** generates regular 1D pore channels (5.3 x 4.8 Å; 609.1 $Å^3$; 27% of void space in unit cell)[34] along the *b*-axis (**Figure 25**). **Figure 23d** shows that the pores accommodate four guest H_2O molecules per formula unit. Importantly, the amino -NH_2 and the imidazolate -NH of adenine that reside within the channel establish H-bond interactions with water molecules and oxygen atoms of the carboxylic groups. Moreover, the N_1 pyridiminate nitrogen atom acts as acceptor of H-bond interactions established with water molecules. The theoretical pore volume of **2** calculated from the crystallographic structure after removing the guest H_2O molecules is 0.176 cm^3g^{-1}. In this case, the topological analysis showed that **2** presents the known fsc net (**Figure 22b**).

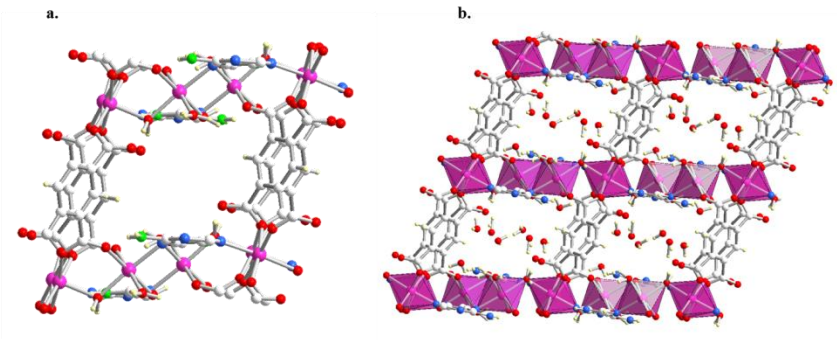

Figure 25 a) Illustration of a single pore in **2**, showing that the Lewis-base groups of ade are distributed over the internal surface of the network. **b)** Supramolecular association leading the formation of 1D pores filled with the H-bonded H_2O molecules (pink: Co; grey: C; red: O; blue: N; yellow: H; and green: N atoms from the amino NH_2, and imidazolate NH of ade).

Table 1 Crystal and Structure Refinement data.

Compound	1	2
Empirical formula	$C_{78}H_{48}N_{10}O_{24}Co_3$	$C_{15}H_{21}N_5O_{15}Co_2$
Formula weight	1686.05	629.23
Crystal system	Monoclinic	Monoclinic
Space group	$P2_1/n$	$P2_1/n$
CCDC ref	1043962	1043963
Unit cell dimensions		
a (Å)	9.77	9.47
b (Å)	17.33	12.58
c (Å)	22.71	18.98
β (deg)	100.9	93.5
V ($Å^3$)	3775.8	2256.0
Z	2	4
F (000)	1710	1280
θ range (°)	1.66-33.82	1.94-28.39
Ind refln (R_{int})	9365 (0.0349)	5531 (0.1063)
Final R indices	R1 = 0.1272	R1 = 0.0573
[I > 2σ(I)]	wR2 = 0.4550	wR2 = 0.1220

4.4.3. Adenine in CPs.

An analysis of extended structures containing adenine and transition metal ions obtained from the Cambridge Structural Database (CSD; Allen, 2002) illustrates the rich coordination modes that can adopt adenine for constructing CPs. From this study, we found that adenine can act as a

simple monodentate ligand, mainly through the N_3 or N_9 site.[35-37] Examples of these coordination modes were observed by García-Terán *et al*. in 1D Zn(II)- and Cu(II)-oxalate chains, in which adenine coordinates these metal ions only through the N_3[35] and the N_9[37] site, respectively (**Figures 26a** and **26b**).

Adenine can also act as a bidentate ligand; having here a wide variety of combinations depending on the N sites that participate in the metal binding. Overall, we have detected that adenine can coordinate to two metal ions through the: i) [N_3, N_9];[38, 39] ii) [N_7, N_9];[39-42] iii) [N_1, N_9];[43] iv) [N_1, N_7];[39] and v) [N_3, N_7] (in **2**) sites. An example of the first coordination mode was reported by Stylianou *et al.* in $[Ni_3(PZDC)_2(ade)_2(H_2O)_4](H_2O)_{1.5}$ (where PZDC = 3,5-pyrazoledicarboxylate).[38] In this structure, adenine participates in the formation of Ni(II) dimers by bridging two Ni(II) ions through the N_3 and N_9 sites (**Figure 26c**). These Ni(II) units are then connected through PZDC linkers, forming chains that are 3D hydrogen-bonded. The second coordination mode was observed in [Zn(ade)(INT)]·DMF (where INT = isonictinate; DMF = dimethylformamide).[40] In this compound, adenine connects Zn(II) ions through the N_7 and N_9 sites (**Figure 26d**), creating infinite 1D helices that are 3D linked by the INT linkers. Sanjib Das *et al.* described the third coordination mode in a 1D Cu(II) CP with formula $[Cu(glycine)(ade)(NO_3)(H_2O)]$. Here, adenine connects two Cu(II) ions through the N_1 and N_9 sites (**Figure 26e**), creating zig-zag chains that are 3D hydrogen bonded.[43] An example of the last reported [N_1, N_7] coordination mode (**Figure 26f**) can be found in $[Cd(ade)(IPA)(H_2O)]$ (where IPA = isophtalate). In this 2D CP, adenine forms chains binding Cd(II) ions through the N_1 and N_7 sites, which are further 2D connected by the IPA linkers.[39]

In our reported extended structures **1** and **2**, adenine also acts as a bidentate ligand coordinating to two Co(II) ions. In **1**, adenine bridges two Co(II) ions through the N_3 and N_9 sites forming a trinuclear Co(II) cluster (**Figure 26c**). This coordination mode is very similar to the one observed by Stylianou *et al.*[38] In contrast, adenine exhibits a rare coordination mode through the N_3 and N_7 sites in **2** (**Figure 26g**). To the best of our knowledge, this coordination mode was only observed in two previous discrete Cu(II)-based complexes.[44, 45] Through this [N_3, N_7] coordination mode, adenine participates in the formation of infinite Co(II)-adenine chains that are 3D linked by $BTeC^{4-}$ linkers.

Besides of acting as a bidentate ligand, adenine can also coordinate *via* more than two N sites. In fact, the most common coordination mode found in CPs is [N_3, N_7, N_9].[18, 46-54] For example, adenine coordinates to three Cu(II) ions *via* the N_3, N_7 and N_9 sites (**Figure 26h**) in a porous CP with formula $[Cu_2(ade)_2(H_2O)_2]\cdot[Cu(oxalate)(H_2O)]_2\cdot\sim14\cdot H_2O$.[46] In this CP, four adenine ligands participate in the formation of a paddle wheel unit by bridging two Cu(II) ions through the N_3 and N_9 sites. These units are then connected through mononuclear entities ([Cu(oxalate)(H_2O)]) *via* the N_7 site. More unusual coordination modes for adenine are [N_1, N_6, N_9] and [N_3, N_6, N_9]. An example of the [N_1, N_6, N_9] coordination mode can be found in $[(CH_3Hg)_2(ade)]\cdot EtOH$ (**Figure 26i**).[54] In this structure, two CH_3Hg^+ ions are coordinated through the N_6 and N_9 sites, whereas another CH_3Hg^+ ion is coordinated *via* the N_1 site forming 1D-chains. The other coordination mode was observed in $[(CH_3Hg)_4(ade)](NO_3)$.[55] In this case, four CH_3Hg^+ ions are linked by the N_3, N_6 and N_9 sites (**Figure 26j**), creating a 2D structure.

Finally, adenine can also coordinate four metal ions *via* the N_1, N_3, N_7 and N_9 sites.[56, 57] An example of this coordination mode was reported by

An et al. (Figure 32k) in $[Zn_8(ade)_4(BPDC)_6O{\cdot}2Me_2NH_2]{\cdot}8DMF{\cdot}11H_2O$ (where BPDC = biphenyldicarboxylate; bio-MOF-1).[17] In this structure, Zn(II) ions and adenine coordinate forming chains composed of apex-sharing octahedral cages. These chains are interconnected *via* multiple BPDC linkers, expanding the structure to a 3D porous network.

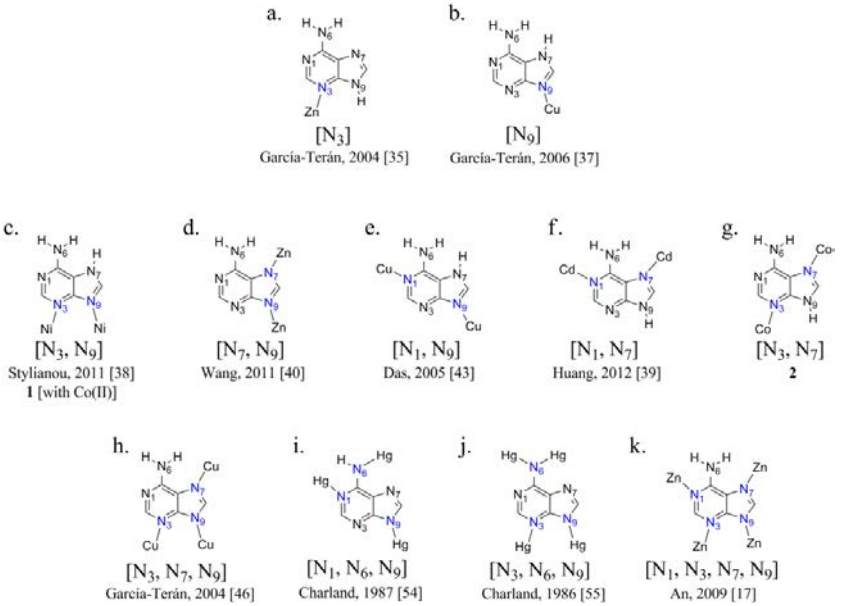

Figure 26 Representation of the coordination modes of adenine observed in extended structures.

4.4.4. Hydrochromic Behavior of 2.

We observed that when **2** was heated at 240°C or at 50°C under vacuum for 12 hours, a new phase, $[Co_2(ade)(BTeC)(H_2O)]$ (**2'**), was formed, as evidenced by elemental analysis. During this transformation, the crystals of **2** were cracked and changed color from pink to purple (**Figure 27a**). This is thought to be due to the change in coordination of Co#2, from octahedral to tetrahedral, which resulted from the loss of the coordinated

H_2O molecules. The UV/Vis spectra revealed a red shift in the d-d transition of the Co(II), from ~514 nm (**2**) to ~532 nm (**2'**), and the absorption band broadened (**Figure 27b**). The sensitivity of these metal-based transitions to the geometry change, which occurs upon conversion of the Co(II) centers from six to mixed six/four coordination, is reminiscent of the color variations observed for other frameworks in which open transition metal sites can be generated.[58, 59] Unfortunately, it was not possible to obtain more structural details of this transformation by determining the structure of **2'** with single crystal X-ray diffraction, but its PXRD pattern showed loss of crystallinity to a high degree (**Figure 27c**). This is indicative that structural re-arrangements occurred upon desolvation and that **2'** is highly disordered.

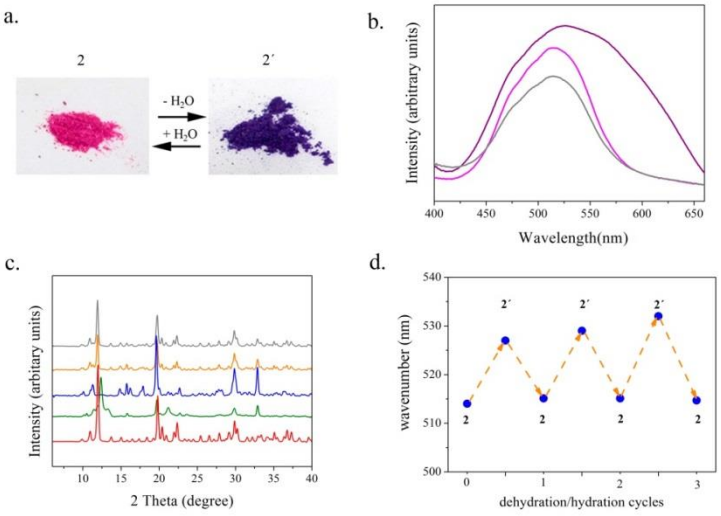

Figure 27 a) Pictures showing the color change from pink (2) to purple (2') upon dehydration and hydration. **b)** UV/vis spectra of 2 (pink), 2' (violet) and regeneration of 2 after the immersion of 2' in liquid H_2O (grey). **c)** PXRD study showing the re-generation of 2 upon immersion of 2' in liquid H_2O after three days: 2 (red), 2' (green) and 2' immersed in water for 1 day (blue), 2 days (orange) and 3 days (grey), and **d)** 2 can be activated and regenerated for at least three times as revealed by UV/vis spectroscopy

retaining the comparable maximum absorption wavenumber (and also followed by the characteristic color change).

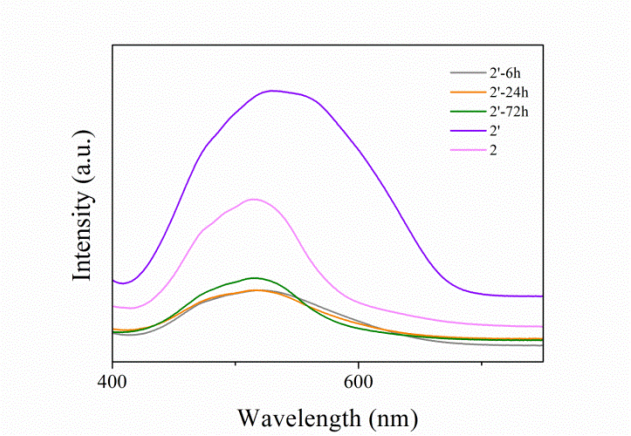

Figure 28 UV/Vis spectra study of the evolution of the absorption band during the transition from **2'** to **2**. Inset corresponds to the length of time that **2'** had been soaked in H_2O.

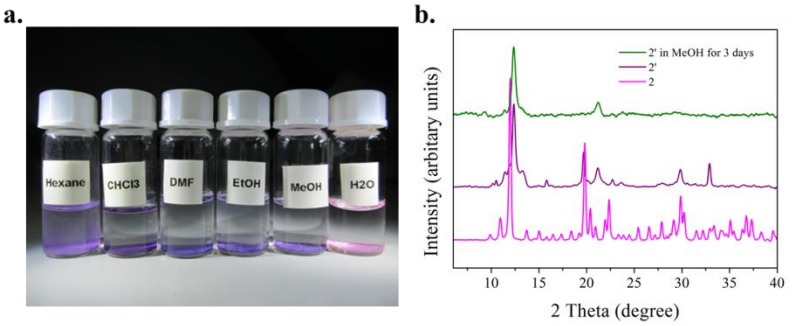

Figure 29 **a)** The characteristic pink colour of **2** appeared only in the sample that had been soaked in H_2O, indicating that hydration of **2'** had occurred. **b)** The PXRD pattern of the sample of **2'** that had been soaked in methanol confirmed that **2** could not be regenerated.

In order to assess the porosity of **2'** and check the influence of the structural re-arrangements upon desolvation, N_2 and CO_2 isotherms collected at 77 K and 195 K, respectively, up to 1 bar (**Figures 30-31**). **2'** adsorbs very small amounts of CO_2 (4.18 cm^3/g at 1 bar) with a BET

surface area of 8.11 m^2/g, and the N_2 isotherm shows a characteristic type II shape confirming the non-porous behavior of **2'**. This observation suggests that upon activation, dramatic structural changes occurred and thus the pores of **2'** are not accessible.

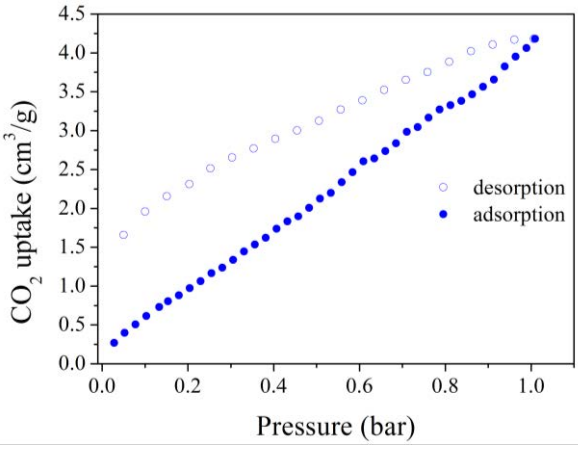

Figure 30 CO_2 isotherm collected on **2'** at 195 K (solid blue dots: adsorption; empty blue circles: desorption).

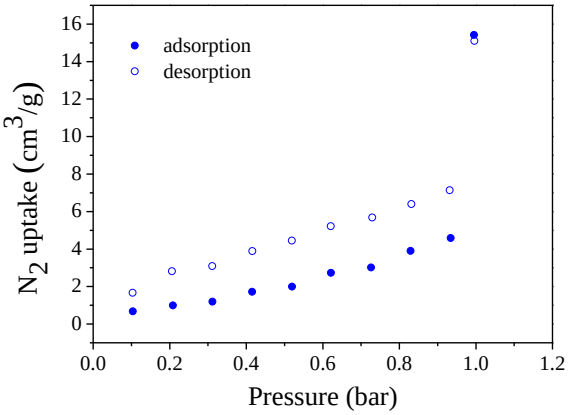

Figure 31 Nitrogen gas isotherm collected on **2'** at 77 K (solid blue dots: adsorption; empty blue circles: desorption

The structural changes observed between hydrated and dehydrated materials encouraged us to deeply analyzed this hydrochromic behavior. For this, we studied how **2'** responds to the presence of liquid H_2O and organic solvents. **2'** was initially immersed in liquid H_2O for different periods of time, and the evolution of the structure was monitored by PXRD and UV/Vis spectroscopy. Notably, after 24 hours, the purple colour of **2'** had changed to pink and the corresponding absorption band had blue-shifted to 524 nm (**Figure 27b**; **Figure**). The PXRD patterns showed an increase in crystallinity with time, which had stabilized after 2 days (**Figure 27c**). After 3 days, both the main reflection at $2\theta = 11.9°$ and the absorption band at 514 nm, were essentially recovered compared with those observed for the newly synthesized **2** (**Figures 27b-c**).

This recovery confirmed a large degree of reversibility for the H_2O-induced structural changes, indicating that H_2O can be re-adsorbed within the framework: the H_2O molecules can coordinate to the Co#2 center, regenerating its octahedral coordination geometry, and H_2O molecules can enter the pores, re-establishing the H-bonds between them and the functional groups (mainly of the adenine) in the pores, as evidenced by elemental analysis. The consistency and reversibility of these H_2O-sorption-induced structural changes were confirmed by exposing a sample of **2** to three cycles of alternate dehydration (under vacuum at 50°C overnight) and rehydration (soaking in H_2O for 3 days). **Figure 27d** illustrates the alternating dehydration/hydration behaviour measured in **2**, with reversible absorption band shifts from 514 to 515 nm (**2**), to 528 to 532 (**2'**). Based on this observation (H_2O importance for the recovery of **2**), we checked if **2** could be recovered through the formation of these specific H-bonding interactions between the framework with other polar and apolar solvents. Thus, the violet solid (**2'**)

was soaked in liquid methanol, ethanol, dimethylformamide, chloroform and hexane (**Figure 29**). It is found that the violet colour of **2'** was retained after three days of treatment with all the solvents suggesting the well-organized structure of **2** was not formed. The PXRD of the methanol loaded sample confirmed that **2** cannot be recovered, indicating that the specific interactions between H_2O molecules and host framework are key factors for retaining the structural integrity of **2**.[12]

4.5 Conclusions

In conclusion, we have prepared two new 3D CPs assembled from Co(II), adenine and aromatic tetracarboxylic acids. From a structural point of view, **1** shows a compact 3D binodal 4,6-c net with a new topology with the point symbol {4^4.6^10.8}{4^4.6^2}. **2** shows a fsc net, in which adenine acts as a bidentate linker through a rare coordination mode; that is, through the N_3 and N_7 sites. In addition, **2** exhibits a clearly observable and reversible colour change from pink (**2**) to purple (**2'**), and *vice versa*, upon dehydration and hydration, respectively, indicative that structural re-arrangements occurred upon activation. This has a direct impact on its sorption behaviour as it is non-porous to CO_2 or N_2. Contrawise, we found that H_2O molecules can diffuse within the pores and organize the 3D open structure of **2**. Selective pore recovery is likely driven by the re-establishment of the H-bonds occurred between H_2O molecules and adenine in the host framework. Stable and H_2O-responsive Co(II)-based CPs can be particularly interesting as potential desiccants: for example, in air purification or in energy-efficient dehumidification at flue gas plants.

4.6 References

1. N. Hadjiliadis and E. Sletten, *Metal Complex-DNA Interactions*, Wiley, 2009.
2. I. Imaz, M. Rubio-Martinez, J. An, I. Sole-Font, N. L. Rosi and D. Maspoch, *Chemical Communications*, 2011, **47**, 7287-7302.
3. P. Amo-Ochoa and F. Zamora, *Coordination Chemistry Reviews*, 2014, **276**, 34-58.
4. S. Sivakova and S. J. Rowan, *Chemical Society Reviews*, 2005, **34**, 9-21.
5. S. Verma, A. K. Mishra and J. Kumar, *Accounts of Chemical Research*, 2009, **43**, 79-91.
6. M. Zhang, W. Lu, J.-R. Li, M. Bosch, Y.-P. Chen, T.-F. Liu, Y. Liu and H.-C. Zhou, *Inorganic Chemistry Frontiers*, 2014, **1**, 159-162.
7. J. P. García-Terán, O. Castillo, A. Luque, U. García-Couceiro, P. Román and L. Lezama, *Inorganic Chemistry*, 2004, **43**, 4549-4551.
8. S. Pérez-Yáñez, O. Castillo, J. Cepeda, J. P. García-Terán, A. Luque and P. Román, *Inorg. Chim. Acta*, 2011, **365**, 211-219.
9. J. P. Garcia-Teran, O. Castillo, A. Luque, U. Garcia-Couceiro, G. Beobide and P. Roman, *Dalton Transactions*, 2006, DOI: 10.1039/b510018f, 902-911.
10. K. C. Stylianou, J. E. Warren, S. Y. Chong, J. Rabone, J. Bacsa, D. Bradshaw and M. J. Rosseinsky, *Chem. Commun.*, 2011, **47**, 3389-3391.
11. H.-X. Huang, X.-Z. Tian, Y.-M. Song, Z.-W. Liao, G.-M. Sun, M.-B. Luo, S.-J. Liu, W.-Y. Xu and F. Luo, *Aust. J. Chem.*, 2012, **65**, 320-325.
12. F. Wang, Y.-X. Tan, H. Yang, H.-X. Zhang, Y. Kang and J. Zhang, *Chem. Commun.*, 2011, **47**, 5828-5830.
13. A. K. Paul, U. Sanyal and S. Natarajan, *Crystal Growth & Design*, 2010, **10**, 4161-4175.
14. F. Wang, H. Yang, Y. Kang and J. Zhang, *J. Mater. Chem.*, 2012, **22**, 19732-19737.
15. S. Das, C. Madhavaiah, S. Verma and P. K. Bharadwaj, *Inorg. Chim. Acta*, 2005, **358**, 3236-3240.
16. J. An, S. J. Geib and N. L. Rosi, *J. Am. Chem. Soc.*, 2010, **132**, 38-39.
17. T. Li, D.-L. Chen, J. E. Sullivan, M. T. Kozlowski, J. K. Johnson and N. L. Rosi, *Chemical Science*, 2013, **4**, 1746-1755.
18. J. Hubert and A. L. Beauchamp, *Can. J. Chem.*, 1980, **58**, 1439-1443.
19. J.-P. Charland, J. F. Britten and A. L. Beauchamp, *Inorg. Chim. Acta*, 1986, **124**, 161-167.

20. S. Pérez-Yáñez, G. Beobide, O. Castillo, J. Cepeda, A. Luque, A. T. Aguayo and P. Román, *Inorg. Chem.*, 2011, **50**, 5330-5332.
21. S. Pérez-Yáñez, G. Beobide, O. Castillo, J. Cepeda, A. Luque and P. Román, *Crystal Growth & Design*, 2012, **12**, 3324-3334.
22. E.-C. Yang, H.-K. Zhao, B. Ding, X.-G. Wang and X.-J. Zhao, *New J. Chem.*, 2007, **31**, 1887-1890.
23. F. Wang and Y. Kang, *Inorg. Chem. Commun.*, 2012, **20**, 266-268.
24. J.-P. Charland, *Inorg. Chim. Acta*, 1987, **135**, 191-196.
25. J. P. Charland and A. L. Beauchamp, *Inorg. Chem.*, 1986, **25**, 4870-4876.
26. E.-C. Yang, H.-K. Zhao, Y. Feng and X.-J. Zhao, *Inorg. Chem.*, 2009, **48**, 3511-3513.
27. J. An, O. K. Farha, J. T. Hupp, E. Pohl, J. I. Yeh and N. L. Rosi, *Nat Commun*, 2012, **3**, 604.
28. J. An, S. J. Geib and N. L. Rosi, *Journal of the American Chemical Society*, 2009, **131**, 8376-8377.
29. L. E. Kreno, K. Leong, O. K. Farha, M. Allendorf, R. P. Van Duyne and J. T. Hupp, *Chemical Reviews*, 2011, **112**, 1105-1125.
30. C. Reichardt and T. Welton, in *Solvents and Solvent Effects in Organic Chemistry*, Wiley-VCH Verlag GmbH & Co. KGaA, 2010, DOI: 10.1002/9783527632220.ch6, pp. 359-424.
31. Z.-Z. Lu, R. Zhang, Y.-Z. Li, Z.-J. Guo and H.-G. Zheng, *Journal of the American Chemical Society*, 2011, **133**, 4172-4174.
32. D. Sarma, K. V. Ramanujachary, S. E. Lofland, T. Magdaleno and S. Natarajan, *Inorganic Chemistry*, 2009, **48**, 11660-11676.
33. Z. Su, M. Chen, T.-a. Okamura, M.-S. Chen, S.-S. Chen and W.-Y. Sun, *Inorganic Chemistry*, 2011, **50**, 985-991.
34. E. Coronado and G. Minguez Espallargas, *Chemical Society Reviews*, 2013, **42**, 1525-1539.
35. O. S. Wenger, *Chemical Reviews*, 2013, **113**, 3686-3733.
36. C.-L. Chen, A. M. Goforth, M. D. Smith, C.-Y. Su and H.-C. zur Loye, *Angewandte Chemie International Edition*, 2005, **44**, 6673-6677.
37. C. Näther, J. Greve and I. Jeβ, *Chemistry of Materials*, 2002, **14**, 4536-4542.
38. K. Takaoka, M. Kawano, M. Tominaga and M. Fujita, *Angewandte Chemie International Edition*, 2005, **44**, 2151-2154.
39. K. Takaoka, M. Kawano, T. Hozumi, S.-i. Ohkoshi and M. Fujita, *Inorganic Chemistry*, 2006, **45**, 3976-3982.

Chapter 5

Conclusions

5. Conclusions

The efforts in this Thesis were addressed to take advantage of the coordination abilities of biomolecules, amino acids and nucleobases, having impact in two important topics of the chemistry of coordination polymers: i) to expand the variables to take account in the synthesis of chiral crystalline materials, introducing the enantiomeric ratio as a valuable variable, and ii) to show the importance of adenine as relevant building block in the construction of novel and functional metal-organic frameworks.

In the first part of this Thesis, we showed the importance of enantiomeric ratio as relevant variable in the synthesis of porous metal-organic frameworks. Enantiomeric ratio can be introduced as variable with surprising results which enabled us to obtain a porous material from a non-porous enantiopure material. We found these remarkable results using a racemic mixture of an aspartic acid-based benzene-1,3,5-tricarboxamide as chiral linker, BTAsp. Here, we have demonstrated that the ratio of two opposite enantiomeric ligands can influence the final structure of the resulting MOFs. We showed that by simply modifying the ratio of ***S***-BTAsp/***R***-BTAsp in a MOF reaction, the structure of the resulting MOF could be tuned between the three structures ***R***, ***RS*** and ***S***, which exhibit different porosity and chirality properties. The systematic identification of new parameters that determine MOF structures is important, as it will enable a greater understanding of structure–function relationships and therefore, enable better engineering of MOFs for targeted applications and will help us to predict the synthesis of porous materials when chiral ligands are used.

The second part of this Thesis was focused in the synthesis of adenine-based coordination polymers. Here we have prepared two new 3D CPs assembled from Co(II), adenine and aromatic tetracarboxylic acids, where we aimed to exploit its five potential coordination sites for metal binding. Here we found that adenine acted as bridging ligand through the N3 and N9 sites in $[Co_3(\mu_6\text{-TCPB})(\mu_4\text{-}H_2TCPB)(ade)_2]\cdot H_2O$, or as terminal ligand through the N3 and N7 sites in $[Co_2(ade)(\mu_6\text{-BTeC})(\mu\text{-}H_2O)(H_2O)_2]\cdot 4(H_2O)$, a rare coordination mode. In addition, $[Co_2(ade)(\mu_6\text{-BTeC})(\mu\text{-}H_2O)(H_2O)_2]\cdot 4(H_2O)$ exhibits a clearly observable and reversible colour change from pink to purple, and vice versa, upon dehydration and hydration, respectively, indicative that structural re-arrangements occurred upon activation. This has a direct impact on its sorption behaviour as it is non porous to CO_2 or N_2. On the contrary, we found that H_2O molecules can diffuse within the framework and organize the 3D open structure. Selective structural recovery is likely driven by the re-establishment of the H-bonds occurred between H_2O molecules and adenine in the host framework.

Appendix

In the appendix of this PhD thesis the two publications related to the main objectives of the Thesis are presented.

The first work is related to the results presented in Chapter 3. The article entitled "The influence of the enantiomeric ratio of an organic ligand on the structure and chirality of metal–organic frameworks" published in *Chemical Communications*, 2014, 13829-13832, explore the enantiomeric ratio as relevant variable in the synthesis of porous metal-organic frameworks, and its influence over the structural properties as porosity and chirality.

And finally, the second publication presents the results described in Chapter 4. The study, entitled *"Adenine-based coordination polymers: synthesis, crystal structure, coordination modes and reversible hydrochromic behaviour"* was published in Crystal Growth & Design 2015, 15, 3182–3189.